ESR AND MÖSSBAUER STUDIES ON STRUCTURE AND MAGNETIC PROPERTIES OF IRON-CONTAINING AMORPHOUS OXIDES

KATSUHISA TANAKA

1990

ESR AND MÖSSBAUER STUDIES ON STRUCTURE AND MAGNETIC PROPERTIES OF IRON-CONTAINING AMORPHOUS OXIDES

KATSUHISA TANAKA

1990

CONTENTS

CHAPTER 1

INTRODUCTION

The amorphous solids in Fe_2O_3-based system are interesting substances from a viewpoint of amorphous magnetism.[1] In this field, amorphous alloys have been investigated most extensively. They are known to show the second order transition at the well-defined Curie temperature and to have critical exponents which obey the scaling law the same as crystalline ferromagnetic matters do. For instance, the critical exponent β which describes the temperature dependence of magnetization as $M(T)=M_0(1-T/T_C)^{\beta}$ is observed to be 0.4[2] which is consistent with the value expected from several theoretical models. The spin wave, which is known to obey the Bloch law at low temperatures, is also observed.[3)-7)] However, the existence of a fluctuation of internal fields due to the random arrangement of magnetic atoms leads to some anomalies in the behavior of magnetization, susceptibility, spin wave and so on. For example, the temperature dependence of the inverse initial paramagnetic susceptibility does not follow the Curie-Weiss law, but exhibits the upward curvature.[2),8)] The Arrott plots, that is, the plots of M^2 as a function of H/M, where M is the magnetization and H the applied field, draw the downward curvature,[2),7),8)] while the plots for the ferromagnetic crystals exhibit the straight line as expected from the molecular field theory. The spin wave stiffness constant D which describes the dispersion relation for the spin wave as $h\omega = Dk^2$ where k is the wave vector shows field dependence while that in crystalline states is independent of the field.[9),10)] These phenomena have

been explicated by considering the fluctuation in the magnetic moment at each atomic site.[11)-13)] The existence of the fluctuation in the magnetic moment has been demonstrated by analyzing the broad linewidth appearing in the Mössbauer spectra of these amorphous alloys.[14),15)]

On the other hand, most of the amorphous oxides containing large amounts of iron ions are known to show so called spin glass- or cluster spin glass-like (mictomagnetic) transition at low or very low temperatures as revealed by the vigorous investigations in these two decades.[16)-20)] Therefore, they are often designated "amorphous insulating spin glasses." The existing facts on the magnetism of the amorphous insulating spin glasses are as follows:

1) The susceptibility vs. temperature curve experiences a maximum in zero field cooling, which corresponds to the spin-freezing temperature. This maximum vanishes when the field cooling is applied. These phenomena are prototypal features of the cluster spin glass.

2) The relation between susceptibility and temperature follows the Curie-Weiss law at high temperatures and the reciprocal susceptibility vs. temperature curve intersects the temperature axis in the negative region, indicating that an antiferromagnetic interaction is dominant between magnetic ions.

3) The gradual decrease of the effective magnetic moment occurs nearly above the spin-freezing temperature, suggesting that the superparamagnetic clusters where spins are aligned in an antiferromagnetic fashion are present.

4) The spin-freezing temperature shifts depending on the frequency of ac susceptibility measurements, the relation of which is describable in terms of the Vogel-Fulcher empirical equation.

5) The remanent magnetization decays with time as $M(t) \approx \log t$.

6) Individual spins are frozen in random directions well below the spin-freezing temperature. This situation is often called speromagnetism.[21),22)]

It is reasonable to say that the above features are characteristic of the random spin system where the magnetic interaction in long range order such as RKKY interaction is not present.

In addition to these glasses which show the cluster spin glass-like behavior with antiferromagnetic interactions among magnetic ions, oxide glasses possessing ferromagnetic properties have been found. Coey et al.[23)] have revealed that an amorphous oxide $Fe_{0.50}{}^{3+}Fe_{0.19}{}^{2+}Ga_{1.37}O_3$ exhibits ferromagnetic properties with Curie temperature of about 150 K. The oxide glasses in the system $La_{1-x}Sr_x\ MnO_3$-B_2O_3[24)] also show the ferromagnetic character. The common feature of these ferromagnetic oxide glasses is that they have transition metal ions in mixed valency states. It is considered that the positive double exchange interaction[25)] among the magnetic ions with different valences is responsible for the ferromagnetism. The oxide and fluoride systems such as amorphous FeF_2,[26)] $CoFe_2O_4$-P_2O_5[27)] and ZnO-Bi_2O_3-Fe_2O_3[28)] also exhibit ferromagnetic character. However, the ferromagnetic order is restricted within an only short range in these materials and the system is rather superparamagnetic or mictomagnetic.

Among them, glasses in the systems FeF_2 and $ZnO-Bi_2O_3-Fe_2O_3$ are interesting materials because the local spin configuration is ferromagnetic although the crystalline FeF_2, $ZnFe_2O_4$ and $BiFeO_3$ are antiferromagnetic.

From the applicative viewpoints, glass containing a large amount of iron oxide is an effective material from which ferrimagnetic substances such as ferrite compounds can be precipitated by heat treatment. Ferrite compounds are magnetically most functional materials among magnetic oxides, and thus extensively utilized as magnetic cores with low iron loss, permanent magnets, recording media involving vertical recording, Faraday effect devices, bubble memory devices and so on. The superiority of the preparation method of ferrite compounds by making use of the crystallization from the glass lies in the fact that it is possible to control the size of particles precipitated which dominates such magnetic properties as magnetization and coercive force. For instance, the fine particle of barium ferrite with hexagonal platelet precipitated from $BaO-Fe_2O_3-B_2O_3$ glass is a promising material for the vertical recording medium.[29] Also the ferrite thin film is one of the effective magnetic materials because the thin film form leads to a great deal of functionality in magnetic properties such as low eddy current loss and very rapid response in memory effect. One way to prepare a thin film is to utilize the crystallization of a gel film which is readily formed from a sol solution.[30] Moreover, there exist a large fraction of magnetic ions situated in the surface in fine particles and thin films. Such magnetic ions are more or less laid in

a random configuration, and lead to magnetic properties different than bulk magnetism.

As shown above, amorphous solids in Fe_2O_3-based system possess interesting magnetic properties from both fundamental and practical viewpoints. However, there still remain several unresolved problems on these materials. For instance, a complete clarification on the mechanism of magnetic transition observed in iron-containing oxide glasses has not been accomplished. The nature of iron ion cluster which dominates the cluster spin glass-like behavior of the oxide glasses is also little revealed. The magnetism of amorphous oxides which show ferromagnetic character is not thoroughly clear. The present investigation was undertaken to resolve such problems.

In Chapter 1, the general background and the purpose of the present investigation are outlined.

In Chapter 2, a theoretical approach to the mechanism of the magnetic transition of iron-based amorphous insulating spin glass is presented.

In Chapter 3, the theory presented in Chapter 2 is applied to several oxide and fluoride glasses.

In Chapter 4, the local structure of iron in oxide glasses which is inevitable for the thorough description of the magnetic properties of these substances is examined.

In Chapter 5, the formation of iron ion cluster in amorphous oxides which is also an important factor for clarification of the magnetic properties of these matters is examined.

In Chapter 6, the magnetic properties of Fe_2O_3-based fine particles and ferrite thin films are discussed.

References

1) Amorphous Magnetism, edited by H.O.Hooper and A.M. de Graaf (Plenum Press, New York, 1973); Amorphous Magnetism II, edited by R.A.Levy and R.Hasegawa (Plenum Press, New York, 1977)

2) S.N.Kaul, Phys. Rev., B23, 1205 (1981)

3) H.N.Ok and A.H.Morrish, Phys. Rev., B22, 4215 (1980)

4) C.L.Chien and R.Hasegawa, Phys. Rev., B16, 2115 (1977)

5) N.Saegusa and A.H.Morrish, Phys. Rev., B26, 10 (1982)

6) A.K.Bhatnagar, B.B.Prasad and R.Jagannathan, Phys. Rev., B29, 4896 (1984)

7) C.C.Tsuei and H.Lilienthal, Phys. Rev., B13, 4899 (1976)

8) H.Kronmüller, J. Appl. Phys., **52**, 1895 (1981)

9) G.Hilscher, R.Hagerb, H.Kricheneyer, M.Müller and H.J.Guntherodt, J. Phys., F11, 2429 (1981)

10) R.Krishnan, M.Dancygier and M.Tarhounin, J. Appl. Phys., **53**, 7768 (1982)

11) T.Kaneyoshi, J. Phys. Soc. Jpn., **51**, 73 (1982)

12) T.Kaneyoshi, Phys. Stat. Sol., (b)**118**, 751 (1983)

13) G.Herzer, M.Fahnle, T.Egami and H.Kronmüller, Phys. Stat. Sol., (b)**101**, 713 (1980)

14) M.E.Lines and M.Eibschütz, Solid State Commun., **45**, 435 (1983)

15) R.J.Pollard, Z.S.Wronski and A.H.Morrish, Phys. Rev., B29, 4864 (1984)

16) T.Egami, O.A.Sacli, A.W.Simpson, A.L.Terry and F.A.Wedgwood, J. Phys., C5, L261 (1972)

17) J.P.Sanchez, J.M.Friedt, R.Horne and A.J. van Duyneveldt, J. Phys., C17, 127 (1984)

18) E.M.Gyorgy, K.Nassau, M.Eibschütz, J.V.Waszczak, C.A.Wang and J.C.Shelton, J. Appl. Phys., **50**, 2883 (1979)

19) S.K.Mendiratta, R.Horne and A.J. van Duyneveldt, Solid State Commun., **52**, 371 (1984)

20) H.Laville and J.C.Bernier, J. Mat. Sci., **15**, 73 (1980)

21) J.M.D.Coey, J. de Phys., **35**, C6-89 (1974)

22) J.M.D.Coey, J. Appl. Phys., **49**, 1646 (1978)

23) J.M.D.Coey, E.Devlin and R.J.Gambino, J. Appl. Phys., **53**, 7810 (1982)

24) K.Inomata, S.Hashimoto and S.Nakamura, Jpn. J. Appl. Phys., **27**, L883 (1988)

25) C.Zener, Phys. Rev., **82**, 403 (1951)

26) F.J.Litterst, J. de Phys., **36**, L-197 (1975)

27) M.Sugimoto and N.Hiratsuka, Jpn. J. Appl. Phys., **21**, 197 (1982)

28) N.Ota, M.Okubo, S.Masuda and K.Suzuki, J. Magn. Magn. Mat., **54-57**, 293 (1986)

29) O.Kubo, T.Ido and H.Yokoyama, IEEE Trans. Magn., **MAG-18**, 1122 (1982)

30) H.Dislich and E.Hussman, Thin Solid Films, **77**, 129 (1981)

CHAPTER 2

THEORY OF CLUSTER SPIN GLASS AND PRINCIPLE OF ESR AND MÖSSBAUER MEASUREMENTS

It has been known that most of the amorphous oxides and fluorides containing a relatively large amount of magnetic ions show a magnetic transition like that of cluster spin glasses or mictomagnets as described in detail in the previous chapter. Verhelst et al.[1] first explained the cluster spin glass behavior of cobalt and manganese aluminosilicate glasses in terms of the superparamagnetic model. They assumed that there exist monodomains where cobalt or manganese ions are concentrated in the glass, and connected the phenomenon that a maximum appeared in the susceptibility vs. temperature curve when the zero field cooling was applied with a progressive freezing of the monodomains in a superparamagnetic fashion. The susceptibility vs. temperature curve they reproduced theoretically was in a qualitative agreement with that obtained experimentally. Since then, this model has been often applied to explain several magnetic properties of oxide glasses. For instance, Rechenberg et al.[2] explicated the experimental fact that the remanent magnetization varies with logarithm of the time for $83.1CoO \cdot 15.5Al_2O_3 \cdot 1.4SiO_2$ glass by using the superparamagnetic domain model. Jamet et al.[3] examined the temperature dependence of ESR line shift and linewidth for $Mn_3Al_2Si_3O_{12}$ glass and concluded that the freezing of each spin takes place progressively in the temperature range of 10 to 3.6 K. This model was also utilized to interpret the magnetic transition of some metallic spin glasses. Wohlfarth[4]

attempted to clarify the spin-freezing temperature of some spin glasses including metallic ones in terms of the anisotropy field which determines the direction of the magnetization in a cluster. Burke et al.[5] described the magnetic structure of Cr-Fe alloys containing 16.7 to 25 at% Fe on the basis of the simple superparamagnetism. However, as Burke et al.[5] pointed out, the simple superparamagnetic model is insufficient for understanding the magnetic behavior of those cluster spin glasses fully, because the cluster existing in those spin glasses is rather the percolation cluster, whose volume varies with temperature, than the single-domain fine particle treated in the superparamagnetism by Nèel,[6] and the intercluster interaction exists. The imporance of considering the variation of the cluster size with temperature and the interaction between clusters has also been pointed out for some cluster spin glasses such as Fe_xNiGe[7] and amorphous $FeO-Al_2O_3-SiO_2$.[8] Theoretical treatment on these problems was firstly carried out by Shtrikman and Wohlfarth.[9),10] They introduced a parameter T_0, temperature corresponding to the intercluster interaction, and gave a physical meaning to Vogel-Fulcher empirical relation which holds in the measuring frequency dependence of the spin-freezing temperature. The Shtrikman-Wohlfarth model, however, has not been applied yet to the amorphous oxide systems where a distribution of superexchange interaction interaction is expected to exist.

In the present chapter, an attempt was made to modify the Shtrikman-Wohlfarth model by taking into account the distribution of superexchange interaction. Further, the principle of ESR and

Mössbauer measurements, which are useful techniques for the clarification of local structure and magnetic properties of amorphous oxides, was described briefly. These measurements will be utilized to obtain experimental facts about the local structure and magnetic properties of amorphous oxides in iron oxide-based system in the following chapters. The experimental facts will not only demonstrate the validity of the model proposed but also give new information about the structure and magnetism beyond the theory.

2.1 Superparamagnetic Model

According to Shtrikman and Wohlfarth,[9),10)] the spin-freezing temperature T_f, which corresponds to the so-called blocking temperature in superparamagnetism, is expressed by the next equation in the weak coupling regime, i.e., the case that the intercluster interaction is much weaker than the anisotropy field:

$$\tau = \tau_0 \exp[(Kv+H_i Mv)/kT_f], \tag{2.1}$$

where k is the Boltzmann constant, K and v are the uniaxial anisotropy and the volume of the superparamagnetic cluster, τ is the relaxation time for rotating the cluster, M is the saturation magnetization, and H_i is the intercluster interaction field. For the assembly of the clusters, H_i can be replaced by a statistical mean value $\langle H_i \rangle$ which is given by

$$\langle H_i \rangle = H_i \tanh \frac{H_i Mv}{kT} \approx \frac{H_i^2 Mv}{kT} \tag{2.2}$$

for weak interactions. From Eqs.(2.1) and (2.2), the next equation holds:

$$\tau = \tau_0 \exp[(Kv+\frac{H_i^2 M^2 v^2}{kT_f})/kT_f]. \tag{2.3}$$

Eq.(2.3) is one result of Shtrikman-Wohlfarth model. Here, we can assume that

$$H_i = mJ, \tag{2.4}$$

where J is the magnitude of superexchange interaction and m is a positive constant. From Eqs.(2.3) and (2.4),

$$M^2 v^2 m^2 J^2 = k^2 T_f^2 \ln(\tau/\tau_0) - kT_f Kv > 0 \tag{2.5}$$

is derived. It is readily found from Eq.(2.5) that

$$\frac{\partial T_f}{\partial J} = \frac{M^2 v^2 m^2}{2k^2 T_f \ln(\tau/\tau_0) - kKv} > 0. \tag{2.6}$$

Therefore, the spin-freezing temperature increases monotonically with increasing the magnitude of the superexchange interaction.

On the other hand, in the strong coupling regime, i.e., the case that the intercluster interaction field is much stronger than the anisotropy field, the Ornstein-Zernike theory is applied so as to describe the correlation of spins. Hence, the effective volume of the cluster within which the spins correlate is expressed as follows:[9),10)]

$$v_{eff} = 4\pi \int r^2 \rho(r/\xi)(r/\xi_0)^{-1} dr, \tag{2.7}$$

where ξ is the correlation length given by

$$\xi = \xi_0[(T-T_0)/T_0]^{-1/2} \tag{2.8}$$

with T_0 being a ordering temperature of the ensemble spins over the clusters. Eqs.(2.7) and (2.8) lead to the next equation:

$$v_{eff} = \varepsilon \xi_0^3 [(T-T_0)/T_0]^{-1}, \tag{2.9}$$

where

$$\varepsilon = 4\pi \int_0^\infty Xe^{-X} dX = 4\pi. \tag{2.10}$$

$\varepsilon \xi_0^3$ is roughly equal to v/p, where p is the volume packing fraction.

The anisotropy constant as well as the volume of the cluster has a temperature dependence. In the Shtrikman-Wohlfarth model, the anisotropy field is assumed to be randomly distributed and its statistical average value is deduced from the random walk model. Thus, the effective anisotropy constant is written as follows:

$$K_{eff} = pKN^{-1/2} = pK(v/pv_{eff})^{1/2}, \tag{2.11}$$

where N is the number of cluster in the correlated volume. From above equations, the next equation is derived:

$$\tau = \tau_0 \exp\{Kv[(T_f-T_0)/T_0]^{-1/2}/kT_f\}. \qquad (2.12)$$

This is the result deduced in the strong coupling regime. In this case, it can be assumed that

$$T_0 = nJ, \qquad (2.13)$$

where n is a positive constant. From Eqs.(2.12) and (2.13), the next relation results:

$$nJ = P^2 T_f^3/(1+P^2T_f^2), \qquad (2.14)$$

where $P=k\ln(\tau/\tau_0)/(Kv)$. Eq.(2.14) leads to the next relation:

$$\frac{\partial T_f}{\partial J} = \frac{n(1+P^2T_f^2)^2}{3+P^2T_f^2} > 0. \qquad (2.15)$$

Therefore, the spin-freezing temperature increases monotonically with increasing the magnitude of superexchange interaction also in this case.

In the present amorphous oxide and fluoride systems, a distribution of superexchange interaction exists because of the distribution of Fe-O-Fe and Fe-F-Fe bond angles.[11)-13)] Hence, the effect of distribution of J should be introduced into Eqs. (2.3) and (2.12) for the construction of the model which can describe the practical system more appropriately. In the weak coupling regime, by using the distribution function f(J), $\langle H_i \rangle$ is rewritten as the mean value in the first approximation:

$$\langle H_i \rangle = \int \frac{H_i^2 Mv}{kT} f(J)\, dJ, \qquad (2.16)$$

where f(J) is the distribution function of superexchange interaction. By using Eq.(2.16), the next equation is derived instead

of Eq.(2.3):

$$\tau = \tau_0 \exp[(Kv + \int \frac{m^2 M^2 v^2 J^2}{kT_f} f(J)\, dJ)/kT_f]. \qquad (2.17)$$

On the other hand, in the strong coupling regime, by replacing the spin correlation length with its average value given by

$$\xi = \xi_0 \int [(T-T_0)/T_0]^{-1/2} \; f(J)\, dJ, \qquad (2.18)$$

Eq.(2.12) is rewritten as follows:

$$\tau = \tau_0 \exp\{Kv \int [(T_f - nJ)/nJ]^{-1/2} \; f(J)\, dJ/kT_f\}. \qquad (2.19)$$

By using Eqs.(2.17) and (2.19), the relation between the spin-freezing temperature and the magnitude of superexchange interaction can be derived in the case that a distribution of the superexchange interaction exists. Here, it is assumed that either the ferromagnetic or the antiferromagnetic interaction is dominant in the system. The situation of coexistence of these two interactions is not considered.

It seems instructive to examine different distribution functions for the analysis of Eqs.(2.17) and (2.19). Here, three types of distribution functions are chosen. The first one is the delta function-like distribution expressed by the next equation:

$$f(J) = \begin{cases} 1/2\Delta J & (J_0 - \Delta J \le J \le J_0 + \Delta J) \\ 0 & (\text{otherwise}) \end{cases}, \qquad (2.20)$$

where J_0 and ΔJ are average value and distribution width of the magnitude of superexchange interaction. The assumption that either the ferromagnetic or antiferromagnetic interaction is dominant results in $J_0 > 0$, $\Delta J > 0$ and $J_0 - \Delta J > 0$. The schematic illustration for this distribution function is given in Fig.2.1.

In the weak coupling regime, the next relation holds:

$$\tau = \tau_0 \exp[(Kv + \int_{J_0-\Delta J}^{J_0+\Delta J} \frac{m^2 M^2 v^2 J^2}{kT_f} \frac{1}{2\Delta J} dJ)/kT_f]. \quad (2.21)$$

By setting that

$$J/\Delta J = x,\ J_0/\Delta J = j,\ \text{and}\ T_f/\Delta J = t, \quad (2.22)$$

Eq.(2.21) is transformed into next equation:

$$3A_1 t^2 - 3A_2 t = 6j^2 + 2 > 0, \quad (2.23)$$

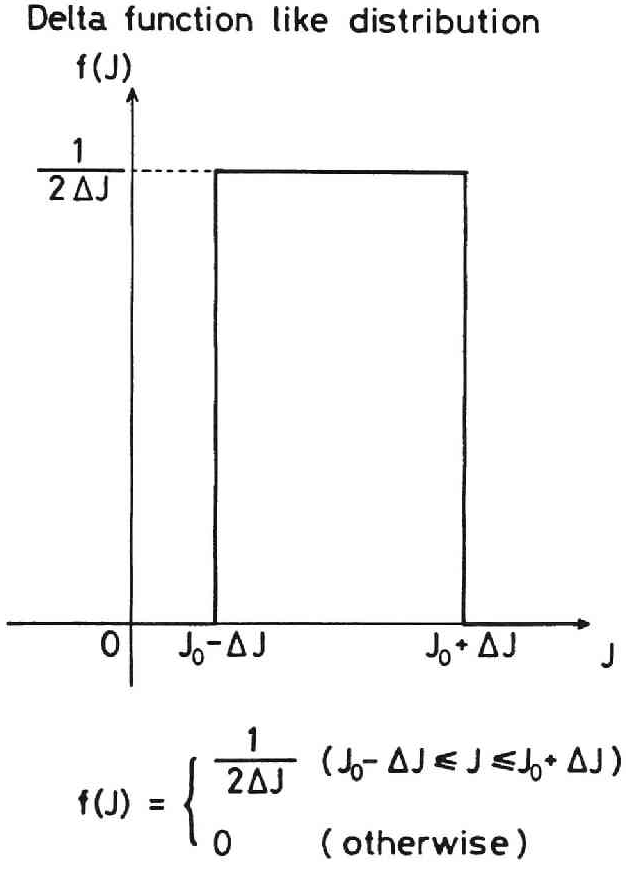

Fig.2.1 Schematic illustration of the delta function-like distribution.

where A_1 and A_2 are positive constants given by

$$A_1 = \frac{2k^2 \ln(\tau/\tau_0)}{m^2 M^2 v^2}, \quad A_2 \quad \frac{2kK}{m^2 M^2 v \Delta J}. \tag{2.24}$$

From Eq.(2.23),

$$\frac{\partial t}{\partial j} = \frac{4j}{2A_1 t - A_2} > 0 \tag{2.25}$$

is derived. This relation leads to

$$\frac{\partial T_f}{\partial J_0} > 0. \tag{2.26}$$

In the strong coupling regime, by substituting Eq.(2.20) into Eq.(2.19) and setting that

$$J/\Delta J = x, \; J_0/\Delta J = j, \text{ and } T_f/n\Delta J = t, \tag{2.27}$$

the next equation is derived:

$$B_1 = \frac{1}{t} \int_{j-1}^{j+1} [(t-x)/x]^{-1/2} \, dx, \tag{2.28}$$

where B_1 is a positive constant given by

$$B_1 = \frac{2kn\Delta J \ln(\tau/\tau_0)}{Kv}. \tag{2.29}$$

The integral in Eq.(2.28) is calculated by setting $x = t\cos^2\theta$. The result is the following one:

$$B_1 = \sqrt{(j-1)(t-j+1)/t^2} - \sqrt{(j+1)(t-j-1)/t^2} + \cos^{-1}\sqrt{(j-1)/t} - \cos^{-1}\sqrt{(j+1)/t}. \tag{2.30}$$

After somewhat lengthy calculation, the next relation is derived from Eq.(2.30):

$$\frac{\partial j}{\partial t} = \frac{1}{1 - \dfrac{\sqrt{(j+1)(t-j-1)} - \sqrt{(j-1)(t-j+1)}}{t[\sqrt{(j+1)/(t-j-1)} - \sqrt{(j-1)/(t-j+1)}]}}. \tag{2.31}$$

Since it is algebraically proved that

$$\sqrt{(j+1)/(t-j-1)} - \sqrt{(j-1)/(t-j+1)} > 0 \qquad (2.32)$$

and

$$t[\sqrt{(j+1)/(t-j-1)} - \sqrt{(j-1)/(t-j+1)}] - [\sqrt{(j+1)(t-j-1)} - \sqrt{(j-1)(t-j+1)}] > 0, \qquad (2.33)$$

the next relation results from Eq.(2.31):

$$\frac{\partial j}{\partial t} > 0. \qquad (2.34)$$

Hence, it is concluded that Eq.(2.26) holds also in the strong coupling regime.

Next, a parabolic distribution is considered. The distribution function is given as follows:

$$f(J) = \begin{cases} -(3/4\Delta J^3)[(J-J_0)^2 - \Delta J^2] & (J_0-\Delta J \le J \le J_0+\Delta J) \\ 0 & (\text{otherwise}) \end{cases} . \qquad (2.35)$$

The distribution is schematically drawn in Fig.2.2. Firstly, the weak coupling regime is taken into account. By substituting Eq.(2.35) into Eq.(2.17) and using Eq.(2.22), we obtain the next equation:

$$2A_1 t^2 - 2A_2 t = \int_{j-1}^{j+1} x^2 [-3(x-j)^2 + 3]\, dx, \qquad (2.36)$$

where A_1 and A_2 are given in Eq.(2.24). By calculating the integral in Eq.(2.36) directly, the next equation is derived:

$$A_1 t^2 - A_2 t = 2j^2 + \frac{2}{5} > 0. \qquad (2.37)$$

Therefore, Eqs.(2.25) and (2.26) also hold in this case. As for the strong coupling regime, the numerical calculation was performed. By substituting Eq.(2.35) into Eq.(2.19) and setting as follows instead of Eq.(2.27):

$$(J-J_0)/\Delta J=x,\ J_0/\Delta J=j,\ \text{and}\ T_f/n\Delta J=t, \tag{2.38}$$

the next equation is derived:

$$B_1 = \frac{3}{2t}\int_{-1}^{1}[(t-j-x)/(j+x)]^{-1/2}(1-x^2)\,dx, \tag{2.39}$$

where B_1 is given in Eq.(2.29). The relation between t and j for arbitrary value of B_1 numerically calculated is drawn in Fig.2.3.

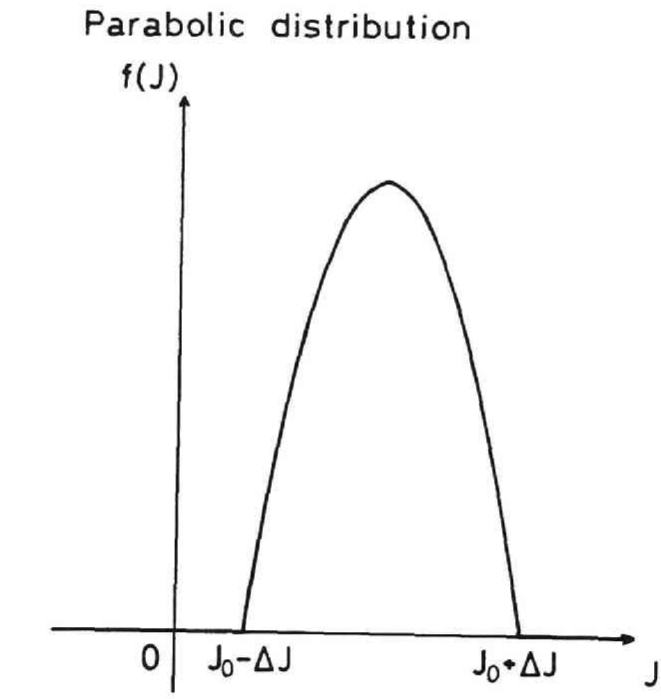

Fig.2.2 Schematic illustration of the parabolic distribution.

It is seen that t increases monotonically with j, indicating that Eq.(2.26) holds.

Finally, the Gaussian distribution

$$f(J) = \frac{1}{\sqrt{2\pi}\Delta J} \exp\left[-\left(\frac{J-J_0}{\sqrt{2}\Delta J}\right)^2\right] \tag{2.40}$$

is adopted. In the weak coupling regime, we obtain the next equation by using Eqs.(2.17), (2.24) and (2.40):

$$A_1 - A_2\Delta J/T = 2\int_{J_0-3\Delta J}^{J_0+3\Delta J} \frac{J^2}{T^2} \frac{1}{\sqrt{2\pi}\Delta J} \exp\left[-\left(\frac{J-J_0}{\sqrt{2}\Delta J}\right)^2\right] dJ, \tag{2.41}$$

where the range of the magnitude of superexchange interaction was restricted to $J_0-3\Delta J \leq J \leq J_0+3\Delta J$ because the integral of the

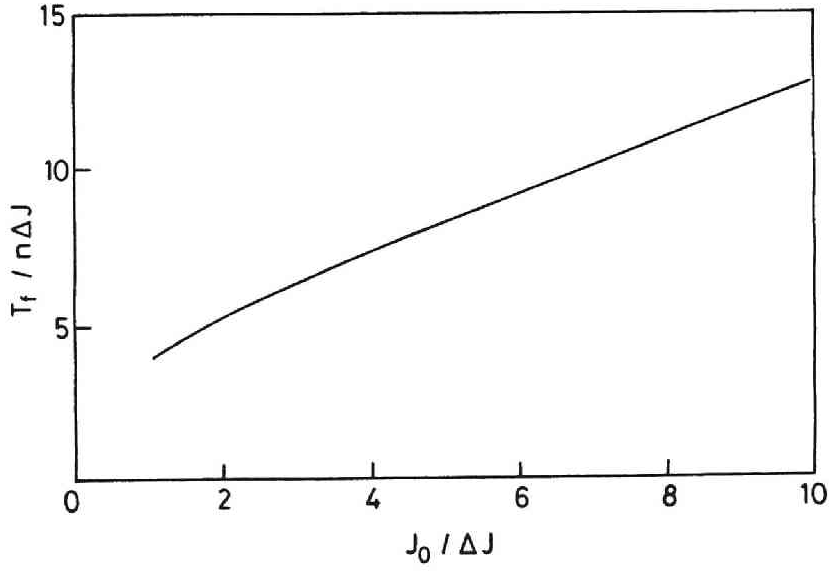

Fig.2.3 Relation between $J_0/\Delta J$ and $T_f/n\Delta J$ calculated for parabolic distribution of J.

Gaussian function in this interval can be approximated to be equal to unity. Besides, $J_0-3\Delta J>0$ was assumed since either ferromagnetic or antiferromagnetic interaction is taken into account in the present calculations. By setting

$$(J-J_0)/\Delta J=x,\ J_0/\Delta J=j,\ \text{and}\ T_f/\Delta J=t, \tag{2.42}$$

Eq.(2.41) is transferred into the next equation:

$$A_1t^2 - A_2t = 2\int_{-3}^{3} (x+j)^2 \frac{1}{\sqrt{2\pi}}\exp(-x^2/2)\,dx. \tag{2.43}$$

For the integral of the Gaussian function in Eq.(2.43), the interval [0,3] can be replaced by [0,∞]. Then, Eq.(2.43) results in the next equation:

$$A_1t^2 - A_2t = \frac{8}{\sqrt{\pi}}\left[\int_0^{\infty} j^2\exp(-x^2/2)\,dx + \int_0^{3} x^2\exp(-x^2/2)\,dx\right]. \tag{2.44}$$

The first term of the right hand in Eq.(2.44) can be easily calculated. The result is the next one:

$$A_1t^2 - A_2t = 2j^2 + \frac{8}{\sqrt{\pi}}\int_0^{3} x^2\exp(-x^2/2)\,dx. \tag{2.45}$$

Since $x^2\exp(-x^2/2)>0$ for $x>0$, the second term of the right hand in Eq.(2.45) is a positive constant. Hence, Eq.(2.25) and then Eq.(2.26) also hold for the Gaussian distribution.

In the course of the analysis of the above three distribution functions in the weak coupling regime, we have noticed that a function which has a symmetry axis of $J=J_0$ generally gives the result indicated by Eq.(2.26). The proof is as follows. From Eqs.(2.17) and (2.24) along with the relations

$$J-J_0=x,\ J_0/\Delta J=j,\ \text{and}\ T_f/\Delta J=t, \tag{2.46}$$

the next equation is derived:

$$A_1 - A_2/t = \frac{2}{t^2} \int_{-\Delta J}^{\Delta J} \left(\frac{x^2}{\Delta J^2} + 2\frac{x}{\Delta J} j + j^2 \right) F(x)\, dx, \qquad (2.47)$$

where $F(x)=f(J)$ for $x=J-J_0$. Since

$$f(J_0+y) = f(J_0-y) \qquad (2.48)$$

for any y, we obtain

$$F(y) = F(-y). \qquad (2.49)$$

Namely, F(x) is an even function. Therefore, Eq.(2.47) results in the next equation:

$$A_1 t^2 - A_2 t = 4j^2 \int_0^{\Delta J} F(x)dx + \frac{4}{\Delta J^2} \int_0^{\Delta J} x^2 F(x)dx. \qquad (2.50)$$

Since $F(x)>0$ for $0<x<\Delta J$, two integrals in the right hand of Eq.(2.50) give positive values. Hence,

$$\frac{\partial t}{\partial j} = \frac{8j \int_0^{\Delta J} F(x)dx}{2A_1 t - A_2} > 0, \qquad (2.51)$$

which leads to Eq.(2.26).

For the strong coupling regime in the case that the Gaussian distribution is assumed, the numerical calculation was carried out the same as the case of the parabolic distribution. By substituting Eq.(2.40) into Eq.(2.19) and setting

$$(J-J_0)/\Delta J=x,\ J_0/\Delta J=j, \text{ and } T_f/n\Delta J=t, \qquad (2.52)$$

the next equation is derived:

$$B_1 = \frac{2}{t} \int_{-3}^{3} [(t-j-x)/(j+x)]^{-1/2} \frac{1}{\sqrt{2\pi}} \exp(-x^2/2)\, dx. \qquad (2.53)$$

The relation between $j=J_0/\Delta J$ and $t=T_f/n\Delta J$ is drawn in Fig.2.4. It is seen that t increases monotonically with increasing j. Therefore, Eq.(2.26) also holds in this case. For all types of distribution of J examined here, it is indicated that T_f in-

creases as J_0 increases in both weak and strong coupling regimes. Namely, the stronger the mean value of the superexchange interaction becomes, the higher the freezing temperature is. This leads to the expectation that T_f increases with increasing the covalency of Fe^{3+}-O and Fe^{3+}-F bonds for the glasses containing the same amount of Fe^{3+} ions since the superexchange interaction between Fe^{3+} ions is known to be proportional to the covalency of these bonds.[14)-16)] Hence, the difference of T_f due to the variation of the glass systems may be explained in terms of the covalency within the framework of the present model. This problem will be discussed in the next chapter.

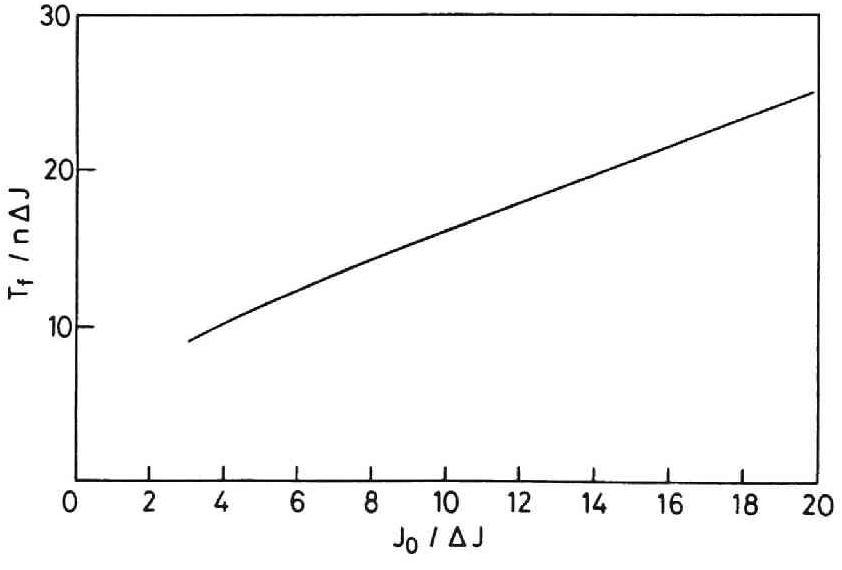

Fig.2.4 Relation between $J_0/\Delta J$ and $T_f/n\Delta J$ calculated for Gaussian distribution of J.

2.2 Principle of ESR and Mössbauer Measurements

2.2.1 ESR Measurements

When an unpaired electron is subjected to the external field, the energy level is splitted due to the interaction between the spin angular momentum of the electron and the external field. Since the magnitude of the energy difference between these levels corresponds to the microwave region, the resonant absorption of the microwave by the electron can occur, yielding the electron spin resonance (ESR) spectrum. The energy state is affected by the crystal field, spin-orbit interaction, magnetic interaction between electron and nuclear spins, and dipolar and superexchange interactions among electrons. Hence, the ESR spectrum gives important information about the chemical and magnetic states of organic radicals and transition elements. As for the transition elements in solids, the information about valency state, site symmetry, covalency of bond, state of exchange-coupled ion pair, magnitude of exchange interaction, spin-lattice interaction, direction of magnetization, etc. has been obtained.

In the present thesis, the chemical and magnetic states of iron will be discussed on the basis of linewidth and g-value of ESR spectrum. Thus, these two factors are described in the following sections.

2.2.1.1 Linewidth

In this section, the linewidth of the ESR spectrum is described on the basis of quantum mechanics.[17] For two functions F(t) and G(t) which vary with time, the correlation function $\phi(\tau)$ is defined as follows:

$$\phi(\tau) = \lim_{T\to\infty} \frac{1}{T} \int_0^T F(t)G(t+\tau)dt. \qquad (2.54)$$

When $\phi(\tau)$ represents the motion of spins, the ESR line shape is expressed as follows:

$$I(\omega) = \frac{1}{2\pi} \int_{-\infty}^{\infty} \phi(\tau)\exp(-i\omega\tau)d\tau. \qquad (2.55)$$

Eq.(2.55) is derived by Wiener-Kinchin theorem. When F(t)=G(t), $\phi(\tau)$ is designated an autocorrelation function. In the Kubo-Tomita theory, the autocorrelation function of resonance frequency $\omega(t,\mathbf{r})$ is defined as follows:

$$\psi(\tau) \quad \frac{\langle\omega(\tau)\omega(0)\rangle}{\langle\omega(0)^2\rangle}. \qquad (2.56)$$

According to the Kubo-Tomita theory, $\phi(t)$, which is the Fourier transformation of the resonant absorption line, is expressed as follows:

$$\phi(t) = \exp(-\omega_d{}^2 \int_0^t (t-\tau)\psi(\tau)d\tau), \qquad (2.57)$$

where ω_d is defined by

$$\omega_d \quad \sqrt{\langle\omega(0)^2\rangle}. \qquad (2.58)$$

Firstly the case that the dipolar interactions are dominant among magnetic ions is considered. Since $\omega(\tau)$ is independent of time in this case, Eq.(2.57) is transferred into the next equation:

$$\phi(t) = \exp(-\omega_d{}^2 t^2/2). \qquad (2.59)$$

By using Eq.(2.55), the next equation is derived:

$$I(\omega) - \frac{1}{\sqrt{2\pi}\omega_d} \exp[-\frac{(\omega-\omega_0)^2}{2\omega_d{}^2}]. \qquad (2.60)$$

Hence, the absorption line is represented by the Gaussian function. Next, the case that the exchange interaction is dominant is taken into account. Because of the exchange interaction, the information the spin possesses at t=0 is lost at $t=J/\hbar$, where J is the energy of the exchange interaction. Hence, Eq.(2.56) is approximately expressed as follows:

$$\psi(\tau) = \begin{cases} 1 & (0<\tau<1/\omega_e) \\ 0 & (\tau>1/\omega_e) \end{cases}, \qquad (2.61)$$

where $\omega_e=J/\hbar$. From Eqs.(2.57) and (2.61), the next equation is derived:

$$\phi(t) = \exp(-\omega_d^2 |t|/\omega_e). \qquad (2.62)$$

Here, $\exp(\omega_d^2/2\omega_e^2)$ is assumed to be unity under the assumption that ω_e is much larger than ω_d. Eq.(2.62) is transferred into the next equation:

$$I(\omega) \quad \frac{\omega_d^2/\omega_e}{\pi} \left[\frac{1}{(\omega-\omega_0)^2 + (\omega_d^2/\omega_e^2)}\right]. \qquad (2.63)$$

Namely, the line shape is Lorentzian in this case. Eq.(2.63) clearly indicates that the exchange interaction makes the ESR linewidth narrower by $1/\omega_e$.

2.2.1.2 g-Value

The g-value for the electron spin is defined as follows:

$$\mu_S = -g\left(\frac{e\hbar}{2mc}\right)S, \qquad (2.64)$$

where μ_s is the magnetic moment of electron, e is the elementary electric charge, $\hbar$ is the Planck constant divided by 2π, m is

the mass of electron, c is the velocity of light and S is the spin angular momentum of electron. The g-value of the electron spin is given as

$$g=2.0023193. \tag{2.65}$$

For the magnetic moment due to orbital angular momentum of electron, g=1 is obtained experimentally. When the magnetic moments due to spin and orbital angular momentums are represented by μ_S and μ_L, respectively, the effective g-value is expressed by the next relation:

$$g_{eff} = \frac{2mc}{e\hbar} \frac{\mu_S + \mu_L}{S + L} . \tag{2.66}$$

The fact that the g-values for the spin and the orbital are 2.00 and 1.00, respectively, leads to the next relation:

$$g_{eff} = \frac{\mu_S + \mu_L}{\mu_S/2 + \mu_L} . \tag{2.67}$$

Since the orbital angular momentum is quenched in a solid because of strong interaction between the orbital and the lattice, Eq. (2.67) is rewritten as follows:

$$g_{eff} = \frac{\mu_S + \mu_L}{\mu_S/2} . \tag{2.68}$$

When the contribution of the orbital angular momentum to the magnetic moment is defined as

$$\varepsilon \quad \mu_L/\mu_S , \tag{2.69}$$

the effective g-value is represented as follows:

$$g_{eff} = 2(1+\varepsilon). \tag{2.70}$$

ε is an order of several percents for crystalline magnetic materials such as iron, cobalt, FeNi, MnSb and $NiFe_2O_4$.[18]

2.2.2 Mössbauer Spectroscopy

Mössbauer effect is a phenomenon that the nucleus in a solid can absorb and emit γ-ray with a certain probability of recoil-free process. It was discovered by Mössbauer in 1958.[19] In the experiment, the energy of γ-ray is varied by using the Doppler effect, and the energy difference corresponding to 0.001 mm/s of Doppler velocity can be readily detected. Since the velocity of γ-ray is $3X10^{11}$ mm/s, the accuracy of the experiment reaches about $3X10^{-15}$. Hence, this effect was successfully utilized for the quantitative demonstration of compression of time due to gravity[20] which was predicted by Einstein in his general theory of relativity.[21] Indeed, in the experiment by Pound and Rebka in 1960,[22] blue shift of γ-ray corresponding to 0.0005 mm/s of Doppler velocity was detected.

As for the application of Mössbauer effect to the solid state chemistry, five parameters, that is, recoil-free fraction, second-order Doppler shift, isomer shift, quadrupole splitting and hyperfine field, are important. These parameters are described in the following sections.

2.2.2.1 Recoil-Free Fraction

The recoil-free fraction is the most essential factor in the Mössbauer effect. This parameter and the second-order Doppler shift which will be described in the next section are effective for the estimation of lattice vibration of solids containing Mössbauer-active elements. The most effective and conventional model to describe the lattice vibration in a solid is the one proposed by Debye.[23] The Debye theory is widely used to explain

the temperature dependence of heat capacity of solids such as alkali halides and metals, and the characteristic temperature or Debye temperature obtained by this theory is regarded as a measure of interatomic bond strength of solids. However, it has become clear recently that this theory does not hold well for solids with a less-closely packed structure. Several attempts have been made in the past to deal with this discrepancy from the Debye theory. For example, Tarasov[24] developed a theoretical model for substances with chain and layer structures by considering both one- and three-dimensional continuum distributions. Blackmann[25] tried to establish the exact frequency distribution function of vibration for some simple two-dimensional lattices, and calculated their specific heat. DeSorbo[26] showed theoretically that the phonon spectrum of crystalline selenium consists of two distinct bands. Recently, Soga and Hirao[27)-29)] showed that the heat capacity data of various network forming inorganic glasses could be represented by the three-band theory using two Debye temperatures (θ_1, θ_3) and one Einstein temperature (θ_E). Since θ_E can be omitted when no network modifier exists, the three-band theory is reduced to the two-band theory with two characteristic temperatures (θ_1, θ_3). This two-band theory was found to be useful to describe the heat capacity data of binary Fe-B and Fe-P amorphous alloys.[30]

The evaluation of the characteristic temperature by utilizing the temperature dependence of the recoil-free fraction or second-order Doppler shift has been also made. For example, Taragin et al.[31] measured the relative value of recoil-free

fraction for Fe^{3+} and Fe^{2+} ions in aluminophosphate glass at various temperatures and calculated the Debye temperature to be 385 K for Fe^{3+} and 230 K for Fe^{2+}. Saegusa and Morrish[32] obtained the Debye temperature of 320 K by measuring the recoil-free fraction and the second-order Doppler shift of amorphous $Fe_{81}B_{13.5}Si_{3.5}C_2$ alloy (METGLAS® 2605SC). Sawatzky et al.[33] found the Debye temperature of 314 K for iron on octahedral sites in Fe_3O_4 and 366 K for iron on octahedral sites in yttrium iron garnet. They noted that those Debye temperatures were much lower than those obtained from specific-heat data. This may be due to the inadequacy of the Debye theory to analyze the recoil-free fraction and second-order Doppler shift data and obtain the characteristic temperature of iron ions or atoms.

In the present section, the two-band theory was applied in place of the Debye theory to analyze the temperature dependence of recoil-free fraction and second-order Doppler shift.

In the harmonic approximation, the recoil-free fraction f at temperature T is given by

$$f \quad \exp(-4\pi^2 < x^2 > /\lambda^2), \tag{2.71}$$

where $< x^2 >$ is the mean-square nuclear displacement of the absorbing nucleus and λ is the wavelength of the absorbed radiation. Quantitatively, the Debye model gives the following expression:

$$f = \exp\{ -\frac{3E_R}{2k\theta_D}[1 + 4(T/\theta_D)^2 \int_0^{\theta_D/T} \frac{x}{e^x - 1} dx]\}, \tag{2.72}$$

where E_R is the recoil-free fraction energy, k is the Boltzmann constant, and θ_D is the Debye temperature.

According to the Debye theory, the vibrational distribution

is given by following an assumption that the whole lattice is isotropic and thus $\rho(\nu)=\alpha\nu^2$. However, in practical solids, the vibrational distribution is more complicated than the one represented by Debye's theory. The frequency mode measured by recoil-free fraction is associated with acoustic mode and consequently affected not only by the interatomic vibration but also by the three-dimensional low-frequency vibrations corresponding to more weak binding of intermolecular type. Therefore, some modification is needed to include these low-frequency vibrations if they exist independently. The two-band theory takes care of this situation. In the two-band theory, the distribution of frequency of phonon is assumed to be as follows:

$$\rho(\nu) = \begin{cases} \dfrac{9N}{\theta_1\theta_3^2}(h/k)^3\nu^2 & (0\le\nu\le\nu_m) \\ \dfrac{3N}{\theta_1}(h/k) & (\nu_m\le\nu\le\nu_1) \end{cases}, \qquad (2.73)$$

where h is the Planck constant and N is the number of atom. θ_1 and θ_3 are characteristic temperatures defined as follows:

$$\theta_1 = h\nu_1/k, \quad \theta_3 = h\nu_m/k. \qquad (2.74)$$

The schematic illustration of Eq.(2.73) is given along with the vibrational density of states for the Debye model in Fig.2.5. The mean-square nuclear displacement of a solid following the two-band model is written as follows:

$$\langle x^2\rangle = \frac{3h^2}{16\pi^2 Mk\theta_1}\Big[\, 3 + 2\ln(\theta_1/\theta_3) + 12(T/\theta_3)^2 \int_0^{\theta_3/T} \frac{x}{e^x-1}\,dx + 4\int_{\theta_3/T}^{\theta_1/T} \frac{1}{x(e^x-1)}\,dx \,\Big], \qquad (2.75)$$

where M is the mass of an atom. By substituting Eq.(2.75) into Eq.(2.71), the following equation is obtained:

$$f = \exp\{ -\frac{E_R}{2k\theta_1}[\, 3 + 2\ln(\theta_1/\theta_3) + 12(T/\theta_3)^2 \int_0^{\theta_3/T} \frac{x}{e^x-1}dx$$

$$+ 4\int_{\theta_3/T}^{\theta_1/T} \frac{1}{x(e^x-1)}\, dx\,]\}. \qquad (2.76)$$

This equation should be comparable to Eq.(2.72). When $\theta_1=\theta_3=\theta_D$, it comes to equal Eq.(2.72). And if

$$T > \theta_1/2 \quad (\theta_1>\theta_3), \qquad (2.77)$$

then Eq.(2.76) can be approximated to the next equation:

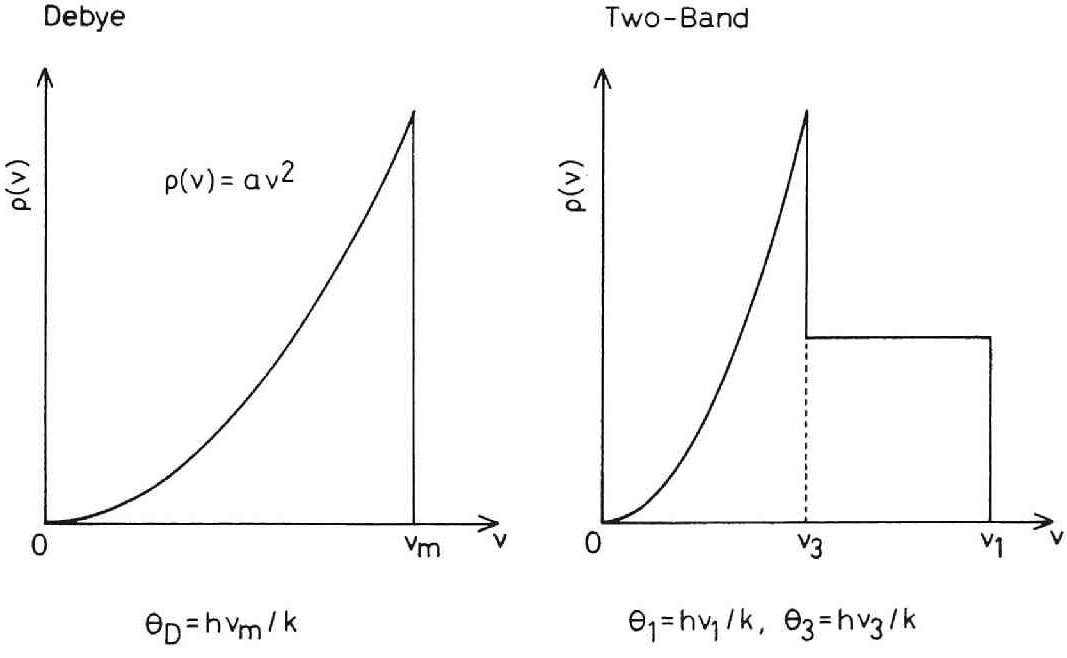

Fig.2.5 Schematic illustration of the vibrational density of states for Debye and two-band models.

$$f = \exp\{ -\frac{E_R}{2k\theta_1}[\ 3 + 4T(4/\theta_3 - 1/\theta_1) + \frac{\theta_1-\theta_3}{T+\theta_3/2}]\} \qquad (2.78)$$

or

$$\ln f = -\frac{E_R}{2k\theta_1}[\ 3 + 4T(4/\theta_3 - 1/\theta_1) + \frac{\theta_1-\theta_3}{T+\theta_3/2}]. \qquad (2.79)$$

Thus, by fitting the relative value of recoil-free fraction f/f_0 to Eq.(2.79), the two characteristic temperatures, θ_1 and θ_3, can be calculated. As an example, the result of analysis for amorphous $Fe_{83}B_{17}$ prepared by the melt-quenching method in the

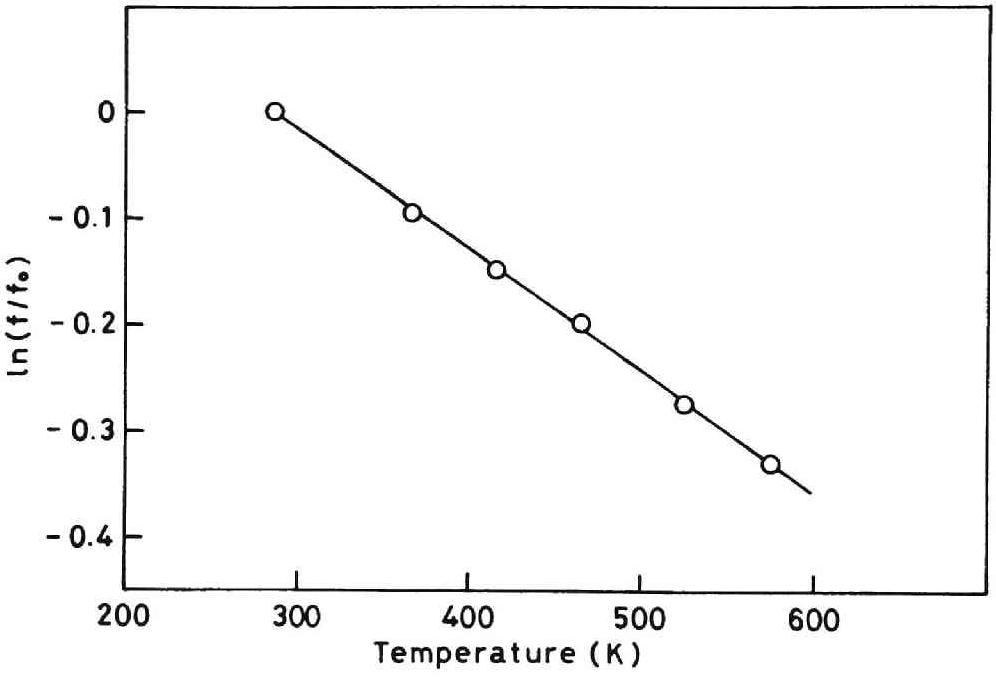

Fig.2.6 Natural logarithms of the normalized absorption area $\ln(f/f_0)$ as a function of temperature for an $Fe_{83}B_{17}$ amorphous alloy:o,experiment;-,calculated.

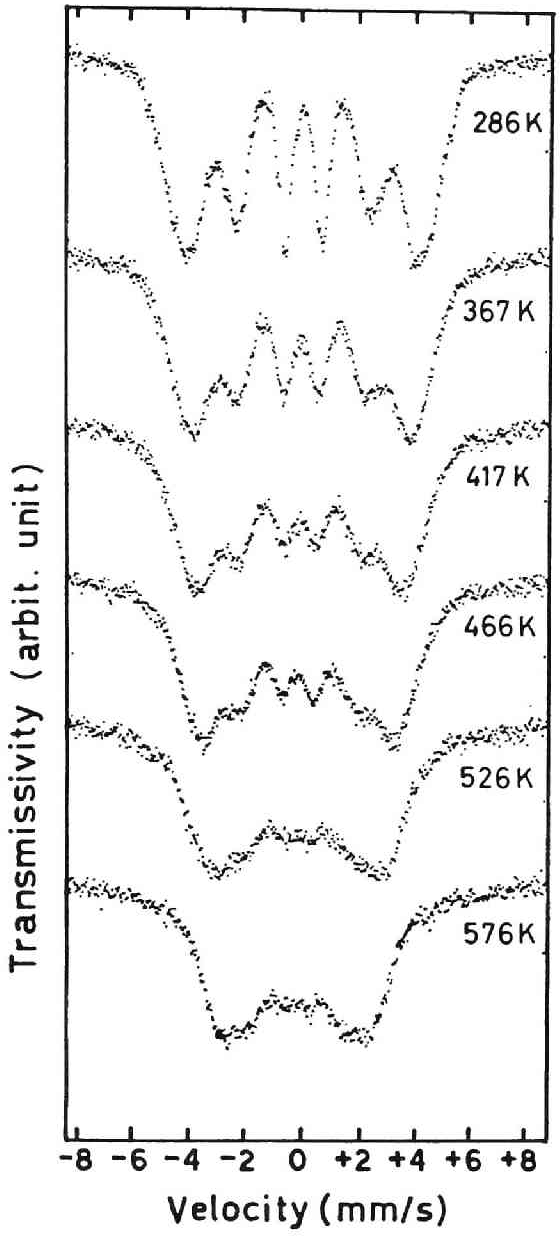

Fig.2.7 Mössbauer spectra obtained with an $Fe_{83}B_{17}$ amorphous alloy at several temperatures.

Table 2.1 The characteristic temperatures θ_1 and θ_3 obtained from Mössbauer measurements

Sample	θ_1(K)	θ_3(K)
$Fe_{83}B_{17}$	605	230
$Fe_{80}B_{20}$	655	185
$Fe_{80}P_{20}$	425	185

present investigation is shown in Fig.2.6. The recoil-free fraction was obtained as the absorption area ratio of the Mössbauer spectra presented in Fig.2.7. It is seen from Fig.2.6 that the theoretical curve agrees with the experimental data very well. The similar analysis was made on amorphous Fe-B and Fe-P alloys and the characteristic temperatures were calculated. The values are shown in Table 2.1.

2.2.2.2 Second-Order Doppler Shift

In general, the second-order Doppler shift, δ_D, is expressed by

$$\delta_D = - \frac{\langle v^2 \rangle}{2c^2} , \qquad (2.80)$$

where $\langle v^2 \rangle$ is the mean-square nuclear velocity of the absorbing nucleus and c the velocity of light. Since the average kinetic energy of the vibrations of nuclei is one-half of the total vibrational energy in a harmonic approximation, $\langle v^2 \rangle$ is ex-

pressed as

$$\langle v^2 \rangle = \frac{1}{NM} \sum_i \left(\frac{1}{2} + \langle n_i \rangle \right) h\nu_i , \qquad (2.81)$$

where N and M are the total number and the average mass of atoms, respectively, h the Planck constant, ν_i the phonon frequency, and $\langle n_i \rangle$ the statistical average of the vibrational quantum numbers. In the two-band model, the vibrational density of states is assumed to be given by Eq.(2.73). Then, the second-order Doppler shift can be derived as

$$\delta_D = -\frac{k}{2Mc^2} \left(\frac{6\theta_1^2 + 3\theta_3^2}{8\theta_1} + \frac{9T^4}{\theta_1 \theta_3^2} \int_0^{\theta_3/T} \frac{x^3}{e^x - 1} dx \right.$$

$$\left. + \frac{3T^2}{\theta_1} \int_{\theta_3/T}^{\theta_1/T} \frac{x}{e^x - 1} dx \right), \qquad (2.82)$$

since $\sum_i \langle n_i \rangle \nu_i$ is equal to $\int (e^{h\nu/kT} - 1)^{-1} \nu \rho(\nu) d\nu$. When θ_1 and θ_3 are set to be equal to the Debye temperature θ_D, Eq.(2.82) becomes the same equation derived from the Debye theory as follows:

$$\delta_D = -\frac{9k\theta_D}{16Mc^2} \left[1 + 8(T/\theta_D)^4 \int_0^{\theta_D/T} \frac{x^3}{e^x - 1} dx \right]. \qquad (2.83)$$

By using Eq.(2.82), the temperature dependence of the second-order Doppler shift δ_D can be calculated when θ_1 and θ_3 are known. In the experiment, δ_D cannot be obtained directly, because the observed spectrum shift δ includes the isomer shift (chemical shift) δ_{IS} in addition to the second-order Doppler shift δ_D. However, δ_{IS} is generally regarded as temperature independent, thus it is possible to compare δ_D with δ at different temperatures. An example of the analysis using Eq.(2.82)

is shown for the case of amorphous $Fe_{80}B_{20}$ in Fig.2.8. In order to obtain the spectrum shift, which is the sum of second-order Doppler shift and isomer shift, the experimental spectra shown in Fig.2.9 were decomposed into six Lorentzian curves so as to reproduce the spectra by shifting the positions of these curves after changing their intensity and linewidth. As seen from Fig. 2.8, the agreement between the theoretical and experimental results is fairly good. It is clear that the two-band model is effective for describing the second-order Doppler shift in amorphous iron alloys.

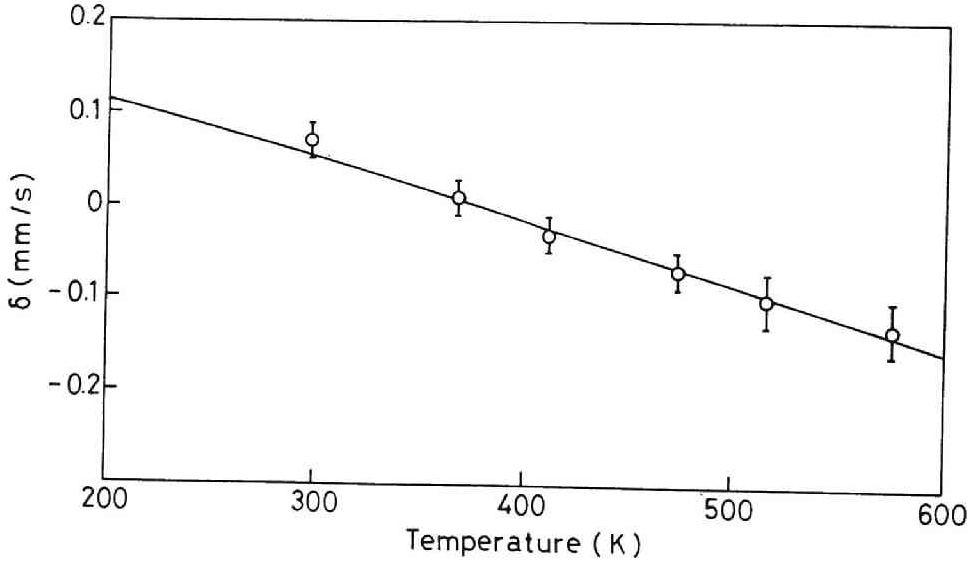

Fig.2.8 Temperature dependence of the spectrum shift for an $Fe_{80}B_{20}$ amorphous alloy:o,experiment;-,calculated.

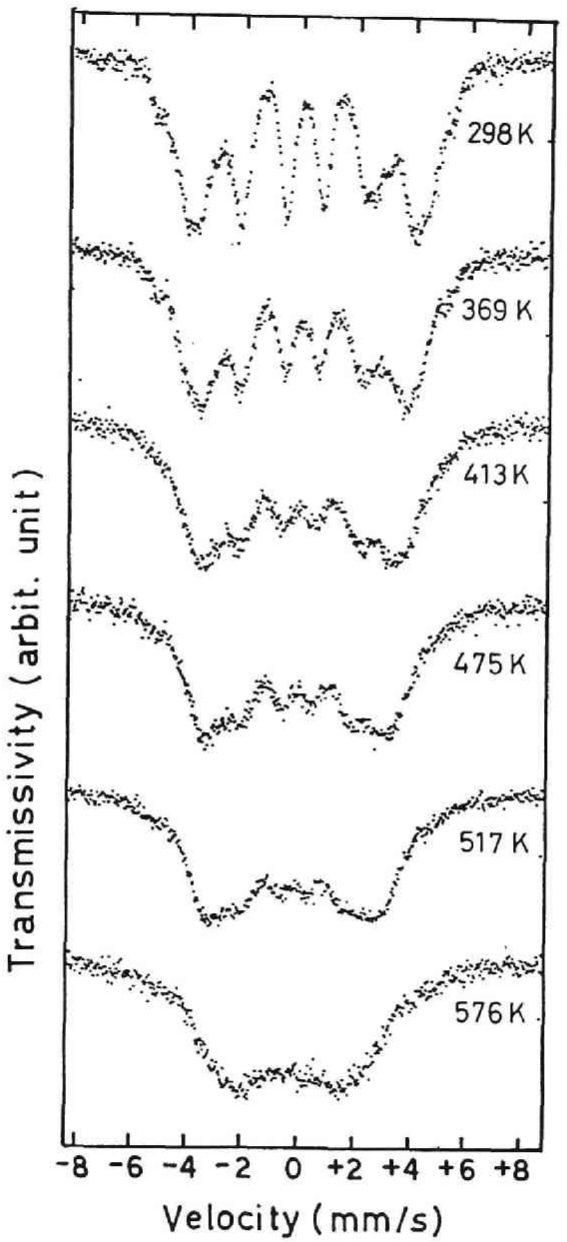

Fig.2.9 Mössbauer spectra obtained with an $Fe_{80}B_{20}$ amorphous alloy at several temperatures.

2.2.2.3 Isomer Shift

The energy difference between ground and excited states of nucleus is generally affected by the environment around the nucleus. When the energy differences between the ground and excited states of emitter and absorber are δ_e' and δ_a', respectively, the isomer shift is represented as follows:

$$\delta = \delta_a' - \delta_e'. \tag{2.84}$$

The energies of ground and excited states of nucleus are calculated by taking into account that the nucleus has a finite size. The distribution function of charge of the nucleus is assumed to be $e\rho_n(\mathbf{r}_n)$ with $\rho_n(\mathbf{r}_n)=0$ at $r_n \geq R$. Here R is an order of 10^{-13} cm. When the coordinate of the electron, r_e, is larger than R, the electrostatic interaction between the electron and the nucleus is the same as the case that the nucleus is a point charge. Hence, the interaction between the electron and the nucleus with a finite size is represented as follows:

$$\Delta E = -e^2 \int\int_{0 \leqq r_n, r_e \leqq R} \frac{\rho_n(\mathbf{r}_n)\rho_e(\mathbf{r}_e)}{|\mathbf{r}_n - \mathbf{r}_e|} d\mathbf{r}_n\, d\mathbf{r}_e$$

$$- \left(-Ze^2 \int_{0 \leqq r_e \leqq R} \frac{\rho_e(\mathbf{r}_e)}{r_e} d\mathbf{r}_e\right), \tag{2.85}$$

where $\rho_e(\mathbf{r}_e)$ is the distribution function and Z is the total charge of the nucleus written as follows:

$$Z = \int \rho_n(\mathbf{r}_n) d\mathbf{r}_n. \tag{2.86}$$

Since

$$\frac{1}{|\mathbf{r}_n - \mathbf{r}_e|} = \sum_{l=0}^{\infty} \frac{r_<^l}{r_>^{l+1}} P_l(\cos\alpha) \tag{2.87}$$

and

$$\int_0^{\pi} P_l(\cos\alpha)\sin\alpha\, d\alpha = \begin{cases} 2 & (l=0) \\ 0 & (l>0), \end{cases} \qquad (2.88)$$

where $P_l(\cos\alpha)$ is the Legendre's polynominal, Eq.(2.85) leads to the next equation:

$$\Delta E = \frac{2\pi}{3} Ze^2 |\phi(0)|^2 \langle r_n^2 \rangle, \qquad (2.89)$$

where $\rho_e(r_e)$ is assumed to be equal to $|\phi(0)|^2$ and

$$\langle r_n^2 \rangle = \frac{1}{Z} \int r_n^2 \rho_n(r_n) dr_n. \qquad (2.90)$$

Since $\langle r_n^2 \rangle$ for the excited state is different from that for the ground state, the energy difference between ground and excited states is expressed as follows:

$$\delta' = \frac{2\pi}{3} Ze^2 |\phi(0)|^2 [\langle r_n^2 \rangle_e - \langle r_n^2 \rangle_g], \qquad (2.91)$$

where $\langle r_n^2 \rangle_g$ and $\langle r_n^2 \rangle_e$ denote the average radius of the nucleus in ground and excited states, respectively. Finally, the isomer shift is represented as follows:

$$\delta = \frac{2\pi}{3} Ze^2 [|\phi_a(0)|^2 - |\phi_e(0)|^2][\langle r_n^2 \rangle_e - \langle r_n^2 \rangle_g]. \qquad (2.92)$$

Therefore, we can obtain information about the electron density at the nucleus from the isomer shift.

2.2.2.4 Quadrupole Splitting

The quadrupole interaction arises from the fact that the nucleus is not a sphere. Let's consider the nucleus in the electrostatic potential, V(r), due to the electrons. When the

electrons are far enough from the nucleus, V(r) can be expanded as follows:

$$V(\mathbf{r}) = V(0) + \sum_i x^i \left(\frac{\partial V}{\partial x^i}\right)_0 + \frac{1}{2}\sum_{i,k} x^i x^k \left(\frac{\partial^2 V}{\partial x^i \partial x^k}\right)_0 + \quad . \tag{2.93}$$

The interaction between the nucleus and the electrons is obtainable as the integral of the product of Eq.(2.93) and the charge distribution of the nucleus, $e\rho_n(\mathbf{r}_n)$. Since

$$\rho_n(\mathbf{r}_n) = \rho_n(-\mathbf{r}_n) \tag{2.94}$$

is known from the experiments, the interaction is expressed as follows:

$$E = E_0 + E_2, \tag{2.95}$$

where

$$E_0 = e\int \rho_n(\mathbf{r}_n)V(0)d\mathbf{r}_n \tag{2.96}$$

and

$$E_2 = \frac{e}{2}\sum_{i,k} \left(\frac{\partial^2 V}{\partial x^i \partial x^k}\right)_0 \int \rho_n(\mathbf{r}_n)x^i x^k d\mathbf{r}_n. \tag{2.97}$$

E_0 is the energy when the nucleus is assumed to be point charge.

The charge distribution of the nucleus is defined as

$$e\rho_n(\mathbf{r}_n) = \langle\psi_n(\mathbf{r}_1, \quad ,\mathbf{r}_A)\left|\sum_{p=1}^{A} e_p\delta(\mathbf{r}-\mathbf{r}_p)\right|\psi_n\rangle, \tag{2.98}$$

where ψ_n is the nuclear wave function, $\mathbf{r}_1$, , $\mathbf{r}_A$ are the nucleon position vectors and the charge e_p=e for protons and e_p=0 for neutrons. By substituting Eq.(2.98) into Eq.(2.97), the next equation is derived:

$$E_2 \quad \frac{e}{6}\sum_i \left(\frac{\partial^2 V}{\partial x^i \partial x^i}\right)_0 \langle\psi_n|\sum_p r_p^2|\psi_n\rangle$$

$$+\frac{e}{6}\sum_{i,k}\left(\frac{\partial^2 V}{\partial x^i\,\partial x^k}\right)_0 \langle\psi_n|\sum_p (3x_p^i x_p^k - r_p^2\delta_{ik})|\psi_n\rangle. \qquad (2.99)$$

The first term in Eq.(2.99) yields the isomer shift and the second term represents the quadrupole interaction. By using the Wigner-Eckart theorem, the next relation is derived:

$$\sum_p (3x_p^i x_p^k - r_p^2\delta_{ik}) \quad A\left[\frac{3}{2}(I_iI_k + I_kI_i) - I(I+1)\delta_{ik}\right]. \qquad (2.100)$$

The quadrupole moment, Q, is defined as the T_{33} component of the tensor in the left hand of Eq.(2.100) with $I_z=I$. Therefore,

$$Q = AI(2I-1) \qquad (2.101)$$

is derived. By using Eqs.(2.100) and (2.101), the second term in the right hand of Eq.(2.99) is expressed as follows:

$$E_Q \quad \frac{eQ}{6I(2I-1)}\sum_{i,k}\left(\frac{\partial^2 V}{\partial x^i\,\partial x^k}\right)_0 \left[\frac{3}{2}(I_iI_k + I_kI_i) - I(I+1)\delta_{ik}\right]. \qquad (2.102)$$

By using the Laplace equation and the asymmetry parameter, η, defined as

$$\eta = \frac{V_{xx}-V_{yy}}{V_{zz}} \qquad (2.103)$$

for $|V_{zz}|\geq|V_{yy}|\geq|V_{xx}|$, Eq.(2.102) is rewritten as follows:

$$E_Q = \frac{e^2qQ}{4I(2I-1)}\left[3I_z^2 - I(I+1) + \frac{\eta}{2}(I_+^2 + I_-^2)\right], \qquad (2.104)$$

where q is defined as

$$eq = V_{zz} \qquad (2.105)$$

and designated the electric field gradient, and I_+ and I_- have their usual meanings. Eq.(2.104) represents the energy resulting

from the non-spherical shape of the nucleus. For ^{57}Fe, I=3/2 for the excited state. In this case, the eigenvalues of Eq.(2.104) are obtained from the next secular equation:

$$\begin{vmatrix} 3-E & 0 & \sqrt{3}\eta & 0 \\ 0 & -3-E & 0 & \sqrt{3}\eta \\ \sqrt{3}\eta & 0 & -3-E & 0 \\ 0 & \sqrt{3}\eta & 0 & 3-E \end{vmatrix} = 0. \qquad (2.106)$$

The result is as follows:

$$E_{3/2,-3/2} = \frac{1}{4}e^2qQ(1+\eta/3)^{1/2}$$

$$E_{1/2,-1/2} = -\frac{1}{4}e^2qQ(1+\eta/3)^{1/2} \quad . \qquad (2.107)$$

As the result, the spectrum is splitted.

2.2.2.5 Hyperfine Field

The magnetic interaction between the magnetic moment due to nuclear spin and that due to electron spin is expressed as follows:

$$H_{mag} = 2\mu_B \mathbf{s} \cdot \mathrm{rot}(\mu \times \frac{\mathbf{r}}{r^3})$$

$$= 2\mu_B[(\mathbf{s}\cdot\nabla)(\mu\cdot\nabla)-(\mathbf{s}\cdot\mu)\nabla^2](\frac{1}{r}), \qquad (2.108)$$

where μ is the magnetic moment of the nuclear spin, $\mathbf{s}$ is the electron spin and μ_B is Bohr magneton. For $r \neq 0$, H_{mag} is given as the dipolar interaction:

$$H_d \quad (-2\mu_B)[\frac{(\mathbf{s}\cdot\mu)}{r^3} - \frac{3(\mu\cdot\mathbf{r})(\mathbf{s}\cdot\mathbf{r})}{r^5}], \qquad (2.109)$$

because $\nabla^2(1/r)=0$. For the complete description of Eq.(2.108), the case that r=0 should be involved. For that purpose, the next integral is considered:

$$\int \frac{1}{r}\left(\frac{\partial^2\phi}{\partial x^2}\right) dr = -\frac{4\pi\phi(0)}{3} + \int \left(\frac{\partial^2}{\partial x^2}\frac{1}{r}\right)\phi \, dr, \quad (2.110)$$

where $\phi(\mathbf{r})$ is an arbitrary function which is differentiable. When the partial differential of a distribution T is written as $(\partial T/\partial x)_{dist.}$, Eq.(2.110) can be rewritten as follows:

$$\left(\frac{\partial^2}{\partial x^2}\frac{1}{r}\right)_{dist.} = -\frac{4\pi}{3}\delta(\mathbf{r}) + \frac{\partial^2}{\partial x^2}\frac{1}{r} \quad . \quad (2.111)$$

Eq.(2.111) also holds for variables y and z. Also, when the x and y axes are transformed into x' and y' axes by the rotation of $\pi/4$ around the z axis, the next relation holds:

$$\frac{\partial^2}{\partial x \partial y} = \frac{1}{2}\left(\frac{\partial^2}{\partial x'^2} - \frac{\partial^2}{\partial y'^2}\right). \quad (2.112)$$

From Eqs.(2.111) and (2.112), the next relation is derived:

$$\left(\frac{\partial^2}{\partial x \partial y}\frac{1}{r}\right)_{dist.} = \frac{\partial^2}{\partial x \partial y}\frac{1}{r} \quad . \quad (2.113)$$

Eq.(2.113) also holds for the other combinations of x, y and z. By using Eqs.(2.111) and (2.113) with Eq.(2.108), the next equation is derived:

$$H_{mag} = (16\pi/3)\mu_B(\mathbf{s}\cdot\mu)\delta(\mathbf{r}) + H_d. \quad (2.114)$$

The first term of Eq.(2.114) is called the Fermi's contact interaction and yields the hyperfine structure in the Mössbauer spectrum. As clearly seen from Eq.(2.114), only s-electrons contrib-

ute to the contact interaction. The reason why the s-orbitals, each of which is filled with paired electrons, bring about magnetic fields is ascribed to the exchange interaction between s- and d-electrons. Since the s-electrons which possess spin parallel to that of d-electrons can not stay nearby the d-electrons according to the Pauli's exclusion principle, the Coulomb's repulsion force between the s- and d-electrons is not very large. On the other hand, the s-electrons the spin of which is antiparallel to that of d-electrons are affected by the repulsion force more largely. As a result, the density of s-electrons having the antiparallel spin is larger than that of s-electrons having the parallel spin at the nucleus, leading to the magnetic field at the nucleus. This magnetic field splits the energy levels of the nucleus according to Zeeman effect, and therefore, splits the observed Mössbauer spectrum.

2.3 Conclusions

For the purpose of clarifying the cluster spin glass-like (mictomagnetic) behavior observed in iron-based amorphous oxides and fluorides, the concept of Shtrikman and Wohlfarth, which treats the magnetic transition of these amorphous solids as the superparamagnetism by considering the temperature dependence of the size of superparamagnetic clusters and existence of the intercluster interaction, was modified by assuming several types of distribution function of the superexchange interaction between Fe^{3+} ions, that is, delta function-like, parabolic and Gaussian distribution functions. It was derived from the present model that the spin-freezing temperature increases monotonically with increasing the average value of the superexchange interaction for all the distributions examined. This fact led to the inference that the spin-freezing temperature increases monotonically with increasing the covalency of Fe-X (X:O, F) bond because the magnitude of superexchange interaction is proportional to the covalency. This inference will be ascertained in the next chapter.

In the present chapter, the principle of ESR and Mössbauer measurements was also described. For the ESR, factors which have an influence on the linewidth of the ESR spectrum and the physical meaning of g-value were outlined. For the Mössbauer measurements, important parameters, that is, recoil-free fraction, second-order Doppler shift, isomer shift, quadrupole splitting and hyperfine field were reviewed. In particular, theoretical expression of temperature dependence of recoil-free fraction and second-order Doppler shift was derived for the first time for the two-band model which is more suitable for the description of

phonons in amorphous solids than the Debye model.

References

1) R.A.Verhelst, R.W.Kline, A.M. de Graaf and H.O.Hooper, Phys. Rev., **B11**, 4427 (1975)

2) H.R.Rechenberg, L.H.Bieman, F.S.Huang and A.M. de Graaf, J. Appl. Phys., **49**, 1638 (1978)

3) J.P.Jamet, J.C.Dumais, J.Seiden and K.Knorr, J. Magn. Magn. Mat., **15-18**, 197 (1980)

4) E.P.Wohlfarth, J. Phys., **F10**, L241 (1980)

5) S.K.Burke, R.Cywinski, J.R.Davis and B.D.Rainford, J. Phys., F13, 451 (1983)

6) L.Nèel, Rev. Mod. Phys., **25**, 293 (1953)

7) T.Goto and T.Kanomata, J. Appl. Phys., **57**, 3450 (1985)

8) J.P.Sanchez, J.M.Friedt, R.Horne and A.J. van Duyneveldt, J. Phys., C17, 127 (1984)

9) S.Shtrikman and E.P.Wohlfarth, Phys. Lett., **85A**, 467 (1981)

10) S.Shtrikman and E.P.Wohlfarth, J. Magn. Magn. Mat., **31-34**, 1421 (1983)

11) G.Ferey, F.Varret and J.M.D.Coey, J. Phys., C12, L531 (1979)

12) M.E.Lines, Phys. Rev., **B20**, 3729 (1979)

13) M.Eibschütz, M.E.Lines, L.G. van Ultert, H.J.Guggenheim and G.J.Zydzik, Phys. Rev., B29, 3843 (1984)

14) P.W.Anderson, Phys. Rev., **79**, 350 (1950)

15) J.Kanamori, Magnetism (Baifukan Ltd., Tokyo, 1969), p.56 (in Japanese)

16) J.Kanamori, J. Phys. Chem. Solids, **10**, 87 (1959)

17) M.Date, Electron Spin Resonance (Baifukan Ltd., Tokyo, 1978), p.29 (in Japanese)

18) S.Chikazumi, Physics of Ferromagnetism, Vol. I (Syokabo Ltd., Tokyo, 1978), p.77 (in Japanese)

19) R.L.Mössbauer, Z. Phys., **151**, 124 (1958)

20) R.V.Pound and G.A.Rebka,Jr., Phys. Rev. Lett., **3**, 439 (1959)

21) A.Einstein, Ann. Phys., **49**, 769 (1916)

22) R.V.Pound and G.A.Rebka,Jr., Phys. Rev. Lett., **4**, 337 (1960)

23) P.J.Debye, Ann. Phys., **39**, 789 (1912)

24) V.V.Tarassov, Zh. Fiz. Khim, **24**, 111 (1950)

25) M.Blackman, Handbuch der Physik (Springer, Berlin, 1955), Vol. VIII-1, p.325

26) W.DeSorbo, J. Chem. Phys., **21**, 1144 (1953)

27) K.Hirao, N.Soga and M.Kunugi, J. Am. Ceram. Soc., **62**, 570 (1979)

28) N.Soga, J. de Phys., **43**, C9-557 (1982)

29) N.Soga, J. Non-Cryst. Solids, **52**, 365 (1982)

30) K.Hirao, K.Kimura and N.Soga, The Fourth Japan Symposium on Thermophysical Properties 1983, edited by A.Nagashima (The Japan Society of Thermophysical Properties, Yokohama, 1983), p.51

31) M.F.Taragin, J.C.Eisenstein and W.Haller, Phys. Chem. Glasses, **13**, 149 (1972)

32) N.Saegusa and A.H.Morrish, Phys. Rev., **B26**, 10 (1982)

33) G.A.Sawatzky, F.van der Woude and A.H.Morrish, Phys. Rev., **183**, 383 (1969)

CHAPTER 3

APPLICATION OF THE THEORY TO IRON-CONTAINING OXIDE AND FLUORIDE GLASSES

As mentioned in the previous chapter, it is expected that the spin-freezing temperature increases with increasing the covalency of Fe^{3+}-O and Fe^{3+}-F bonds when the concentration of Fe^{3+} and the distribution width of the superexchange interaction are constant. The isomer shift appearing in the Mössbauer spectrum is closely related to the covalency of Fe^{3+}-O and Fe^{3+}-F bonds,[1),2)] being able to be used as a good parameter of the covalency. The linear relationship between 4s electron density at the nucleus of Fe^{3+} ion and the isomer shift was theoretically shown by Walker, Wertheim and Jaccarino.[1)] Hence, it is expected that the spin-freezing temperature of several oxide and fluoride glasses can be described in terms of the isomer shift value. In the present chapter, an attempt is made to apply the theoretical result derived in the previous chapter to the present oxide and fluoride glasses containing iron so as to clarify the relation between the spin-freezing temperature and the glass composition. Furthermore, the frequency dependence of the spin-freezing temperature and the temperature dependence of the susceptibility observed for several iron-containing oxide and fluoride glasses are explained within the framework of the present model. Finally, the model is applied to explicate the magnetism of amorphous oxides in the CaO-Bi_2O_3-Fe_2O_3 system which show ferromagnetic character.

3.1 Effect of Composition on Spin-Freezing Temperature

In Table 3.1, the values of the isomer shift for some iron-based amorphous oxides and fluorides studied so far[3)-14)] are summarized as well as the spin-freezing temperature. The isomer shifts for $44Fe_2O_3 \cdot 56P_2O_5$, $11.8Fe_2O_3 \cdot 29.4PbO \cdot 58.8B_2O_3$ and $11.9Fe_2O_3 \cdot 45.2Li_2O \cdot 42.9B_2O_3$ glasses are the new data measured in the present work. These oxide glasses were prepared by using the conventional melting-and-quenching method. Representative Mössbauer spectra of $44Fe_2O_3 \cdot 56P_2O_5$ and $11.8Fe_2O_3$ $29.4PbO \cdot 58.8B_2O_3$ glasses are shown in Fig.3.1. It is seen that the major parts of the iron ions are in Fe(III) state in these oxide glasses.

The relation between the spin-freezing temperature and isomer shift value for those materials in Table 3.1 is shown in Fig.3.2. In order to take into consideration the difference in the concentration of iron ions among these amorphous oxides, the term $T_f/(c-c')$, where c stands for the concentration of iron ion expressed as the atomic ratio of the cation and c' corresponds to the concentration where T_f becomes zero, is plotted as ordinate in this figure. The parameter c' presents also the concentration where the clusters of iron ions start to form in the glass. The value of c' has been estimated for several oxide glass systems. For example, Mendiratta et al.[7)] found c' to be 0.036 for Fe_2O_3-NiO-PbO-B_2O_3 system by applying ac susceptibility measurements. Moon et al.[15)] examined the formation of the cluster of Fe^{3+} ions in Fe_2O_3-BaO-B_2O_3 glasses by means of magnetization and ESR measurements and estimated c'=0.033. For Fe_2O_3-Li_2O-B_2O_3

Table 3.1 The spin-freezing temperature (T_f) and the isomer shift (IS) for iron-based oxide and fluoride glasses

Glass composition	T_f(K)	Ref.*	IS(mm/s)	Ref.**
$39Fe_2O_3$ $48BaO \cdot 13B_2O_3$	70[a]	3)	0.24	4)
$30Fe_2O_3 \cdot 45BaO \cdot 25B_2O_3$	14[b], 38[c]	6)	0.25	5)
$11.8Fe_2O_3 \cdot 29.4PbO \cdot 58.8B_2O_3$	4.0[d]	7)	0.36	this work[h]
$11.9Fe_2O_3 \cdot 45.2Li_2O \cdot 42.9B_2O_3$	3.3[e], 7[a]	8)	0.28	this work
$44Fe_2O_3 \cdot 56P_2O_5$	7[g]	9)	0.41	this work
$Y_3Fe_5O_{12}$	40[g]	10)	0.31	10)
Fe_2O_3	80	11)	0.32	11)
$PbMnFeF_7$	11.77[f]	12),13)	0.45	14)
Pb_2MnFeF_9	5.26[f]	12),13)	0.43	14)

*References for the spin-freezing temperature, **References for the isomer shift value, a: Mössbauer effect, b: thermoremanent effect, c-f: ac susceptibility(c:70Hz, d:83Hz, e:17.3Hz, f:75Hz), g: dc susceptibility

h: These glasses were prepared by using Fe_2O_3, PbO, Li_2CO_3, B_2O_3 and $(NH_4)_2HPO_4$ as the raw materials. They were mixed and melted at 1000 to 1200 °C in air. The melt was quenched with a twin-roller for lithium borate glass and with an iron plate for the other glasses. The Mössbauer measurements were carried out at room temperature by using a 370 MBq ^{57}Co in Rh as the γ-ray source. The calculation of the isomer shift was done by using the spectrum of α-Fe foil at room temperature.

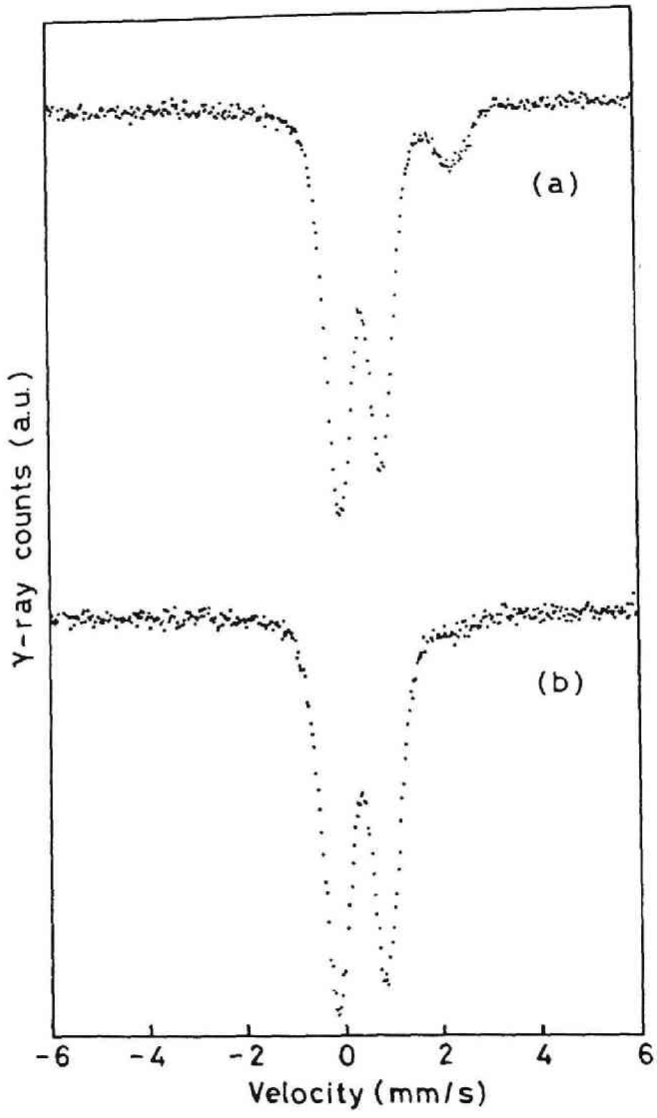

Fig.3.1 Mössbauer spectra for (a)$44Fe_2O_3 \cdot 56P_2O_5$ and (b)$11.9Fe_2O_3 \cdot 45.2Li_2O \cdot 42.9B_2O_3$.

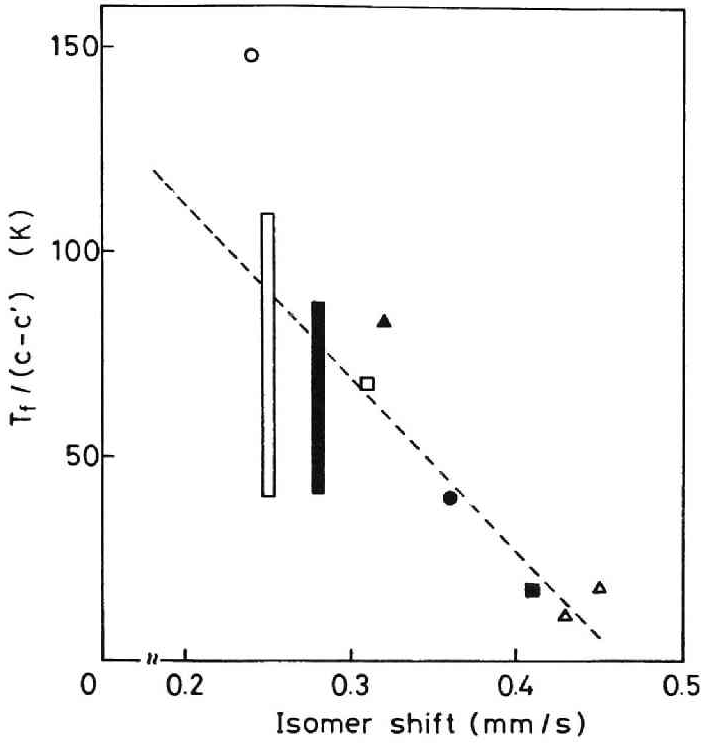

Fig.3.2 Relation between the spin-freezing temperature and the isomer shift for Fe^{3+}-containing insulating glasses. Since the spin-freezing temperature is dependent on the method of measurements, the temperature range where the spin-freezing is observable is indicated for a few of glasses. The broken line is to guide the eyes. (○ and open bar: Fe_2O_3-BaO-B_2O_3, closed bar: Fe_2O_3-Li_2O-B_2O_3, ● : Fe_2O_3-PbO-B_2O_3, □ : Y_2O_3-Fe_2O_3, ■ : Fe_2O_3-P_2O_5, ▲ : Fe_2O_3, △ : PbF_2-MnF_2-FeF_3)

system, c'=0.061 was revealed by Mössbauer measurements at 4.2 K.[8] In the present study, the value of c' is assumed to be 0.04, which is compatible with above-mentioned values. The parameter $T_f/(c-c')$ is considered appropriate as the first approximation, because the linear relation between T_f and c-c' was experimentally observed for cluster spin glasses.[16),17)] The trend that $T_f/(c-c')$ increases with decreasing the isomer shift seen from Fig.3.2 indicates that the spin-freezing temperature increases with increasing the covalency or the superexchange interaction between iron ions. Thus, the present model seems to be appropriate to describe the effect of glass composition on the spin-freezing temperature for these iron-based oxide and fluoride glasses.

3.2 Measuring Frequency Dependence of Spin-Freezing Temperature

It is known that Vogel-Fulcher empirical law[18),19)] well describes the relation between the spin-freezing temperature and the measuring frequency for iron-based oxide and fluoride glasses[7),8),20)-22)] as well as metallic spin glasses.[23)] Namely, measuring frequency ν is related to the spin-freezing temperature as follows:

$$\nu = \nu_0 \exp[-\frac{E}{k(T_f - T_0)}], \tag{3.1}$$

where E is the activation energy for the rotation of the magnetic moment within the cluster. When this equation is applied for the data of $11.9Fe_2O_3 \cdot 45.2Li_2O \cdot 42.9B_2O_3$ glass, T_0 becomes 2.7 K.[8)]

In the model presented in Chapter 2, the relation between the spin-freezing temperature and the measuring frequency is represented as the next form for the weak coupling regime (See Eq.(2.17)):

$$\nu = \nu_0 \exp[-(E_K + \frac{E_i^2}{kT_f})/kT_f], \tag{3.2}$$

where

$$E_K \quad Kv = kT_K \tag{3.3}$$

and

$$E_i^2 = \int m^2 M^2 v^2 J^2 f(J)\, dJ. \tag{3.4}$$

When T_0 is defined as

$$kT_0 = E_i^2 / E_K. \tag{3.5}$$

Eq.(3.2) is transformed into the next equation for $T_0/T_K >> 1$ which is the condition for the weak coupling regime:

$$\nu = \nu_0 \exp[-Kv/k(T_f - T_0)]. \qquad (3.6)$$

Eq.(3.6) is identical to Eq.(3.1), that is, Vogel-Fulcher law.

On the other hand, the measuring frequency dependence of the spin-freezing temperature depends on the distribution function of superexchange interaction, J, for the strong coupling regime. Here, we pay attention to only the delta function-like distribution. In this case, the measuring frequency dependence of the spin-freezing temperature is represented by Eq.(2.30). By using this equation with appropriate value for B_1 and J_0=3.0 K, the experimental data of $11.9Fe_2O_3 \cdot 45.2Li_2O \cdot 42.9B_2O_3$ glass can be well analyzed. The result of the analysis is shown in Fig.3.3. The value of J_0 obtained is almost identical to T_0 given when

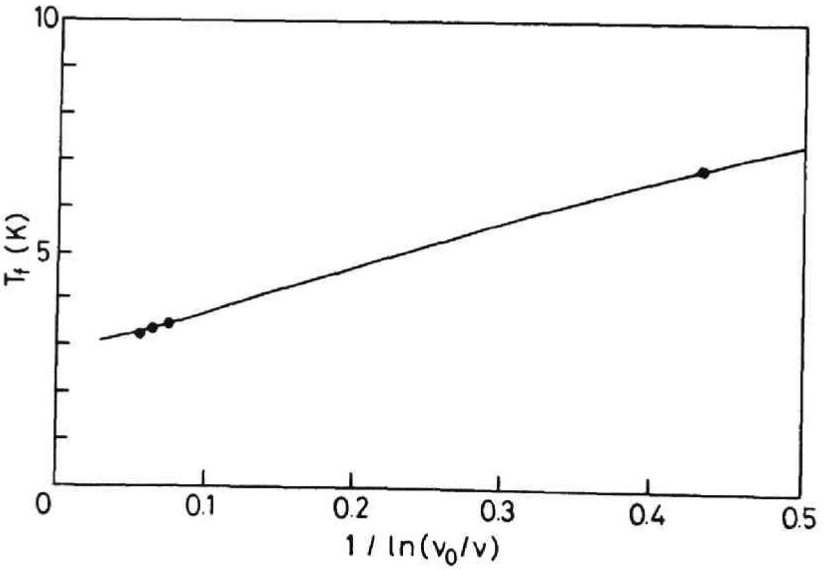

Fig.3.3 The measuring frequency dependence of the spin-freezing temperature for $11.9Fe_2O_3 \cdot 45.2Li_2O \cdot 42.9B_2O_3$ glass. The solid curve is drawn by using Eq.(2.30) (see text).

Eq.(3.1) is applied.[8] The activation energy for the rotation of the clusters decreases with temperature in the present model, which is clearly seen from Fig.3.3, because the cluster size increases with temperature,. Furthermore, as clearly seen from this figure, the agreement of the experimental data and the curve calculated from Eq.(2.30) is rather good.

Figure 3.4 shows the result of the similar analysis on $51.8FeO \cdot 5.8Al_2O_3 \cdot 42.4SiO_2$ glass.[22] Here, J_0=7.6 K was used when the data were analyzed. The good agreement between the experimental data and the calculated curve is observable. Thus, it is concluded that the present model is also effective for ex-

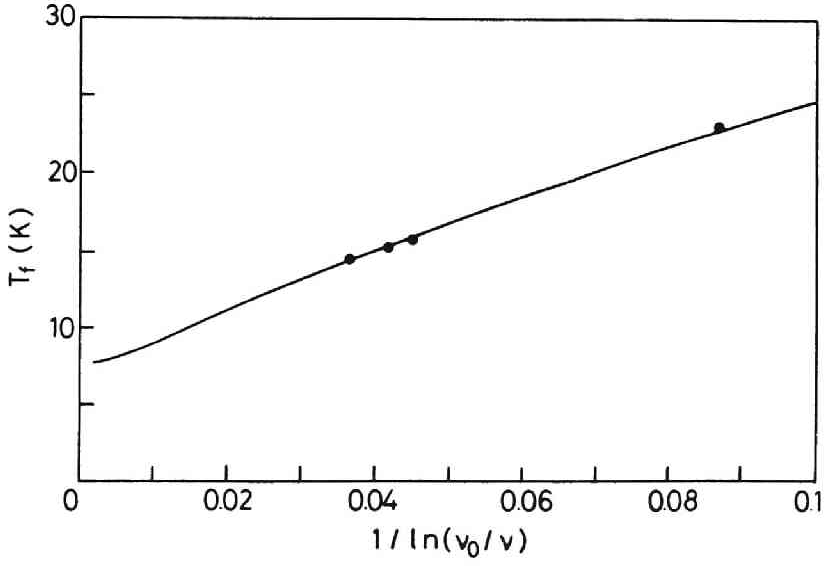

Fig.3.4 The measuring frequency dependence of the spin-freezing temperature for $51.8FeO \cdot 5.8Al_2O_3 \cdot 42.4SiO_2$ glass. The solid curve is drawn by using Eq.(2.30) (see text).

planation of the measuring frequency dependence of spin-freezing temperature for the strong coupling regime as well as for the weak coupling regime.

3.3 Temperature Dependence of Susceptibility

The behavior of the susceptibility as a function of temperature for amorphous iron oxides and fluorides greatly depends on the region of the temperature. At high temperatures much above the spin-freezing temperature, the inverse susceptibility decreases linearly with decreasing the temperature and the effective magnetic moment obtained from the slope of the line corresponds to the spin-only value for Fe^{3+}. In other words, the system is in a paramagnetic state described by the Curie-Weiss law. In the region of nearly above the spin-freezing temperature, the inverse susceptibility vs. temperature curve deviates from the Curie-Weiss law, with the effective magnetic moment being smaller. In this region, the system is superparamagnetic. Below the spin-freezing temperature, the susceptibility decreases with decreasing the temperature as a result of the freezing of the superparamagnetic clusters. The susceptibility vs. temperature curves obtained experimentally for several amorphous iron oxides and fluorides are shown in Figs.3.5 and 3.6. In Fig.3.5, specimens for which the inverse susceptibility vs. temperature curve exhibits upward curvature in the superparamagnetic region are shown. On the contrary, the curves of the specimens shown in Fig.3.6 exhibit downward curvature.

In the simple superparamagnetism, the temperature dependence of the susceptibility for the superparamagnets at high temperatures is expressed as follows:

$$\chi = N(M_S V)^2/3kT, \tag{3.7}$$

where χ is the susceptibility, N, M_S and V are the number,

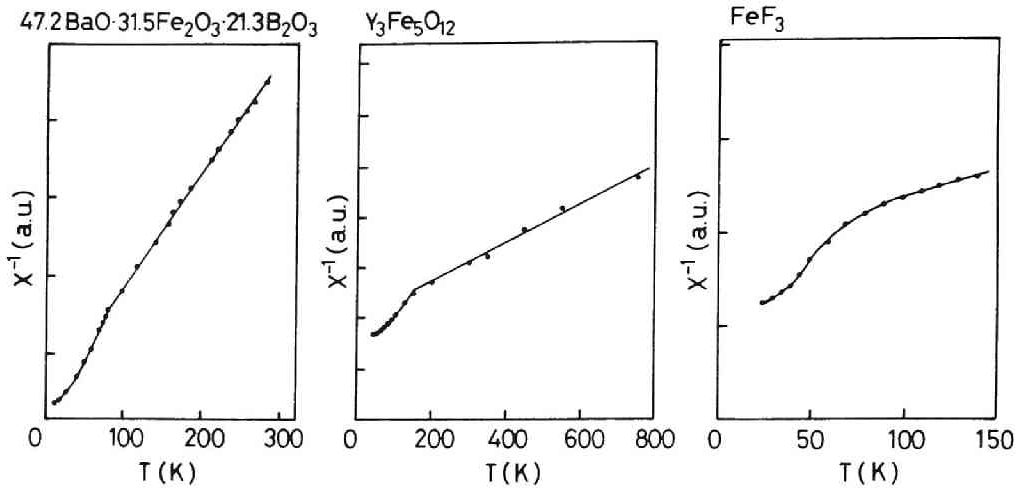

Fig.3.5 The temperature dependence of the susceptibility for several oxide and fluoride glasses. The inverse susceptibility vs. temperature curve in the superparamagnetic region shows the upward curvature.

saturation magnetization and volume of the superparamagnetic particles, respectively. In the strong coupling regime in the present model, the volume of the cluster has the temperature dependence represented by the next relation:

$$V \propto T^{-1} \tag{3.8}$$

Namely, the volume increases with decreasing the temperature. The number of the cluster is expected to decrease as the temperature decreases nearly above the spin-freezing temperature because in this temperature region, a larger cluster comes to incorporate smaller ones. Besides, it is expected that the saturation magnetization decreases with decreasing the tempera-

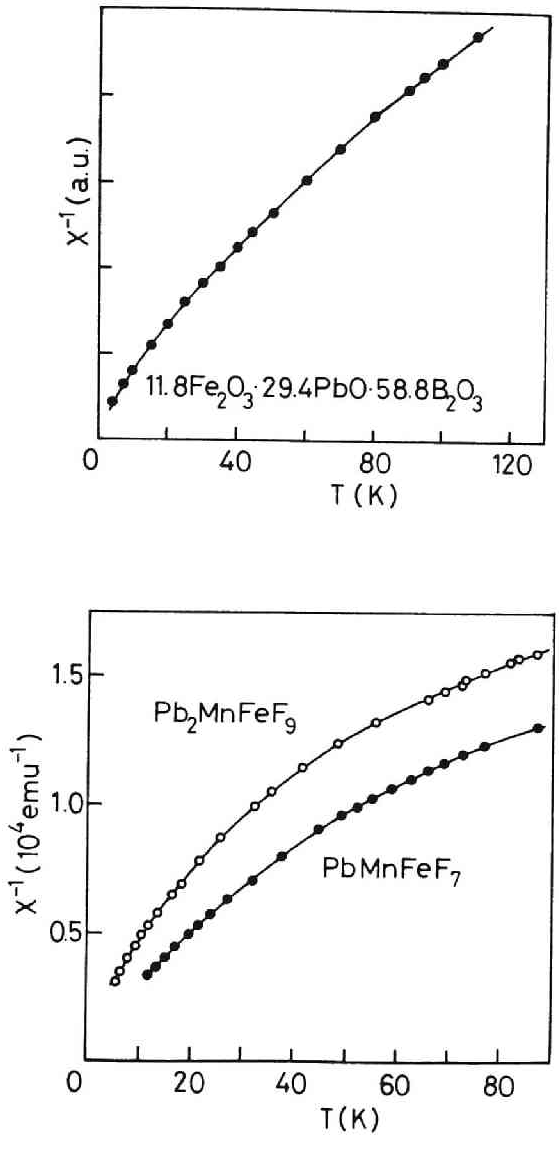

Fig.3.6 The temperature dependence of the susceptibility for several oxide and fluoride glasses. The inverse susceptibility vs. temperature curve in the superparamagnetic region shows the downward curvature.

ture since the negative superexchange interaction is dominant among the spins within the cluster. Therefore, the term $N(M_sV)^2$ in Eq.(3.7) positively depends on temperature. Thus, when

$$\log_T[N(M_sV)^2] > 0, \tag{3.9}$$

the χ^{-1} versus T curve shows upward curvature and when

$$\log_T[N(M_sV)^2] < 0, \tag{3.10}$$

the curve shows downward curvature. These curves are schematically illustrated in Fig.3.7. It is found that the experimental curves shown in Figs.3.5 and 3.6 are explainable in terms of Eqs.(3.9) and (3.10), respectively. In other words, the temperature dependence of the susceptibility, especially in the superparamagnetic region, is describable qualitatively within the framework of the present modified superparamagnetic model.

When Fig.3.7 is compared with Figs.3.5 and 3.6, it is seen that the glasses with lower and higher contents of iron tend to satisfy Eqs.(3.9) and (3.10), respectively. In the glasses with lower content of iron, the number and the volume of clusters do not depend on temperature so strongly. Hence, the temperature dependence of the magnetization affects most largely the temperature dependence of the susceptibility. It is expected that the magnetization decreases with decreasing the temperature as described above. As a result, the temperature dependence of the susceptibility is represented by Eq.(3.9). On the other hand, it is expected that in the glasses with higher content of iron, the volume varies with temperature in accordance with Eq.(3.8). This temperature dependence of the volume brings about the T^3 dependence of χ^{-1}. It is thought that the variation of the volume is the most dominant in the variation of susceptibility with tem-

$$\chi = \frac{1}{3} N (M_s V)^2 / kT$$

1) $\log_T N(M_s V)^2 < 0$

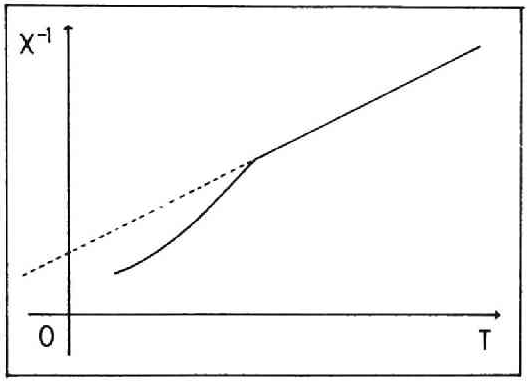

2) $\log_T N(M_s V)^2 > 0$

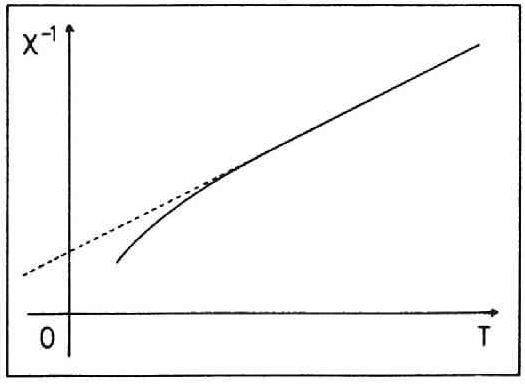

Fig.3.7 Schematic illustrations of the temperature dependence of the susceptibility derived from the present model.

perature. This leads to the temperature dependence of the susceptibility represented by Eq.(3.10).

3.4 Application to Amorphous Oxides of Ferromagnetic Character

Recently, ferromagnetic character with Curie temperature higher than room temperature has been revealed in several amorphous oxides such as $ZnO-Bi_2O_3-Fe_2O_3$,[24] $CaO-Bi_2O_3-Fe_2O_3$,[25,26] and $(La_{1-x}Sr_x)MnO_3-B_2O_3$[27] systems. They are interesting substances considering that in most of the iron- or manganese-containing oxide glasses reported thus far, the predominant interaction among magnetic ions is antiferromagnetic. The previous studies on amorphous oxides possessing ferromagnetic features have revealed several anomalies in their magnetic properties. For instance, the room temperature Mössbauer spectrum of amorphous $20ZnO \cdot 30Bi_2O_3 \cdot 50Fe_2O_3$ does not show hyperfine structure although the Curie temperature of this material is 450 K.[28] For the amorphous $15CaO \cdot 25Bi_2O_3 \cdot 60Fe_2O_3$, the magnetization vs. temperature curve exhibits a maximum when the zero field cooling is applied and the maximum disappears when the static low field is applied during the cooling.[25] These phenomena imply that the ferromagnetic interaction does not propagate in a long range but is restricted to a short range even below the Curie temperature, and the freezing of the spins takes place in the mictomagnetic fashion. In the present section, Mössbauer measurements were carried out on amorphous $CaO-Bi_2O_3-Fe_2O_3$ system and an attempt was made to interpret the results obtained on the basis of the mictomagnetism.

Reagent grade $CaCO_3$, Bi_2O_3 and Fe_2O_3 were mixed thoroughly so as to make the composition of $xCaO \cdot (40-x)Bi_2O_3 \cdot 60Fe_2O_3$ where x was varied from 0 to 40 mol%. The mixture was pressed under

hydrostatic pressure of 10 MPa and then sintered in air at 750 to 800 °C for 5 h. The sintered body was melted in an image furnace with a Xe-lamp as the heat source and quenched by using a twin-roller rotating at 3000 rpm. The resultant specimen was a thin foil. It was ascertained by means of X-ray diffraction analysis with CuKα radiation that the specimen was amorphous.

The specimen was ground into powders and subjected to the Mössbauer measurements at room temperature. As the γ-ray source, 370 MBq ^{57}Co in metallic rhodium was used. The velocity calibration and the calculation of isomer shift and hyperfine field were performed by using a spectrum of α-Fe foil at room temperature.

The Mössbauer spectra of amorphous $10CaO \cdot 30Bi_2O_3 \cdot 60Fe_2O_3$, $15CaO \cdot 25Bi_2O_3 \cdot 60Fe_2O_3$ and $20CaO \cdot 20Bi_2O_3 \cdot 60Fe_2O_3$ are shown in Fig.3.8. Although it is known that these materials exhibit ferromagnetic character with Curie temperature around 730 K,[25] a major part of the spectra at room temperature mainly consists of a paramagnetic quadrupole doublet with slight absorption peaks split due to hyperfine field. This indicates that the magnetic order holds only within a short range and the system lies in the superparamagnetic state at room temperature. The hyperfine splitting is brought about by the clusters of larger size the magnetic anisotropy energy of which is large enough to overcome the thermal fluctuation at room temperature. Hence, the magnetism of this amorphous oxide system can be well explained by the model presented in Chapter 2. Namely, since the concentration of iron ions is almost the same in the present specimens, it is expected that the freezing temperature is high for the specimen

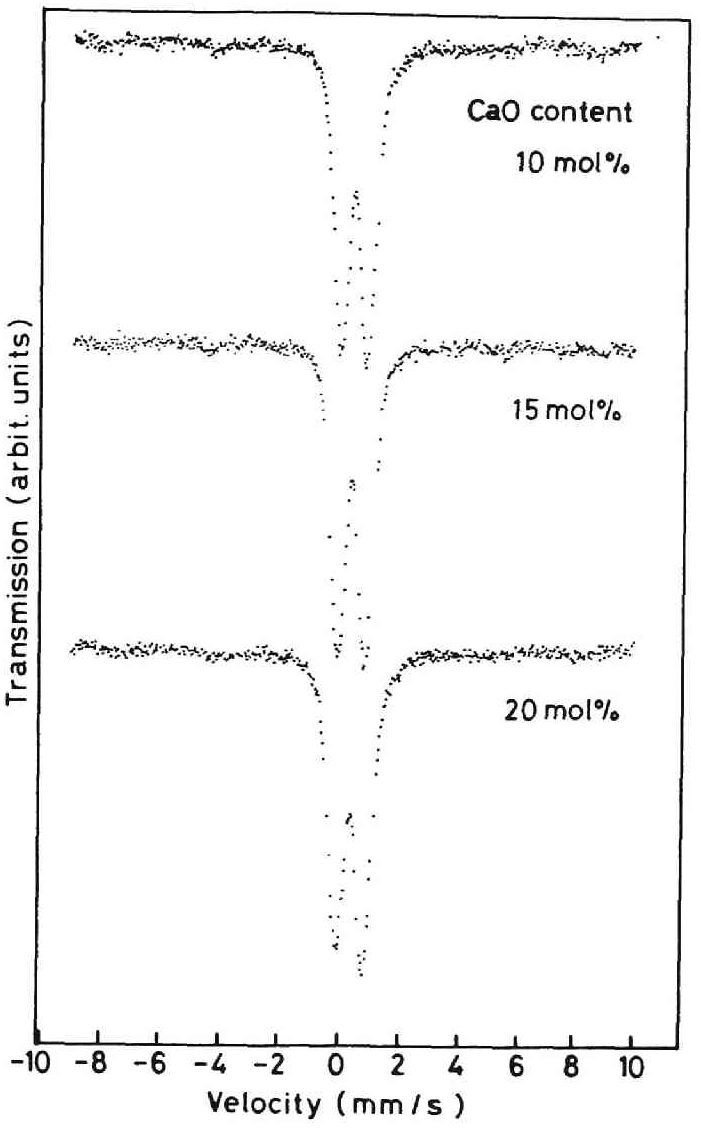

Fig.3.8 Mössbauer spectra of amorphous $10CaO \cdot 30Bi_2O_3 \cdot 60Fe_2O_3$, $15CaO \cdot 25Bi_2O_3 \cdot 60Fe_2O_3$ and $20CaO \cdot 20Bi_2O_3 \cdot 60Fe_2O_3$ at room temperature.

with the covalency of Fe-O bond being large.

The covalency of Fe-O bond can be estimated from the isomer shift of Mössbauer spectrum as described above. The isomer shift value along with the hyperfine field was elucidated by fitting the Lorentzian curves to the experimental spectrum. The compositional dependence of isomer shift obtained from this analysis is shown in Fig.3.9. In this composition region, the specimens with CaO content being 10, 15 and 20 mol% exhibit the hyperfine structure in the Mössbauer spectra at room temperature. Among these three specimens, the Fe-O bond in the specimens with 10 and 15 mol% CaO is more covalent than that in the specimen with 20 mol% CaO.

The values of the hyperfine field are listed in Table 3.2. It is seen that the hyperfine field of the specimen of 20 mol% CaO is somewhat smaller than that of the others. In this table, the fraction of the absorption area of four peaks due to hyperfine field in the total absorption area of the Mössbauer spectrum is also listed. This value is useful for the estimation of the fraction of spins within the clusters which are already frozen at room temperature. It is seen that the value for the specimen of 20 mol% CaO is smaller than that for the other specimens the same as the case of the hyperfine field. These facts clearly indicate that the freezing temperature lies around the room temperature for these specimens and the freezing temperature of the specimens with 10 and 15 mol% CaO is higher than that of the specimen with 20 mol% CaO. This tendency along with the compositional dependence of the covalency of Fe-O bond is coincident with the theoretical prediction mentioned in Chapter 2. A close look at Fig.

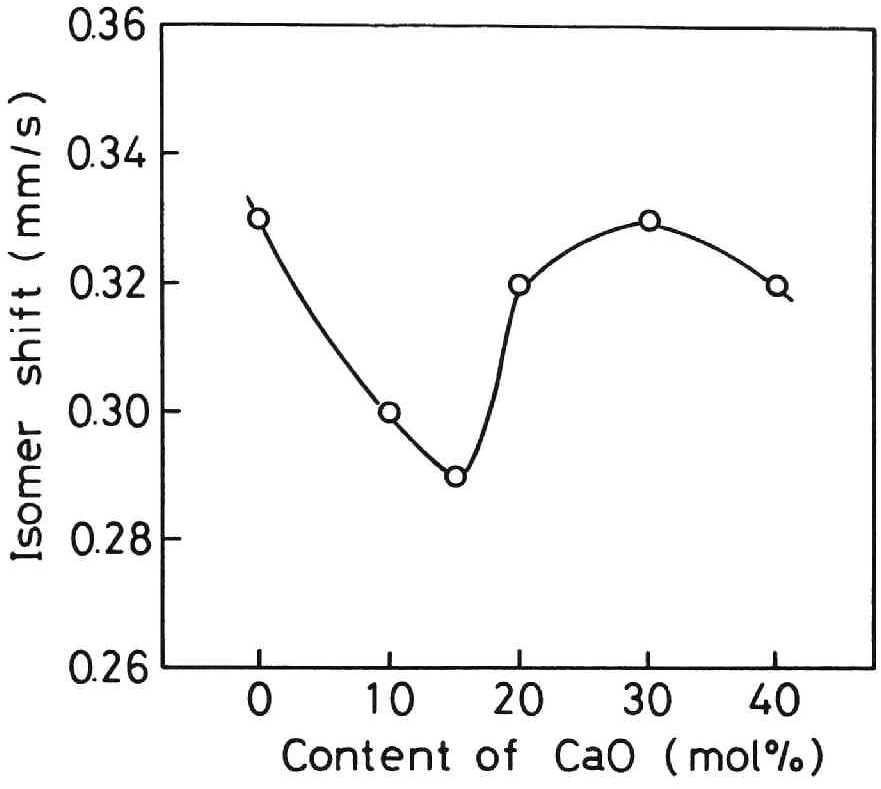

Fig.3.9 Variation of isomer shift with the content of CaO.

3.9 and Table 3.2 reveals that the freezing temperature of the specimens with 10 and 15 mol% CaO is almost identical with each other although the covalency of Fe-O bond is somewhat smaller in the specimen with 10 mol% CaO. It is expected that the anisotropy energy for Fe^{3+} ions is larger in the 10 mol% CaO specimen because this specimen contains larger amount of Bi^{3+} ions the 6p orbital of which has large spin-orbit coupling constant as discussed in Chapter 4. This effect increases the freezing temperature of the specimen with 10 mol% CaO.

Table 3.2 The hyperfine field and the fraction of absorption area of four peaks due to hyperfine structure for the specimens with the CaO content of 10, 15 and 20 mol%

Glass composition (mol%)	H_{hf}* (kOe)	A** (%)
$10CaO \cdot 30Bi_2O_3 \cdot 60Fe_2O_3$	506	7
$15CaO \cdot 25Bi_2O_3 \cdot 60Fe_2O_3$	510	7
$20CaO \cdot 20Bi_2O_3 \cdot 60Fe_2O_3$	474	5

*hyperfine field

**fraction of absorption area of four peaks due to hyperfine structure

Thus, the room temperature Mössbauer spectra of amorphous $10CaO \cdot 30Bi_2O_3 \cdot 60Fe_2O_3$, $15CaO \cdot 25Bi_2O_3 \cdot 60Fe_2O_3$ and $20CaO \cdot 20Bi_2O_3 \cdot 60Fe_2O_3$ have been interpreted well on the basis of the mictomagnetism. However, the reason why the magnetic interaction among the iron ions becomes ferromagnetic in this amorphous system remains still open. At present, the author considers that some ferrimagnetic microcrystal-like clusters exist in these matters.

3.5 Conclusions

From the result deduced in Chapter 2, it was expected that the difference in spin-freezing temperature among various oxide and fluoride glass systems was explainable in terms of the covalency of Fe-O and Fe-F bonds in these solids. The relationship between the spin-freezing temperature observed experimentally and the isomer shift obtained from the Mössbauer effect measurements described in the present chapter seems to support this expectation qualitatively.

It was also found that the present model is effective for description of the measuring frequency dependence of the spin-freezing temperature and the temperature dependence of the susceptibility. The Vogel-Fulcher law modified within the framework of the present model was well applied to explain the experimental data of measuring frequency dependence of the spin-freezing temperature for the oxide glasses. The value of intercluster interaction parameter T_0 obtained by analyzing the experimental data on the basis of the present model is physically meaningful. As for the temperature dependence of the susceptibility, two cases were expected in the superparamagnetic region which were derived from the qualitative discussion based on the present model. One of them is the case that the inverse susceptibility vs. temperature curve shows the upward curvature and the other is the case that the curve exhibits the downward curvature. The experimental curves for several oxide and fluoride glasses were in qualitative agreement with those derived from the present model.

The present model was also applied to clarify the magnetism

of amorphous oxides in the bismuth iron oxide-based system which show ferromagnetic character. The specimens with 10, 15 and 20 mol% CaO and 60 mol% Fe_2O_3 in the amorphous $CaO-Bi_2O_3-Fe_2O_3$ system exhibited slight peaks splitted due to hyperfine field at room temperature. The compositional dependence of hyperfine structure and isomer shift value was well explained in terms of the superparamagnetic model.

Reference

1) L.R.Walker, G.K.Wertheim and V.Jaccarino, Phys. Rev. Lett., **6**, 98 (1961)

2) J.Danon, Lectures on the Mössbauer Effect (Gordon & Breach, New York, 1968), p.92

3) Y.Syono, A.Ito and O.Horie, J. Phys. Soc. Jpn., **46**, 793 (1979)

4) O.Horie, Y.Syono, Y.Nakagawa, A.Ito, K.Okamura and S.Yajima, Solid State Commun., **25**, 423 (1978)

5) A.Bonnenfant, J.M.Friedt, M.Maurer and J.P.Sanchez, J. de Phys., **43**, 1475 (1982)

6) H.Laville and J.C.Bernier, J. Mat. Sci., **15**, 73 (1980)

7) S.K.Mendiratta, R.Horne and A.J. van Duyneveldt, Solid State Commun., **52**, 371 (1984)

8) J.P.Sanchez and J.M.Friedt, J. de Phys., **43**, 1707 (1982)

9) T.Egami, O.A.Sacli, A.W.Simpson, A.L.Terry and F.A.Wedgwood, J. Phys., C**5**, L261 (1972)

10) E.M.Gyorgy, K.Nassau, M.Eibschütz, J.V.Waszczak, C.A.Wang and J.C.Shelton, J. Appl. Phys., **50**, 2883 (1979)

11) A.M.Van Diepen and Th.J.A.Popma, Solid State Commun., **27**, 121 (1979)

12) J.P.Renard, J.P.Miranday and F.Varret, Solid State Commun., **35**, 41 (1980)

13) J.P.Renard, C.Dupas, E.Velu, C.Jacoboni, G.Fonteneau and J.Lucas, Physica, **108**B, 1291 (1981)

14) Y.Kawamoto, J.Fujiwara, K.Hirao and N.Soga, J. Non-Cryst. Solids, **95&96**, 921 (1987)

15) D.W.Moon, J.M.Aitken, R.K.MacCrone and G.S.Cieloszyk, Phys. Chem. Glasses, **16**, 91 (1975)

16) V.Cannella and J.A.Mydosh, Phys. Rev., **B26**, 4220 (1972)

17) M.K.Hou, M.B.Salamon and M.J.Pechan, J. Appl. Phys., **57**, 3482 (1985)

18) H.Vogel, Z. Phys., **22**, 645 (1921)

19) G.S.Fulcher, J. Am. Ceram. Soc., **8**, 339 (1925)

20) P.Beauvillain, C.Dupas, J.P.Renard and P.Veillet, J. Magn. Magn. Mat., **31-34**, 1377 (1983)

21) A.T.Meert and L.E.Wenger, J. Magn. Magn. Mat., **23**, 165 (1981)

22) J.P.Sanchez, J.M.Friedt, R.Horne and A.J. van Duyneveldt, J. Phys., C17, 127 (1984)

23) J.L.Tholence, Solid State Commun., **35**, 113 (1980)

24) N.Ota, M.Okubo, S.Masuda and K.Suzuki, J. Magn. Magn. Mat., **54-57**, 293 (1986)

25) M.Mitera, M.Mimura, N.Ota and S.Masuda, Research Reports of Masumoto Amorphous and Intercalation Compounds Project, 1986, p.10

26) S.Nakamura and N.Ichinose, J. Non-Cryst. Solids, **95&96**, 849 (1987)

27) K.Inomata, S.Hashimoto and S.Nakamura, Jpn. J. Appl. Phys., **27**, L883 (1988)

28) K.Suzuki, H.Onodera, M.Sakurai, S.Masuda, A.Matsumoto and H.Sadamura, IEEE Trans. Magnetics, **MAG-22**, 1090 (1986)

CHAPTER 4

LOCAL STRUCTURE OF IRON IN OXIDE GLASSES

It was shown in the previous chapter that the spin-freezing temperature of iron-containing amorphous oxides is intimately related to the local structure of iron in the solid, especially covalency of Fe-O bond and distribution of Fe-O-Fe bond angle. The former is directly related to the magnitude of superexchange interaction between iron ions and the latter to the distribution of the superexchange interaction. The valence state of iron ion also has an effect on the magnetic properties in a sense that Fe^{2+} ion has a large magnetic anisotropy due to the strong spin-orbit interaction of 3d orbital, while the magnetic anisotropy energy of Fe^{3+} ion is small because its orbital angular momentum is zero. Thus, the clarification of chemical state of iron in amorphous oxides is inevitable for the comprehension of magnetic properties of these materials. In the present chapter, the chemical state of iron in Fe_2O_3-based oxide glasses prepared by using a twin-roller quenching method is examined by means of magnetic spectroscopies, that is, ESR and Mössbauer measurements which are effective methods for such state analysis. In particular, the covalency of Fe-O bond in the oxide glasses, which is one of the most important factors that predominate the cluster spin glass-like transition of the oxide glass, is discussed in detail.

4.1 Covalency of Fe-O in Oxide Glasses

4.1.1 Binary System

In this section, an attempt was made to clarify the change in chemical state of iron ions with glass composition for Fe_2O_3-based binary oxide glasses by using ^{57}Fe Mössbauer spectroscopy. The glass systems studied were Fe_2O_3-P_2O_5, Fe_2O_3-TeO_2, Fe_2O_3-SrO, Fe_2O_3-BaO, Fe_2O_3-PbO and Fe_2O_3-Bi_2O_3, and the chemical state of iron ions examined were the valency of iron ions, the coordination number of O^{2-} ions around iron ions and the covalency of Fe-O chemical bonds. In particular, the covalency of Fe-O bond was systematically discussed on the basis of the concept of electronegativity.

The glasses were prepared by using reagent-grade Fe_2O_3, $FePO_4$ hydrate, TeO_2, $SrCO_3$, $BaCO_3$, PbO and Bi_2O_3 as starting materials. They were mixed in accordance with the glass compositions shown in Table 4.1. The mixtures were melted in an electric furnace or in an image furnace with a xenon lamp[1] at 900-2000 °C depending upon the glass compositions. For the Fe_2O_3-P_2O_5 system, $FePO_4$ hydrate was first kept at 400 °C for several hours so as to exclude water, and then mixed with Fe_2O_3. The melts were dropped on a twin-roller rotating at 3000 rpm and rapidly quenched. The details of the method of preparation and the glass-forming region for the Fe_2O_3-P_2O_5 and BaO-Fe_2O_3 systems will be described in Chapter 6.

The specimens thus obtained were thin foils of about 20 μm thickness. It was ascertained that the specimens were amorphous by means of X-ray diffraction analysis. The Mössbauer effect

Table 4.1 Mössbauer parameters for Fe_2O_3-based glasses

Composition mol%			IS mm/s	QS mm/s	Composition mol%		IS mm/s	QS mm/s
Fe_2O_3-P_2O_5					Fe_2O_3-Bi_2O_3			
50	50	Fe^{3+}	0.46	0.89	40	60	0.32	0.78
		Fe^{2+}	1.21	2.38	50	50	0.29	0.82
60	40	Fe^{3+}	0.47	1.01	60	40	0.33	0.78
		Fe^{2+}	1.14	2.35				
70	30	Fe^{3+}	0.43	1.18	Fe_2O_3-PbO			
		Fe^{2+}	1.06	2.45	15	85	0.22	0.81
					20	80	0.23	0.74
Fe_2O_3-TeO_2					30	70	0.25	0.84
10	90		0.39	0.70				
20	80		0.38	0.75	Fe_2O_3-SrO			
					50	50	0.23	0.99
Fe_2O_3-Bi_2O_3					55	45	0.24	0.97
10	90		0.25	0.65	60	40	0.25	0.93
20	80		0.28	0.77				
30	70		0.31	0.80	Fe_2O_3-BaO			
					40	60	0.22	0.81

measurements were carried out at room temperature. As the γ-ray source, a 370 MBq ^{57}Co in metallic rhodium was used. The velocity calibration and the calculation of the isomer shift were made by using the six hyperfine spectral lines of pure α-Fe foil as reference.

The glass compositions studied and the Mössbauer parameters obtained, that is, the isomer shift and the quadrupole splitting, were listed in Table 4.1. P_2O_5 is well known as a glass network forming oxide and TeO_2 can be made amorphous by the splat quenching.[2] Fe^{2+} ions were detected in all the Fe_2O_3-P_2O_5 glasses

but not in any of the Fe_2O_3-TeO_2 glasses. The values of isomer shift for Fe^{3+} ions were in the range of 0.38-0.47 mm/s, indicating that Fe^{3+} ions occupy the octahedral sites surrounded by O^{2-} ions in all the glasses.[3)]

On the other hand, the values of isomer shift for Fe^{3+} ion in the other glasses existed between 0.22 mm/s and 0.33 mm/s. This fact indicates that Fe^{3+} ions are laid on the tetrahedral sites. Fe^{2+} ions were not found in any of these glasses. Table 4.1 also shows a tendency that the value of isomer shift for both Fe^{3+} and Fe^{2+} ions decreased with increasing Fe_2O_3 content in Fe_2O_3-P_2O_5 and Fe_2O_3-TeO_2 glasses. To the contrary, the isomer shift increased with increasing Fe_2O_3 in other glasses.

According to Pauling,[4)] the ionic character of chemical bond f_I is empirically represented as follows:

$$f_I = 1 - \exp(-\frac{1}{4}\Delta\chi^2), \qquad (4.1)$$

where $\Delta\chi$ means the difference in electronegativity between two bonding atoms. Although a physical meaning of this equation is poor, it has been used effectively to discuss the nature of chemical bond qualitatively. The values of f_I for P-O and Te-O bonds were 0.40 and 0.43, respectively. The values of electronegativity proposed by Allred and Rochow[5)-7)] were used in calculation. The ionic characters of P-O and Te-O are relatively small, indicating that the valence electrons of O are spent mostly on the formation of P-O and Te-O covalent bonds and consequently contribute little to the 4s orbitals of Fe, when P or Te coexists with Fe. As a result, Fe-O bond becomes highly ionic and the Fe^{3+} ion takes six oxygen ions nearby. On the other

hand, the values of f_I for Sr-O and Ba-O were 0.79 and 0.80, respectively, indicating that ionic bond mainly governs these chemical bonds. The values of f_I for Pb-O, Bi-O and Fe-O, which were 0.61, 0.57 and 0.58, respectively, are intermediate. Hence, for example, in the Sr-O-Fe chemical bond where the electronegativities of Sr, O and Fe are 0.99, 3.50 and 1.64, respectively, the Fe-O bond is more covalent than the Sr-O bond, so that the formation of sp^3 or sd^3 hybrid orbitals becomes easier, leading to the four-coordinated Fe^{3+} ion state. This interpretation is in accordance with the principle of electronegativity equalization which was originally proposed by Sanderson[8] and thereafter developed theoretically by Ferreira,[9),10)] Iczkowski and Margrave,[11)] Politzer and Weinstein,[12)] and Donnelly and Parr.[13)] Within the framework of the principle of electronegativity equalization, the electronegativity is defined as follows:[11)-13)]

$$\chi = -\mu, \tag{4.2}$$

where μ is chemical potential of atom. The appropriateness of Eq.(4.2) can be shown as follows. The energy of atom as a function of valence state is experimentally represented by the next equation:[11)]

$$E(N) = aN + bN^2, \tag{4.3}$$

where N denotes the number of electrons present around the nucleus minus the atomic number, and a and b are constants peculiar to the atom. The ionization potential I and the electron affinity A of the atom can be derived from Eq.(4.3). The results are as follows:

$$I = E(-1)-E(0) = -a+b \tag{4.4}$$

$$-A = E(1)-E(0) = a+b. \tag{4.5}$$

From Eqs.(4.2), (4.4) and (4.5), the next relation is derived:

$$\chi \quad (I + A)/2. \tag{4.6}$$

This relation is just the same as the definition of electronegativity by Mulliken.[14]

The principle of electronegativity equalization is proved on the basis of Eq.(4.2) by following Politzer and Weinstein.[12] A molecule containing atoms the number of which is m is considered. The total energy of the molecule E is a function of the number of electrons associated with ith atom n_i and the internuclear distance r_j. Then,

$$dE = \sum_i (\partial E/ \partial n_i)_{r_j} dn_i + \sum_j (\partial E/ \partial r_j)_{n_i} dr_j \tag{4.7}$$

holds. When the molecule is in an equilibrium state, dE=0 and r_j is equal to the equilibrium internuclear separation r_e. Hence,

$$\sum_i (\partial E/ \partial n_i)_{r_e} dn_i = 0. \tag{4.8}$$

Since for the total number of electrons in the molecule n,

$$dn = 0 = \sum_i dn_i, \tag{4.9}$$

for $n_k (1 \leq k \leq m)$,

$$dn_k = - \sum_{i \neq k} dn_i. \tag{4.10}$$

Substituting Eq.(4.10) into Eq.(4.8) yields the next equation:

$$\sum_{l \neq k} [(\partial E/ \partial n_l)_{r_e, n_i, i \neq l} - (\partial E/ \partial n_k)_{r_e, n_i, i \neq k}] dn_l = 0. \tag{4.11}$$

Since dn_l can vary independently,

$$(\partial E/ \partial n_k)_{r_e, n_i, i \neq k} \quad (\partial E/ \partial n_l)_{r_e, n_i, i \neq l}. \tag{4.12}$$

From Eqs.(4.2) and (4.12),

$$\chi_k = \chi_l \qquad (4.13)$$

is derived. Eq.(4.13) clearly indicates that the electronegativities of each atom in the molecule are identical at equilibrium, which is invoked in the principle of electronegativity equalization.

The covalency of Fe-O chemical bond can be estimated by calculating the 4s electron contribution to this bond based on

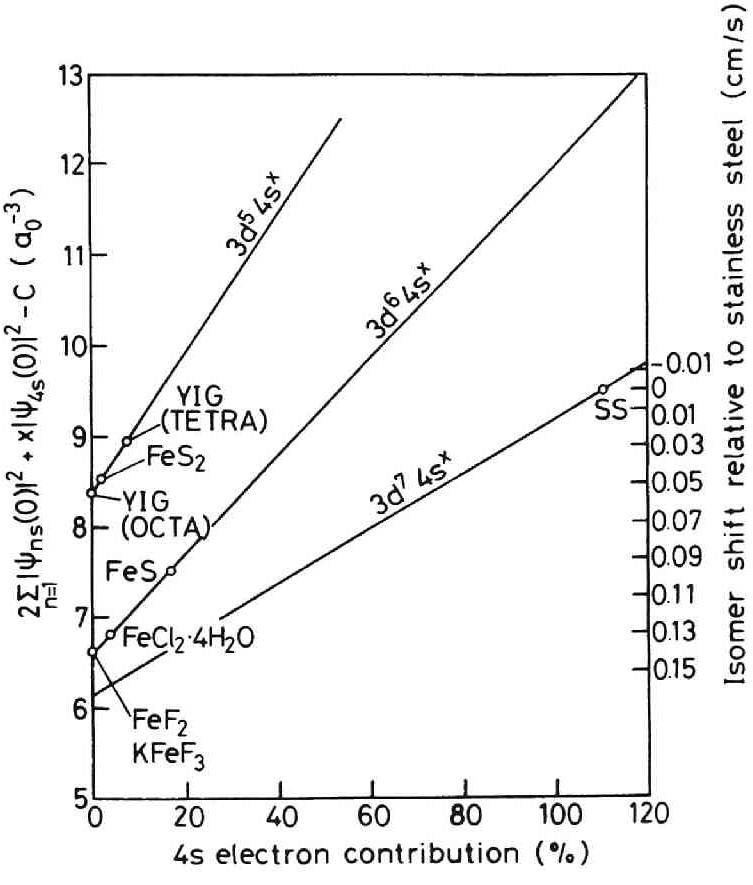

Fig.4.1 The relation between the isomer shift and the 4s electron contribution proposed by Walker et al.[15)]

the experimental data of isomer shift. Walker et al.[15] theoretically calculated the relation between the total s electron density at the nucleus for iron ion and the 4s electron contribution and compared with the experimental values of isomer shift. The relation between the isomer shift and the 4s electron contribution they proposed is shown in Fig.4.1. This chart was applied to estimate the 4s electron contribution of iron ions in

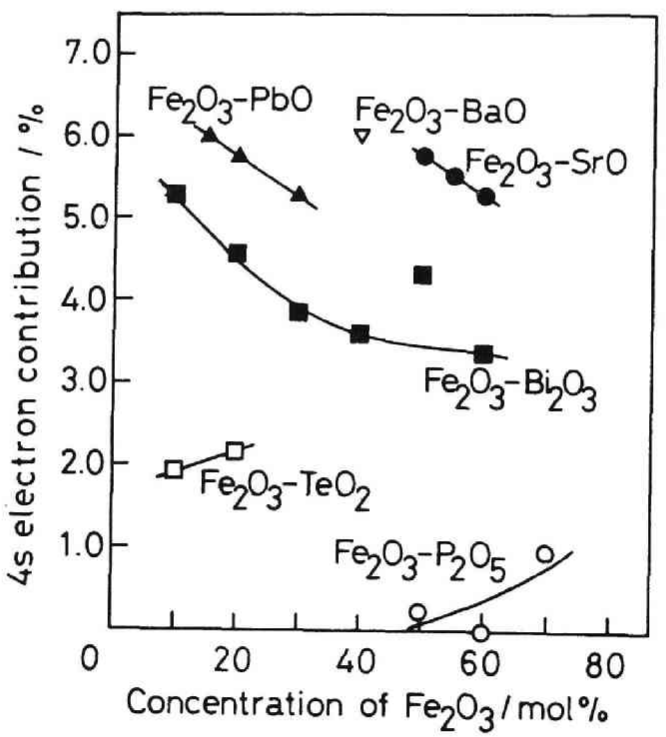

Fig.4.2 Change on 4s electron contribution for Fe^{3+} in Fe_2O_3-P_2O_5, -TeO_2, -SrO, -BaO, -PbO and -Bi_2O_3 binary oxide glasses as a function of Fe_2O_3 content.

the present Fe_2O_3-based glasses. The results of the variation of the 4s electron contribution for Fe^{3+} and Fe^{2+} ions with Fe_2O_3 content are shown in Figs.4.2 and 4.3, respectively. It is clear from Fig.4.2 that the 4s electron contribution for Fe^{3+} ions in the Fe_2O_3-SrO, Fe_2O_3-PbO and Fe_2O_3-Bi_2O_3 glass systems is relatively large and decreases with increasing Fe_2O_3 content. As described above, this fact is attributable to the ionic character of Sr-O, Pb-O and Bi-O bonds. It is also clear that the 4s elec-

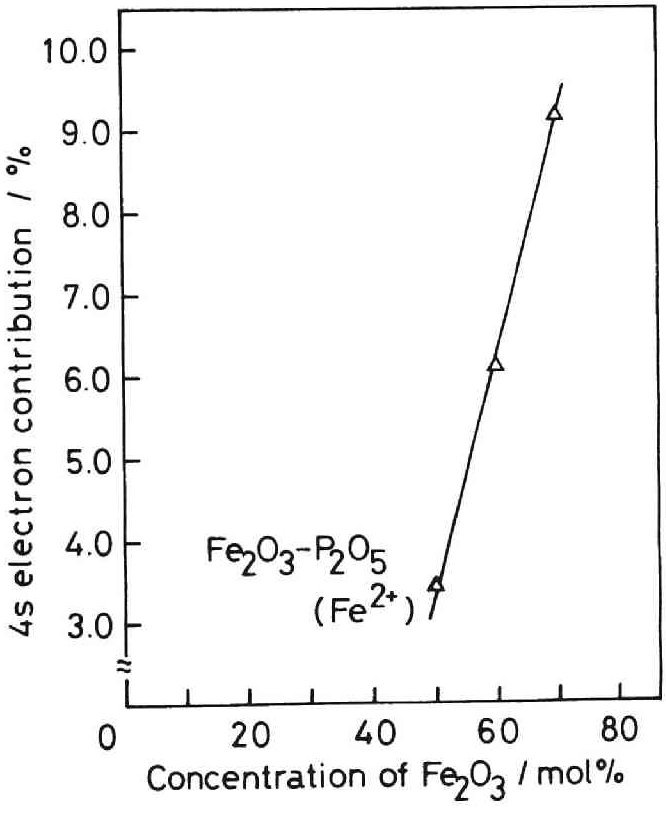

Fig.4.3 Change on 4s electron contribution for Fe^{2+} in Fe_2O_3-P_2O_5 glasses as a function of Fe_2O_3 content.

tron contribution for Fe^{3+} ions in the Fe_2O_3-P_2O_5 and Fe_2O_3-TeO_2 glass systems is small. This fact indicates that the Fe-O bond is highly ionic in those glasses, which is in accordance with the above-described electronegativity consideration. This situation is schematically shown for Ba-O-Fe and P-O-Fe bonds in Fig.4.4. In this figure, the solid and broken arrows represent the major and minor contributions of electrons, respectively.

In order to see the correlation more clearly, the 4s electron contribution was plotted as a function of the electronegativity in Fig.4.5. In this figure, the value of χ_g is defined as[8)]

$$\log\chi_g = \sum_i r_i \log\chi_i, \qquad (4.14)$$

where r_i stands for the ratio of ions in each glass, and shown in

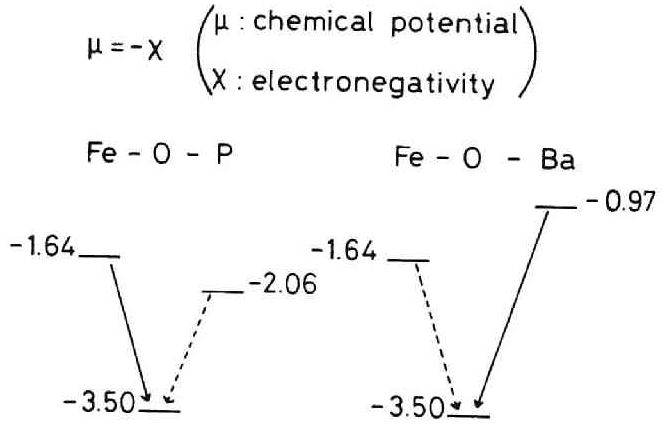

Fig.4.4 Schematic illustration of the principle of electronegativity equalization for the case of P-O-Fe and Ba-O-Fe bonds.

abscissa. The values of the 4s electron contribution for the Fe_2O_3-P_2O_5 glasses are the weighted average of Fe^{3+} and Fe^{2+} ions based on their existing ratio, which is assumed to be equal to the absorption area ratio of Fe^{3+} and Fe^{2+} ions in the Mössbauer spectra. The values used in the calculation are listed in Table 4.2. As seen from Fig.4.5, the 4s electron contribution decreases with increasing electronegativity. This tendency is

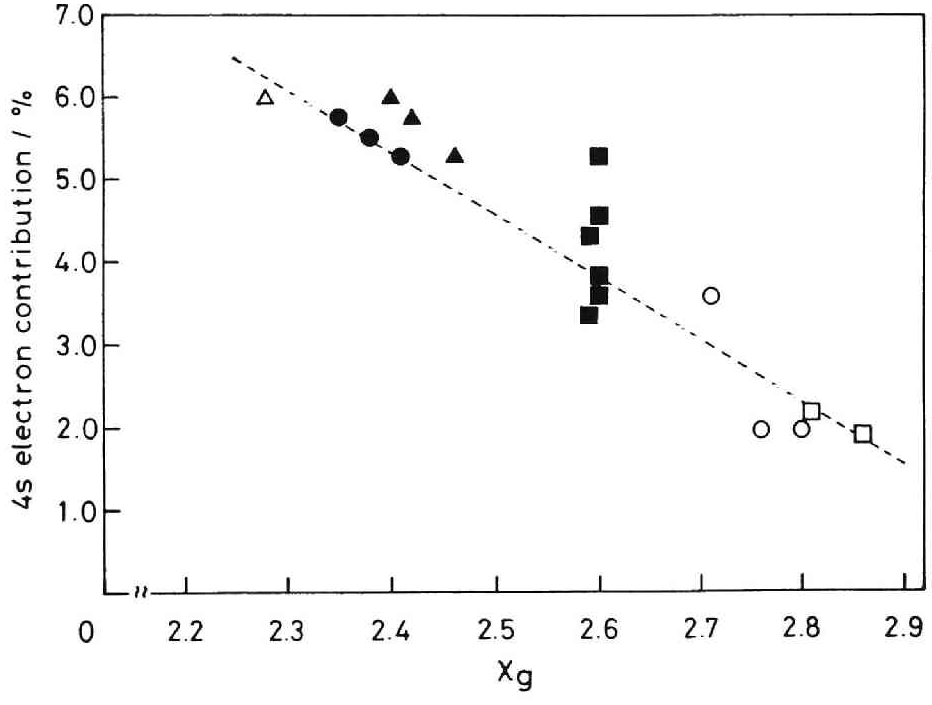

Fig.4.5 Relation between 4s electron contribution and the electronegativity χ_g for Fe_2O_3-based binary oxide glasses.
○: Fe_2O_3-P_2O_5, □: Fe_2O_3-TeO_2, ■: Fe_2O_3-Bi_2O_3
▲: Fe_2O_3-PbO, ●: Fe_2O_3-SrO, △: Fe_2O_3-BaO

Table 4.2 Absorption area ratio for Fe^{3+} and Fe^{2+} in Mössbauer spectra of Fe_2O_3-P_2O_5 glasses

Glass composition mol%		Fe^{3+}	Fe^{2+}
Fe_2O_3-P_2O_5			
50	50	0.46	0.54
60	40	0.68	0.32
70	30	0.68	0.32

compatible with the principle of electronegativity equalization. The Bi_2O_3-Fe_2O_3 system only deviates from this tendency. Namely, the 4s electron contribution increases with increasing the electronegativity as the content of Fe_2O_3 decreases for this system. This anomalous behavior of the Bi_2O_3-Fe_2O_3 system will be discussed in section 4.2.

4.1.2 Ternary System

In this section, the chemical state of iron in sodium borate glasses with a high content of iron oxide is examined as an example of the ternary system. In this system of sodium borate glasses, the borate anomaly related to the boron coordination change occurs. This phenomenon has been investigated by means of NMR measurements and MD calculation and it is now considered that the boron atoms coordinated by four oxygens increase with in-

creasing Na_2O content up to 33 mol%, beyond which they start to decrease.[16),17)] In this region of more than 33 mol% Na_2O, additional oxygens introduced by Na_2O are considered to play the role of nonbridging oxygens. According to infrared transmission spectroscopy, it is reasonable to consider that the coordination change of the boron atom continues up to 33 mol% Na_2O.[18)] Raman et al.[19)] have also studied the sodium borate glasses containing a small amount of Fe_2O_3 by Mössbauer spectroscopy and related the change of the isomer shift to the borate anomaly. In the present study, an attempt was made to clarify whether the same borate anomaly could be observed in the glasses containing a large amount of Fe_2O_3 and how the covalency of Fe^{3+}-O changed with composition.

The glasses were prepared by mixing reagent-grade Na_2CO_3, B_2O_3 and Fe_2O_3 in suitable proportions (Table 4.3) and melting the mixture at 1200-1300 °C for 1 h, with intermittent stirring. Then, the melts were rapidly quenched by a twin-roller and thin films of glass of about 20 μm thickness were obtained. No inclusion of the crystalline phase in the glasses obtained was ascertained by X-ray diffraction analysis. The Mössbauer measurements were carried out in the same condition as for the Fe_2O_3-based binary glasses.

The glass forming region is illustrated in Fig.4.6. This region determined by means of a twin-roller method, was quite wide when compared with that determined by the regular melt and quench method using a crucible.[20)] The compositional range was: Na_2O = 0-40 mol%, 60-80 mol%, Fe_2O_3 = 0-55 mol% and B_2O_3 = 10-100

Table 4.3 Mössbauer parameters of sodium iron borate glasses

Composition (mol%) Fe_2O_3	Na_2O	B_2O_3	Isomer shift (mm/s)	Quadrupole splitting (mm/s)
10	22.5	67.5	0.29	1.01
10	30	40	0.25	1.00
10	45	45	0.24	0.86
20	10	70	0.35	0.87
20	20	60	0.34	0.79
20	26.7	53.3	0.33	1.03
20	30	50	0.30	1.03
20	40	40	0.27	0.97
20	50	30	0.23	0.84
30	23.3	46.7	0.30	0.79
30	30	40	0.23	0.98
30	35	35	0.24	0.91
40	30	30	0.26	0.90

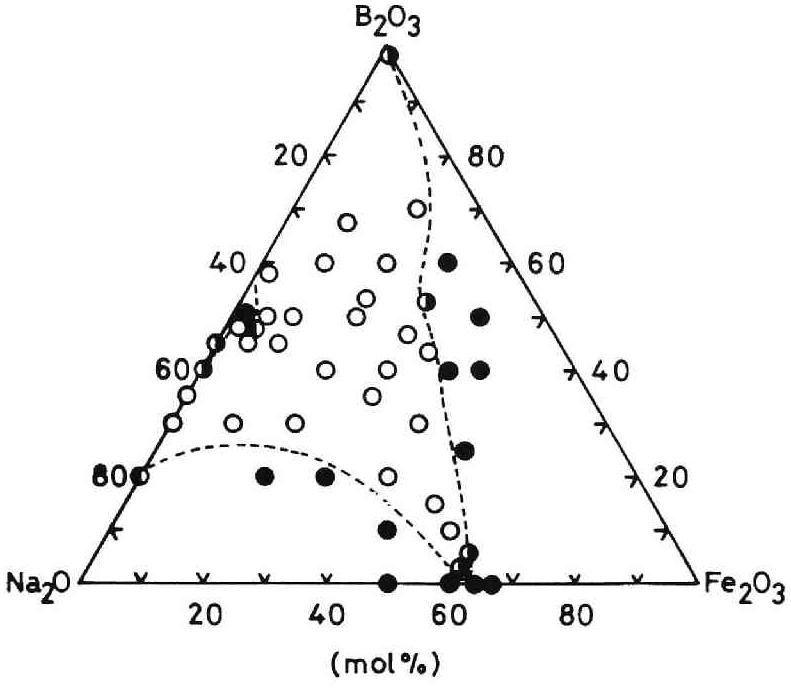

Fig.4.6 Glass forming region of sodium iron borate system (twin-roller method).
○: glass, ●: crystal, ◑, ◐: glass+crystal

mol%. Figure 4.7 shows a typical Mössbauer spectrum for $30Na_2O \cdot 40Fe_2O_3 \cdot 30B_2O_3$ glass. In a normal run, approximately $8X10^5$ counts were collected in each of 256 channels and the errors were obtained from the uncertainty in the peak positions which were of the order of one channel. All the specimens exhibited well-resolved quadrupole doublets in agreement with the results obtained by Burkley et al.[21] The Mössbauer parameters obtained for the glasses at room temperature are summarized in Table 4.3,

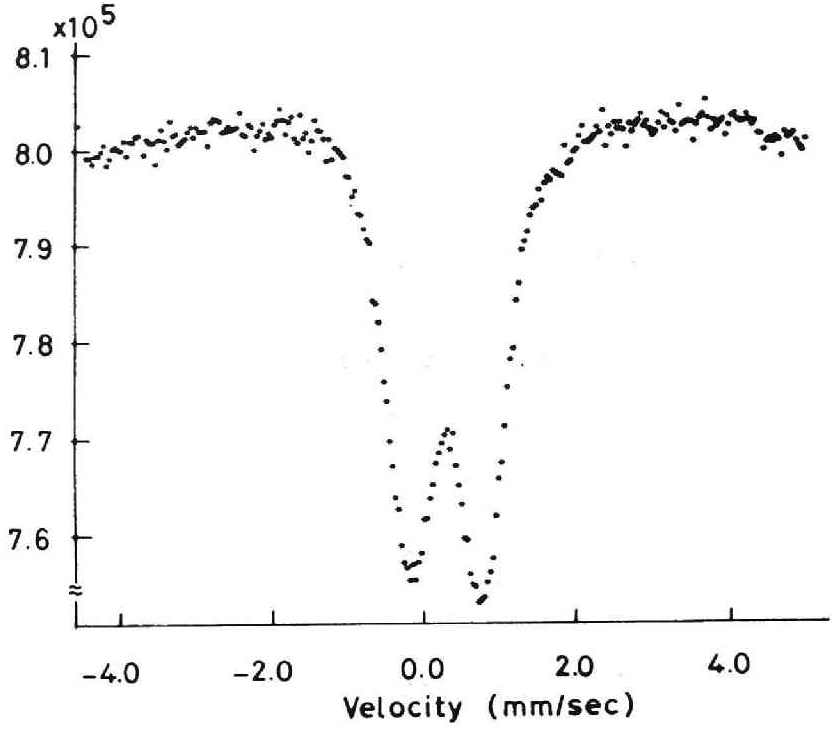

Fig.4.7 Mössbauer spectrum of $30Na_2O \cdot 40Fe_2O_3 \cdot 30B_2O_3$ glass.

which shows that over the entire compositional range the values of the isomer shift exist between 0.23 mm/s and 0.35 mm/s when referred to pure iron. This suggests that the iron ion exists mainly as an Fe^{3+} ion coordinated by four oxygen ions as indicated by Kurkjian and Sigety.[3)]

The variations of the isomer shift and the quadrupole splitting with the ratio of Na_2O to B_2O_3 at 20 mol% iron oxide are shown in Figs.4.8 and 4.9, respectively. From Fig.4.8, it is apparent that the isomer shift decreases with the increase of Na_2O concentration. A close look at this figure reveals that there is a sharp decrease of the isomer shift in the composition

of nearly 30 mol% Na_2O, and it tends to decrease further as the alkali concentration increases, thereby indicating that an increase in the s-electron density at the nucleus takes place. In these glasses, FeO_4 tetrahedra form a network structure with BO_3 triangles and BO_4 tetrahedra, and in the region of more than 30 mol% Na_2O content, an additional oxygen introduced by Na_2O breaks the bond in this network structure. As a result, the following structure appears;

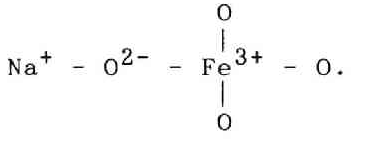

$$Na^{+} - O^{2-} - Fe^{3+} - O.$$

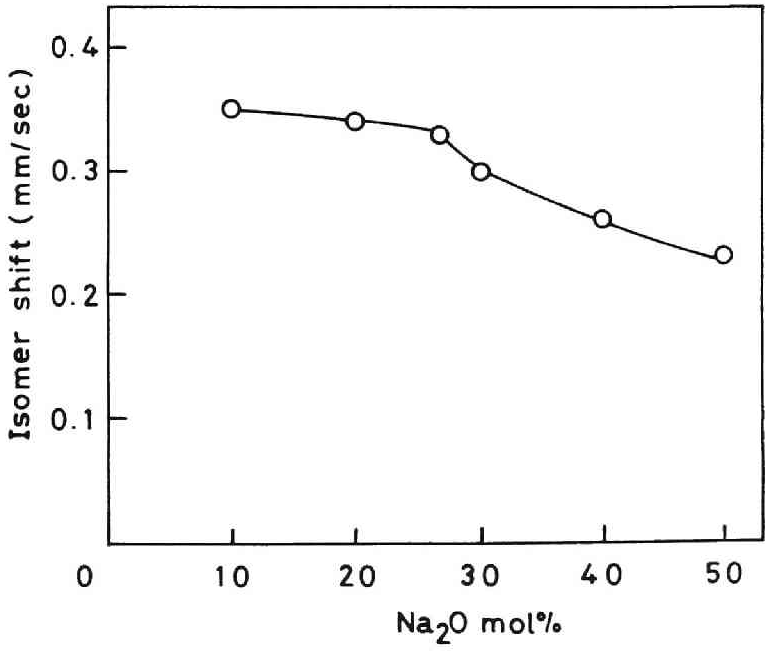

Fig.4.8 Variation of isomer shift with the Na_2O content

The oxygen bonded to a sodium ion attracts an outer electron of the sodium atom strongly because the ionic character of the Na-O chemical bond is large. This attracted electron contributes to the 4s orbital of Fe^{3+} by way of the 2p orbital of oxygen, leading to an increase of the s-electron density of Fe^{3+}. This should result in a sharp decrease of isomer shift. From this viewpoint, it is considered that when the alkali content is low, the oxygen introduced by Na_2O does not work as a nonbridging oxygen but takes the coordinating position of a boron atom as the fourth oxygen. Thus little change of the isomer shift in the region of less than 30 mol% Na_2O content should be observed. The result shown in Fig.4.8 seems to confirm this consideration. On

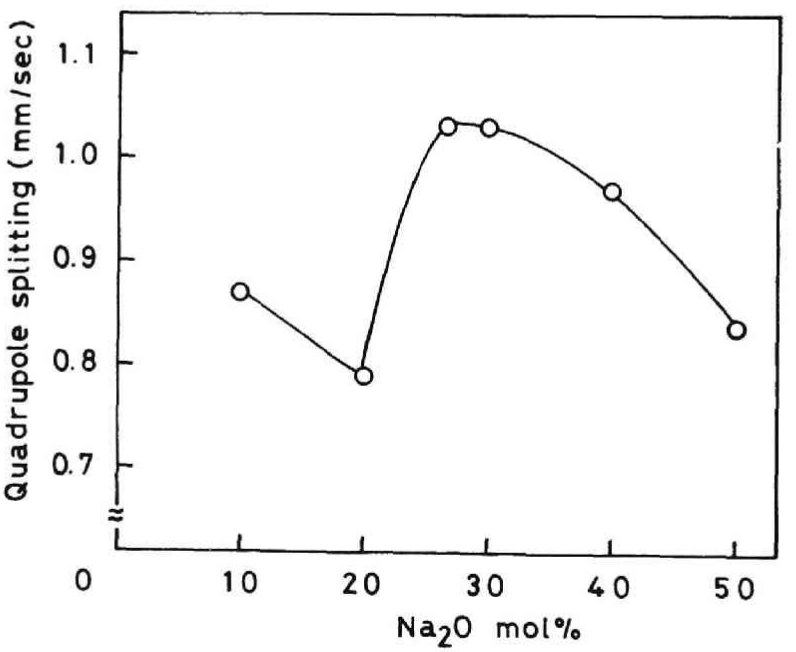

Fig.4.9 Variation of quadrupole splitting with the Na_2O content

the other hand, the sharp decrease of the isomer shift is observable in Fig.4.8 in the region of more than 30 mol% Na_2O, which fits the above consideration.

Similarly, the quadrupole splitting also changes significantly at about 30 mol% Na_2O content as shown in Fig.4.9. The quadrupole splitting tends to increase until Na_2O reaches nearly 30 mol%, and thereafter decreases as the alkali content increases. When the content of Na_2O exceeds 30 mol%, the glass structure is considered to become more flexible due to an increase of nonbridging oxygens and these oxygen ions coordinate the Fe^{3+} ion easier and more symmetrically. This structural change has an influence on the quadrupole splitting, since this value is a measure of the symmetry of the environment around the Fe^{3+} ion. In fact, the more the content of Na_2O increases, the smaller the quadrupole splitting becomes in the region of more than 30 mol% Na_2O content. On the other hand, in the region of less than 30 mol% Na_2O content, the additional Na_2O does not break down the network structure but coordinates the boron atom and may make the glass structure more rigid. As a result, the quadrupole splitting may tend to increase in this region.

The covalency of Fe^{3+}-O bond in the present glasses is also describable on the basis of the electronegativity consideration. Figure 4.10 shows the relation between the 4s electron contribution to the Fe^{3+} or Fe^{2+} ion and the electronegativity defined in Eq.(4.14) for Na_2O-Fe_2O_3-B_2O_3 glasses along with the Fe_2O_3-based binary system described in section 4.1.1. This figure also shows the values of amorphous Fe_2O_3,[22] Na_2O-Fe_2O_3,[23]

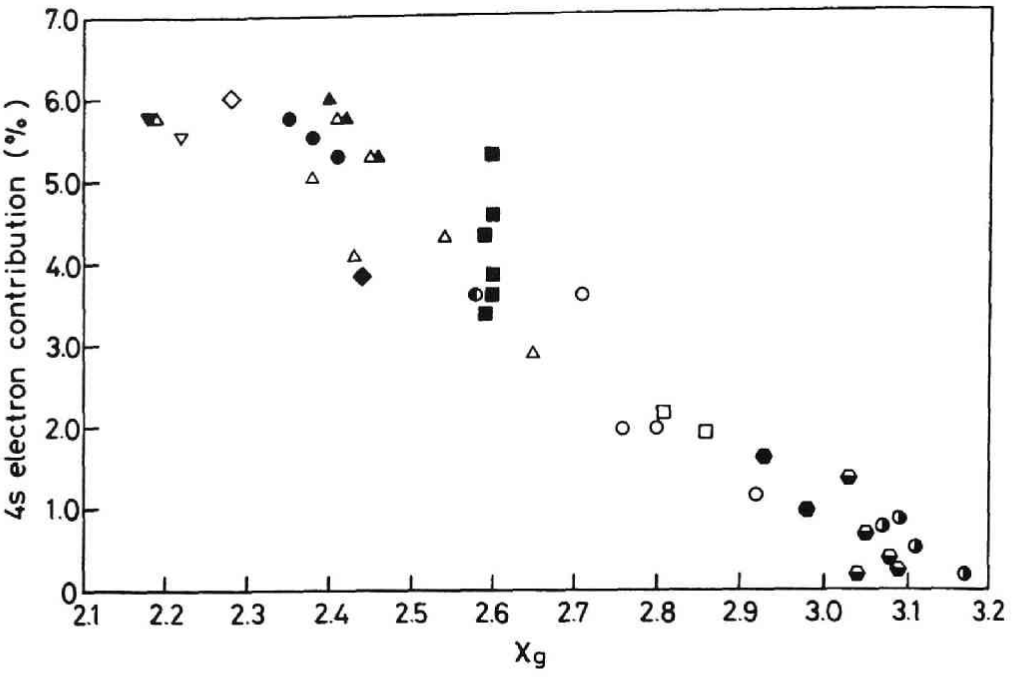

Fig.4.10 Relation between 4s electron contribution and the electronegativity χ_g for several oxide and fluoride glasses. ○:Fe_2O_3-P_2O_5, □:Fe_2O_3-TeO_2, ■:Fe_2O_3-Bi_2O_3, ▲:Fe_2O_3-PbO, ●:Fe_2O_3-SrO, ◇:Fe_2O_3-BaO, ◆:Fe_2O_3-Y_2O_3, ▽:Fe_2O_3-Na_2O, ▼:Fe_2O_3-K_2O, △:Fe_2O_3-Na_2O-B_2O_3, ◐:Fe_2O_3, ◑:FeF_3-PbF_2-MnF_2, ⬙:FeF_3-BaF_2-ZrF_4, ⬣:FeF_3-BaF_2-RF_2(R:Pb,Zn)

K_2O-Fe_2O_3,[23] Y_2O_3-Fe_2O_3,[24] PbF_2-MnF_2-FeF_3[25], BaF_2-ZrF_4-FeF_3,[26),27] and BaF_2-RF_2-FeF_3 (R:Pb,Zn).[27] For all of these systems, the trend that the 4s electron contribution decreases with increasing the electronegativity of the glass is observable. Thus, it is concluded that the covalency of Fe-O and Fe-F bond in the glasses is determined mainly by the electronegativity of the

constituent ions as expected from the principle of electronegativity equalization.

4.2 Ligand Field around Iron in Oxide Glasses

The symmetry of ligand field around iron is one of the important factors which determine the magnetic properties of iron-containing amorphous oxides because it is naturally expected that the more symmetric the geometrical configuration of the ligands becomes, the less the overlap of the orbitals between Fe^{3+} and the ligand becomes when the bond length of the Fe^{3+}-O is kept constant, leading to a decrease of the covalency of the Fe^{3+}-O bond. Among the Fe_2O_3-based glasses systematically studied in the previous section, the Bi_2O_3-Fe_2O_3 system is the most interesting because it has a wide glass-forming region and the two components of the basic system for the amorphous ZnO-Bi_2O_3-Fe_2O_3 and CaO-Bi_2O_3-Fe_2O_3 which show ferromagnetic character[28,29] as mentioned in the previous chapters. Furthermore, as described in section 4.1.1, the Bi_2O_3-Fe_2O_3 system does not follow the correlation between the 4s electron contribution and the electronegativity for amorphous iron oxides and fluorides. In the present section, a further examination was carried out by means of the ESR and Mössbauer measurements in order to obtain more detailed information about the local structure of iron ions in the binary Bi_2O_3-Fe_2O_3 glasses. In particular, the distribution of ligand field around iron ions and bonding characteristics of Fe-O bond were discussed.

Reagent-grade Bi_2O_3 and Fe_2O_3 were mixed in nominal compositions of $(100-x)Bi_2O_3 \cdot xFe_2O_3$ (x = 5-70 mol%) and melted in a platinum crucible with an electric furnace or in an image furnace with a xenon lamp at 1000 to 1500 °C in air. The melt was quenched by pouring onto a twin-roller made of stainless steel

rotating at 3000 rpm. The specimens thus obtained were subjected to X-ray diffraction using Cu Kα radiation in order to determine whether the specimen was amorphous or not.

The glass samples were then subjected to ESR and Mössbauer measurements. ESR measurements were carried out at room temperature using a Varian E-Line spectrometer operating at the X-band frequency (ν = 9.5 GHz) with a magnetic field modulation of 100 kHz. The magnetic modulation width and the time constant used were 8.0 G and 0.25 s, respectively. The Mössbauer effect measurements were performed at room and liquid nitrogen temperatures

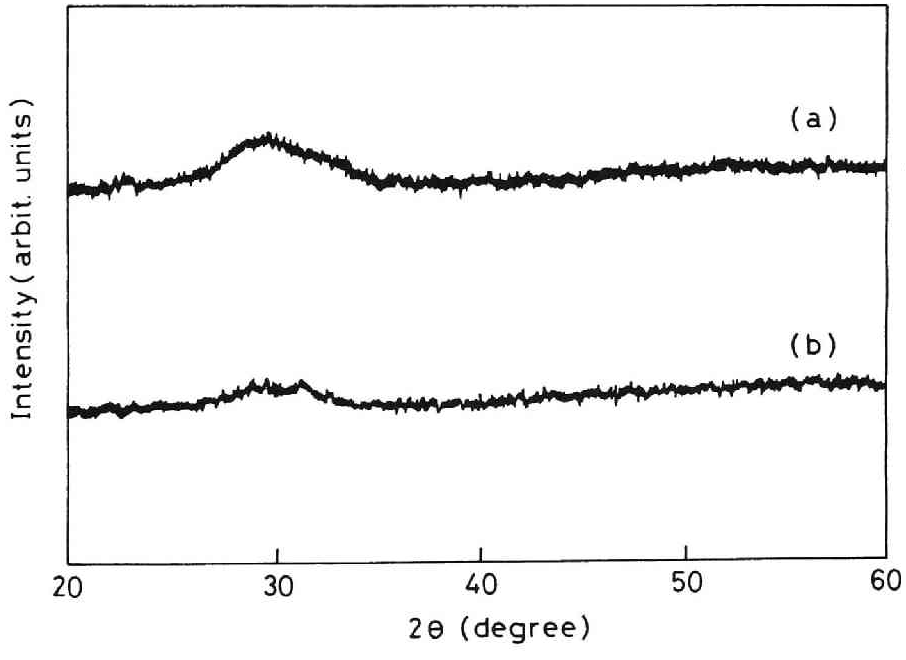

Fig.4.11 X-ray diffraction patterns of (a)$70Bi_2O_3 \cdot 30Fe_2O_3$ and (b)$40Bi_2O_3 \cdot 60Fe_2O_3$.

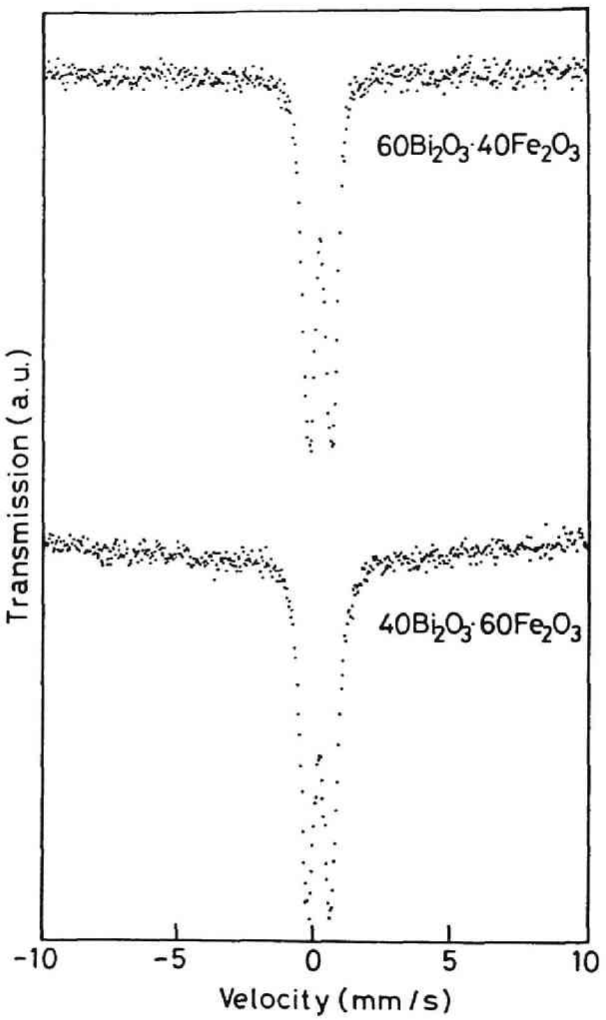

Fig.4.12 Mössbauer spectra of $60Bi_2O_3 \cdot 40Fe_2O_3$ and $40Bi_2O_3$ $60Fe_2O_3$ glasses at room temperature.

using a 370 MBq ^{57}Co in metallic rhodium as a γ-ray source. The velocity calibration and the calculation of isomer shift were made by using the spectrum of α-Fe foil obtained at room temperature.

X-ray diffraction patterns obtained for $70Bi_2O_3 \cdot 30Fe_2O_3$ and $40Bi_2O_3 \cdot 60Fe_2O_3$ are shown in Fig.4.11. Both patterns exhibit the characteristics of the amorphous state. The X-ray diffraction measurements indicated that the specimens with Fe_2O_3 content of 10 to 60 mol% were amorphous. This result is consistent with that reported by Ota et al.[26] Figure 4.12 shows the Mössbauer spectra of $60Bi_2O_3 \cdot 40Fe_2O_3$ and $40Bi_2O_3 \cdot 60Fe_2O_3$ glasses. The spectra consisted of one symmetric doublet which is attributable

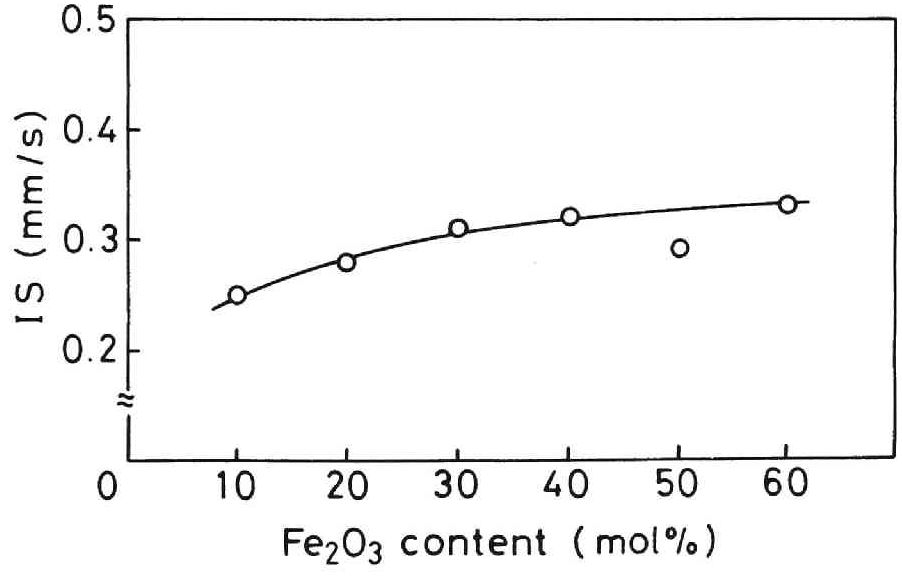

Fig.4.13 The variation of isomer shift with the content of Fe_2O_3.

to the absorption by Fe^{3+} at tetrahedral site, judging from its isomer shift.[30] The absorption peak due to Fe^{2+} was not observed. The spectra of the other glasses exhibited a similar appearance. The compositional dependence of the average value of the isomer shift obtained from the position of the doublet is shown in Fig.4.13. It is seen that the isomer shift tends to increase with increasing content of Fe_2O_3. This means that the covalency of the Fe^{3+}-O bond decreases as the content of iron ion increases.[15]

ESR spectra of $90Bi_2O_3$ $10Fe_2O_3$, $60Bi_2O_3 \cdot 40Fe_2O_3$ and $40Bi_2O_3 \cdot 60Fe_2O_3$ glasses are shown in Fig.4.14. The intensive spectral line centered at about g=2.0 is clearly seen for these three specimens. In addition, a weak signal at about g=4.3 is seen for only the glass with 10 mol% Fe_2O_3. According to the previous investigations,[31)-34)] for the oxide glass with the Fe_2O_3 content larger than about 3 mol%, the spectral lines centered at g=4.3 and g=2.0 are ascribed to isolated Fe^{3+} in the orthorhombic crystal field and Fe^{3+}-O-Fe^{3+} spin pair, respectively. Moon et al.[31] carried out ESR and magnetization measurements on $BaO \cdot 4B_2O_3$ glasses containing Fe_2O_3 and revealed that the decrease of the relative intensity of the signal at g=4.3 with increasing the content of Fe_2O_3 above 3 mol% corresponds to the formation of antiferromagnetic spin pairs between Fe^{3+} ions. The fact that the clusters of Fe^{3+} are present in the glass with low content (3-6 mol%) of Fe_2O_3 was also demonstrated for the Li_2O-Fe_2O_3-B_2O_3 glasses by means of Mössbauer measurements at 4.2 K.[35] It is likely that the same interpretation on the ESR spectra of the present Bi_2O_3-Fe_2O_3 glasses is reasonable and it

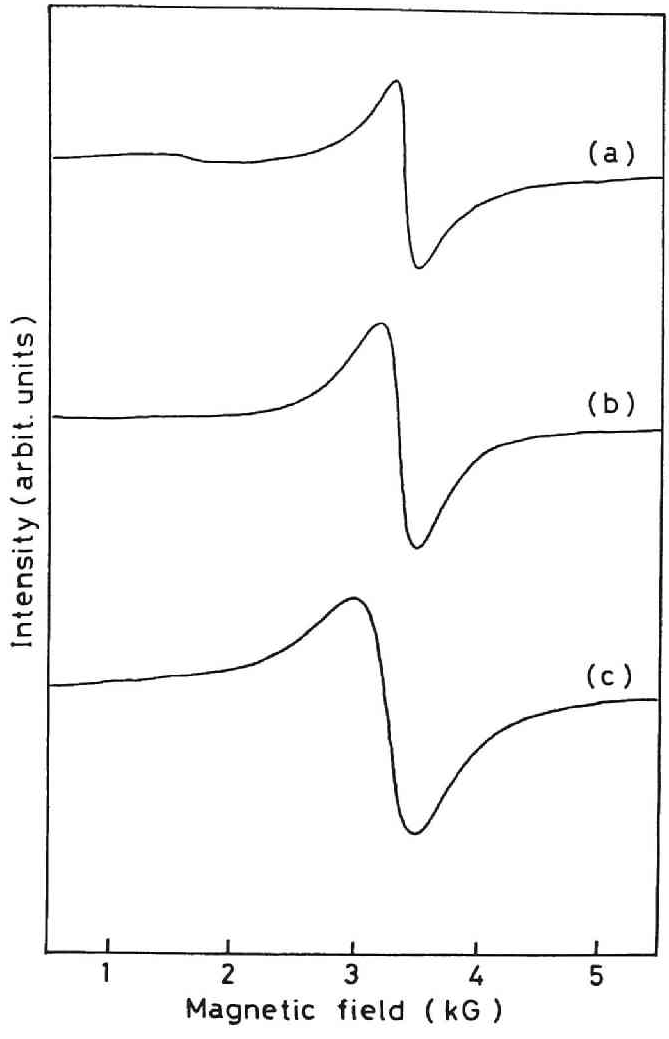

Fig.4.14 ESR spectra of (a)$90Bi_2O_3 \cdot 10Fe_2O_3$, (b)$60Bi_2O_3 \cdot 40Fe_2O_3$ and (c)$40Bi_2O_3 \cdot 60Fe_2O_3$ glasses at room temperature.

Table 4.4 Compositional dependence of the effective g-value

Composition (mol%) Bi_2O_3	Fe_2O_3	effective g-value
90	10	2.02
80	20	2.03
70	30	2.03
60	40	2.04
50	50	2.09
40	60	2.08

is concluded that for the present glasses almost all of the Fe^{3+} ions form spin pairs or clusters where dipolar and superexchange interactions between Fe^{3+} ions occur. The discussion on the clustering of Fe^{3+} ions is given in more detail in Chapter 5.

The compositional dependence of the effective g-value obtained from the ESR spectra is shown in Table 4.4. The effective g-value is larger than 2.00 for all of the glasses and the deviation from 2.00 increases monotonically with increasing content of iron ion. The value at 50 mol% Fe_2O_3 departs somewhat from such a tendency. A similar departure is also observed for the case of the isomer shift as seen from Fig.4.13. These facts may indicate that any structural change occurs at 50 mol% Fe_2O_3, although decisive evidence has not been obtained.

The deviation of the effective g-value from 2.00 is partly ascribable to the contribution of orbital angular momentum to

the magnetic moment of Fe^{3+}. According to Kittel[36] and Van Vleck,[37] the fraction of the magnetic moment due to the orbital angular momentum, $I_s(orb)$, to that due to spin angular momentum, $I_s(spin)$, is expressed as follows:

$$I_s(orb)/I_s(spin) = \frac{1}{2} g - 1, \qquad (4.15)$$

where g denotes the g-value obtained by the microwave magnetic resonance absorption experiments. The fact is explainable in terms of the effect of Bi^{3+} ions: contribution of the orbital angular momentum to the magnetic moment of Fe^{3+} is not absent in the present Bi_2O_3-Fe_2O_3 glasses in spite of the zero value of orbital angular momentum quantum number of a free Fe^{3+}. It is known that the spin-orbit interaction of the 6p orbital of Bi^{3+} is large, and this interaction has an influence on the electronic state of Fe^{3+} through the 2p orbital of O^{2-}. According to Shinagawa and Taniguchi,[38] the spin-orbit coupling constant of the 2p orbital of O^{2-} bonded to Bi^{3+}, ζ^*_{2p}, is expressed as follows:

$$\zeta^*_{2p} = \zeta_{2p} + S^2\zeta_{6p}, \qquad (4.16)$$

where ζ_{2p} and ζ_{6p} are the spin-orbit coupling constants of the 2p orbital of a free O^{2-} and that of the 6p orbital of Bi^{3+}, respectively, and S is the overlap integral between the 2p orbital of O^{2-} and the 6p orbital of Bi^{3+}. This equation indicates that the Bi^{3+} ion makes the spin-orbit interaction of the 2p orbital of O^{2-} bonded to Bi^{3+} ion larger. As a result, the 2p orbital of O^{2-} with a large spin-orbit coupling constant interacts with the 3d orbital of Fe^{3+} bonded to this O^{2-} ion, leading to the appearance of the orbital angular momentum which contributes to the magnetic moment of Fe^{3+}. The reason for the experi-

mental fact that the deviation from 2.00 increases with increasing the content of Fe_2O_3 is not clear at the present time. It may be due to an increase of strength of the dipolar interactions between Fe^{3+} ions. It is considered that the strong dipolar interaction, which is more predominant in the glass with a higher content of Fe_2O_3, causes a localized magnetic field at the site of Fe^{3+} and increases the effective g-value.[39]

In order to obtain further information about the local environment around iron ions, the distribution of the electric field gradient (EFG) was estimated from the Mössbauer spectra. According to Eibschütz et al.,[40] the spectral line is expressed by using the EFG distribution function, p(|V|), as follows:

$$f(z) = h \int_{-\infty}^{\infty} \frac{w^2 \, p(|V|)}{w^2 + 4(z-V)^2} dV, \qquad (4.17)$$

where w is the natural linewidth of the Mössbauer spectrum. p(|V|) is expressed as follows:[40]

$$p(V) \quad \begin{cases} \exp\{-[(V_M-V)/x_1V_M]^{y_1}\} & (0<V<V_M) \\ \exp\{-[(V-V_M)/x_2V_M]^{y_2}\} & (V_M<V<\infty) \end{cases}, \qquad (4.18)$$

where V_M is the EFG giving the peak of the distribution and x_1, x_2, y_1 and y_2 are positive parameters. The result of the parameter fitting for the $60Bi_2O_3 \cdot 40Fe_2O_3$ glass is shown in Fig.4.15, where the solid curve was calculated by using Eq.(4.17) on the basis of the distribution function shown in Fig.4.16. The agreement between the calculated curve and the experimental spectrum was very excellent. Similar results were also obtained for other glasses.

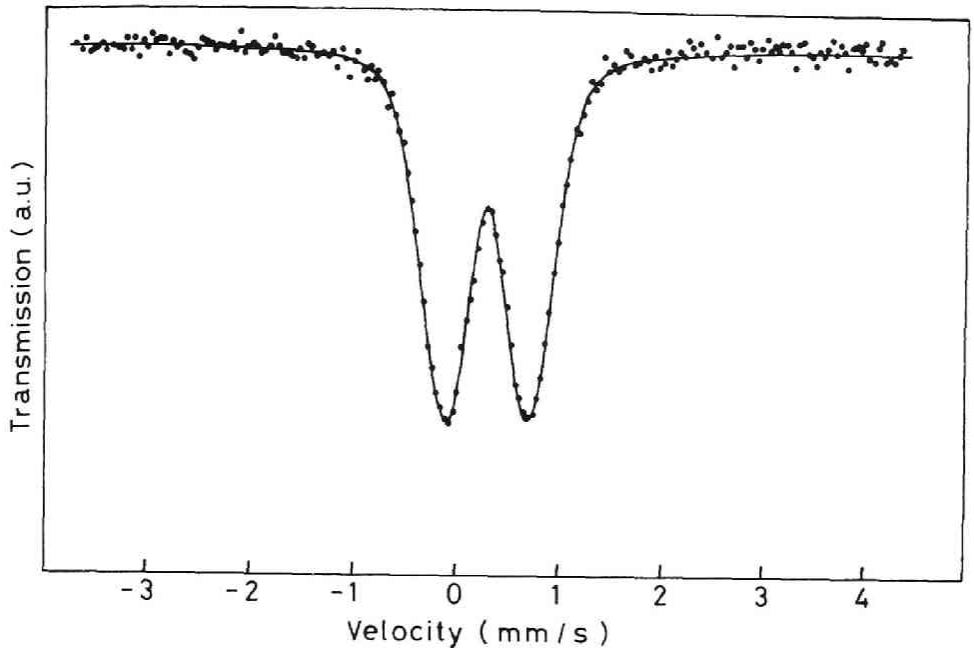

Fig.4.15 Mössbauer spectrum of $60Bi_2O_3 \cdot 40Fe_2O_3$ glass at room temperature. The solid curve is the spectrum simulated by considering the distribution of electric field gradient (see text).

The average value of EFG defined as

$$\overline{|V|} = \int_0^\infty |V| \cdot p(|V|)\, d|V| \qquad (4.19)$$

was evaluated from the distribution function for each glass and plotted against the content of Fe_2O_3 in Fig.4.17. In this figure, the value of $eQ\overline{|V|}$ where e is the elementary electric charge and Q is the quadrupole moment of ^{57}Fe nucleus is plotted as the ordinate. It is seen that the average EFG increases with

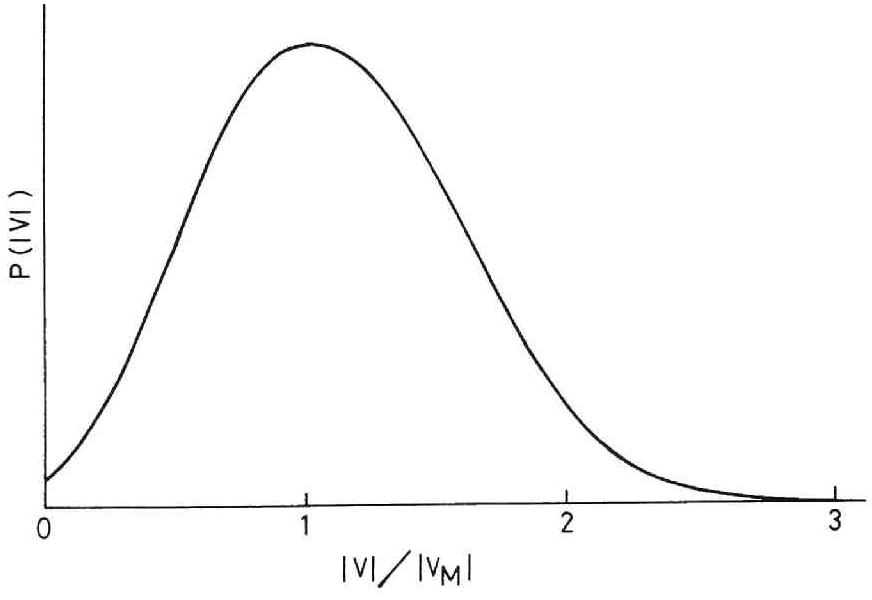

Fig.4.16 The distribution function of electric field gradient for $60Bi_2O_3 \cdot 40Fe_2O_3$ glass.

increasing content of Fe_2O_3, indicating that the FeO_4 tetrahedra become more asymmetric with an increase of Fe_2O_3. In such a glass, most of the Fe^{3+} ions take part in the constitution of the random network, which may lead to the asymmetry of FeO_4 tetrahedra. Since it is considered that the Fe^{3+} forms the d^3s or sp^3 hybrid orbital, this asymmetry leads to less overlap between the 4s orbital of Fe^{3+} and the 2p orbital of O^{2-}. Therefore, in the glass with higher content of Fe_2O_3 where the degree of asymmetry of FeO_4 is larger, the 4s electron density of Fe^{3+} is smaller. This inference is compatible with the compositional dependence of the isomer shift, that is the 4s electron density, mentioned above. Thus, the effect of asymmetry of FeO_4 pre-

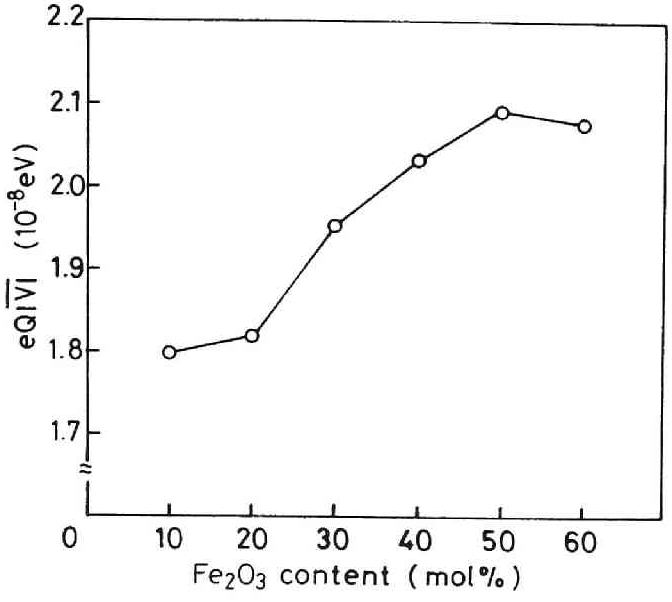

Fig.4.17 The variation of the average value of electric field gradient with the content of Fe_2O_3.

dominates over the covalency of Fe-O, leading to the deviation for the Bi_2O_3-Fe_2O_3 glasses from the correlation that the 4s electron density decreases with increasing the electronegativity described in section 4.1.1.

A slight decrease of the average EFG at the composition of 60 mol% Fe_2O_3 may be attributed to the precipitation of microcrystals in the $40Bi_2O_3 \cdot 60Fe_2O_3$ glass although they were not detected by X-ray diffraction analysis. It is inferred that the more symmetric configuration of O^{2-} around Fe^{3+} in the microcrystal makes the average EFG for the $40Bi_2O_3 \cdot 60Fe_2O_3$ glass smaller. The precipitation of microcrystals is demonstrated in

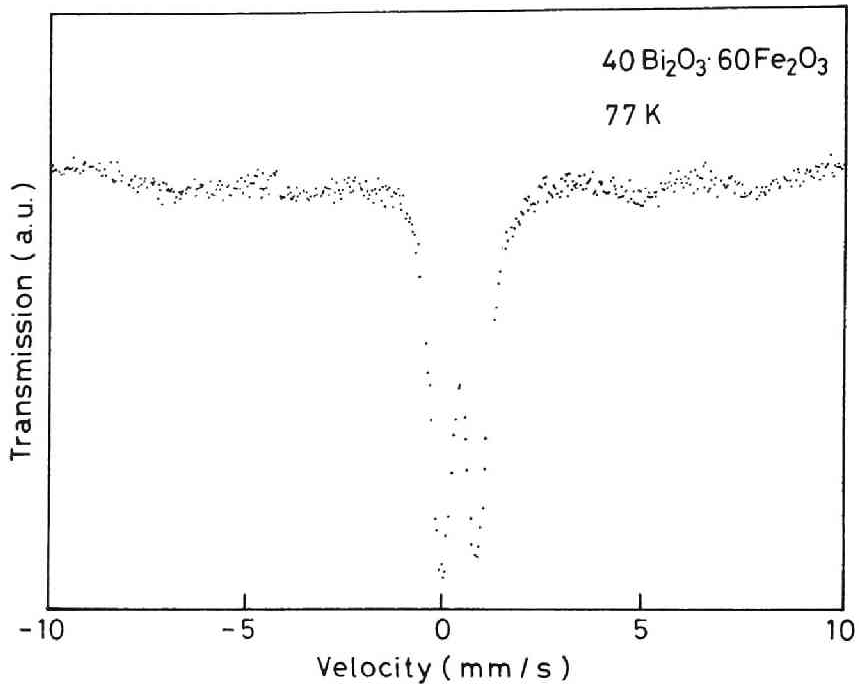

Fig.4.18 Mössbauer spectrum of $40Bi_2O_3 \cdot 60Fe_2O_3$ glass at 77 K.

the Mössbauer spectrum at 77 K as shown in Fig.4.18. The weak peaks, split due to the internal field, are clearly seen at about -7.0, -3.9, 4.9 and 7.8 mm/s in addition to the doublet in the central position. These additional peaks are ascribable to the ferri- or antiferromagnetic microcrystals having a magnetic transition temperature lower than room temperature or showing the superparamagnetism at room temperature, as in the case of $BiFeO_3$, α-Fe_2O_3 and $Bi_2Fe_4O_9$.

4.3 Conclusions

The valence state and coordination number of iron ions and the covalency of Fe-O bond were examined on several binary and ternary oxide glasses containing a large amount of Fe_2O_3 by means of ^{57}Fe Mössbauer spectroscopy. It was found that iron ions existed as Fe^{3+} ions in all the glasses except the Fe_2O_3-P_2O_5 glasses in which Fe^{2+} ions coexisted. It was considered that the coordination number of oxygen ions around Fe^{3+} ions was six in the Fe_2O_3-P_2O_5 and Fe_2O_3-TeO_2 glasses while Fe^{3+} ions in other glasses were coordinated by four oxygen ions. The covalency of the Fe-O bond was large in the Fe_2O_3-SrO, Fe_2O_3-BaO and Fe_2O_3-PbO glasses but very small in the Fe_2O_3-P_2O_5 and Fe_2O_3-TeO_2 glasses, showing that the chemical state of iron ion is greatly affected by other cations coexisting in glass. This fact was explained by considering the difference of electronegativity of the constituent cations.

In the Na_2O-Fe_2O_3-B_2O_3 system, sharp increase of the covalency of Fe^{3+}-O bond was detected at 30 mol% Na_2O content, corresponding to the borate anomaly. As for the binary Bi_2O_3-Fe_2O_3 system, Mössbauer measurements on the glasses with 10 to 60 mol% Fe_2O_3 revealed that the isomer shift of Fe^{3+} increases monotonically with increasing the concentration of Fe_2O_3. This fact indicates that the covalency of Fe^{3+}-O bond decreases as the concentration of iron ion increases. On the other hand, from the ESR measurements, it was found that the effective g-value is slightly larger than 2.00 for all of the glasses and the deviation from 2.00 increases with increasing the Fe_2O_3 content. The

deviation from 2.00 was attributed to the large spin-orbit coupling constant of 6p orbital of Bi^{3+} and the dipolar interactions between Fe^{3+} ions.

The distribution function of electric field gradient around Fe^{3+} in the present glasses was estimated by analyzing the Mössbauer spectra obtained experimentally. The average value of electric field gradient calculated using the distribution function increases with the content of Fe_2O_3. In other words, the FeO_4 tetrahedra are more asymmetric in the glass containing larger amount of Fe_2O_3. This compositional dependence of the average electric field gradient is compatible with that of the isomer shift.

References

1) H.Kozuka, R.Ota and N.Soga, Zairyo, **35**, 73 (1986)

2) P.T.Sarjeant and R.Roy, J. Am. Ceram. Soc., **50**, 500 (1967)

3) C.R.Kurkjian and E.A.Sigety, Phys. Chem. Glasses, **9**, 73 (1968)

4) L.Pauling, The Nature of Chemical Bond (Cornell University Press, New York, 1960) 3rd. ed., Chap.2

5) A.L.Allred and E.G.Rochow, J. Inorg. Nucl. Chem., **5**, 264 (1958)

6) A.L.Allred and E.G.Rochow, J. Inorg. Nucl. Chem., **5**, 269 (1958)

7) E.J.Little and M.M.Jones, J. Chem. Educ., **37**, 231 (1960)

8) R.T.Sanderson, Science, **121**, 207 (1955)

9) R.Ferreira, Trans. Faraday Soc., **59**, 1064 (1963)

10) R.Ferreira, Trans. Faraday Soc., **59**, 1075 (1963)

11) R.P.Iczkowski and J.L.Margrave, J. Am. Chem. Soc., **83**, 3547 (1961)

12) P.Politzer and H.Weinstein, J. Chem. Phys., **71**, 4218 (1979)

13) R.A.Donnelly and R.G.Parr, J. Chem. Phys., **69**, 4431 (1978)

14) R.S.Mulliken, J. Chem. Phys., **2**, 782 (1934)

15) L.R.Walker, G.K.Wertheim and V.Jaccarino, Phys. Rev. Lett., **6**, 98 (1961)

16) P.J.Bray and J.G.O'Keefe, Phys. Chem. Glasses, **4**, 37 (1963)

17) K.Hirao and N.Soga, J. Am. Ceram. Soc., **68**, 515 (1985)

18) J.Wong and C.A.Angell, Glass Structure by Spectroscopy (Dekker, New York, 1976), p.433

19) T.Raman, V.K.Nagesh, D.Chakravorty and G.N.Rao, J. Appl. Phys., **46**, 972 (1975)

20) H.Nasu, Ph. D Thesis, Kyoto Univ., (1983)

21) R.R.Burkrey, P.F.Kenealy, G.B.Beard and H.O.Hooper, J. Appl. Phys., **40**, 4289 (1969)

22) A.M. Van Diepen and Th.J.A. Popma, Solid State Commun., **27**, 121 (1978)

23) Y.Kuromitsu, K.Morinaga and T.Yanagase, Yogyo-Kyokai-Shi, **92**, 173 (1984)

24) E.M.Gyorgy, K.Nassau, M.Eibschütz, J.V.Waszczak, C.A.Wang and J.C.Shelton, J. Appl. Phys., **50**, 2883 (1979)

25) Y.Kawamoto, J.Fujiwara, K.Hirao and N.Soga, J. Non-Cryst. Solids, **95&96**, 921 (1987)

26) T.Nishida, T.Nonaka and Y.Takashima, Bull. Chem. Soc. Jpn., **58**, 2255 (1985)

27) Y.Kawamoto, I.Nohara, K.Hirao and N.Soga, Solid State Commun., **51**, 769 (1984)

28) N.Ota, M.Okubo, S.Masuda and K.Suzuki, J. Magn. Magn. Mat., **54-57**, 293 (1986)

29) S.Nakamura and N.Ichinose, J. Non-Cryst. Solids, **95&96**, 849 (1987)

30) C.R.Kurkjian, J. Non-Cryst. Solids, **3**, 157 (1970)

31) D.W.Moon, J.M.Aitken, R.K.MacCrone and G.S.Cieloszyk, Phys. Chem. Glasses, **16**, 91 (1975)

32) R.M.Catchings, Phys. Stat. Sol. (a)**39**, K101 (1977)

33) L.Trombetta, J.Williams and R.K.MacCrone, Amorphous Magnetism II, ed. by R.A.Levy and R.Hasegawa (Plenum Press, New York, 1977), p.643

34) R.G.Gupta, R.G.Mendiratta, S.S.Sekhon, R.Kamal, S.K.Suri and N.Ahmad, J. Non-Cryst. Solids, **33**, 121 (1979)

35) J.P.Sanchez and J.M.Friedt, J. de Phys., **43**, 1707 (1982)

36) C.Kittel, Phys. Rev., **76**, 743 (1946)

37) J.H.Van Vleck, Phys. Rev., **78**, 266 (1950)

38) K.Shinagawa and S.Taniguchi, Jpn. J. Appl. Phys., **13**, 1664 (1974)

39) T.Komatsu, N.Soga and M.Kunugi, J. Appl. Phys., **50**, 6469 (1979)

40) M.Eibschütz, M.E.Lines and K.Nassau, Phys. Rev., B**21**, 3767 (1980)

CHAPTER 5

IRON ION CLUSTER IN AMORPHOUS OXIDES

As discussed in Chapter 2, the behavior of cluster spin glass-like transition observed experimentally in oxide and fluoride glasses containing magnetic ions has been often explained in terms of superparamagnetic model by assuming the existence of concentrated regions of magnetic ions in the glass. The model firstly proposed by Verhelst et al.[1] to interpret the temperature dependence of susceptibility for cobalt and manganese aluminosilicate glasses as progressive freezing of superparamagnetic monodomains (in other words, cluster) has been utilized to explain the time dependence of remanent magnetization and the temperature dependence of ESR spectral shift of those glasses.[2),3)] Sanchez et al.[4)] performed ac susceptibility measurements on $FeO-Al_2O_3-SiO_2$ glasses and stated that the spin freezing process of the glasses is a relaxation phenomenon of clusters rather than a cooperative magnetic transition of the ensemble of spins. Renard et al.[5)] also confirmed the superparamagnetic region nearly above the spin freezing temperature for $PbMnFeF_7$ and Pb_2MnFeF_9 glasses by using the susceptibility and Mössbauer measurements. A similar result was reported for $50Fe_2O_3 \cdot 35BaO \cdot 15B_2O_3$ glass, whose temperature dependence of Mössbauer spectrum manifested the superparamagnetic transition of the magnetic clusters.[6)] Thus, it seems clear that there exist assemblage states of magnetic ions which determine the magnetic properties of the glass. It has been considered that such a clustering of magnetic ions in the high concentration region is ascribed to the phase separation

of the glass.[1),6)]

On the other hand, clustering or pairing of magnetic ions in low concentration region has been also observed. As for Fe^{3+} ions, their clustering in the low concentration region can be inferred from the variation of ESR spectrum. One of the examples is the early work done by Moon et al.[7)] They revealed with the aid of magnetic susceptibility measurements that in $BaO \cdot 4B_2O_3$ glass containing a small amount of Fe_2O_3, the relative change of ESR spectral lines centered at g=4.3 and g=2.0 was closely related to the clustering reaction of Fe^{3+} ions. Namely, a monotonous increase of the relative intensity of ESR signal at g=2.0 above 3 mol% Fe_2O_3 was attributed to the increase in number of Fe^{3+} ion clusters. Thereafter, this interpretation has been applied to the glasses in the $PbO-Fe_2O_3-B_2O_3$,[8)] $PbO-Fe_2O_3-SiO_2$,[9)] $CaO-Fe_2O_3-SiO_2$[10)] and other systems. However, the reason why the magnetic ions tend to form clusters even in the low concentration region is still unclear. Extensive information about the effects of melting temperature, cooling rate, heat treatment, glass composition, additives and preparation process on the clustering of magnetic ions is needed to solve this problem. As far as we know, however, little data are available except the study about the effect of titanium ion on the clustering of iron in borosilicate glasses reported by Trombetta et al.[11)]

Thus, in the present chapter, the effect of melting temperature on the clustering of iron ions in barium borate and lead borate glasses whose magnetic structure and properties were investigated most extensively[6-8,12-16)] was examined by means of

ESR measurements. The results obtained were discussed qualitatively from thermodynamical viewpoints. Besides, the variation of the state of clusters with glass composition in lithium borate glass system, in which the oxygen coordination number for boron ion is known to vary with alkali oxide content the same as the sodium borate glasses discussed in Chapter 4, was examined, and the effect of glass structure on the clustering of iron ion was discussed. Furthermore, the state of iron ion cluster in oxide glasses prepared from gels by using the sol-gel method was examined and compared with that in the melt-derived glasses.

5.1 Iron Ion Cluster in Oxide Glasses Derived from Melt

For barium borate and lead borate glasses, glass samples were prepared from the reagent-grade Fe_2O_3, $BaCO_3$, Pb_3O_4 and H_3BO_3 as starting materials. They were mixed so as to make $RO \cdot 2B_2O_3$ (R: Ba, Pb) glasses with various concentrations of Fe_2O_3 (1 to 10 mol%). The mixture was melted in a Pt-Rh crucible at 1250 °C for barium borate glass and 1150 °C for lead borate glass, respectively, for 1 h in air, and then remelted at various temperatures from 850 to 1250 °C for 1 h in air. The melt was then poured on an iron plate and quenched by being pressed rapidly with the other iron plate. For the lithium borate glasses, the ratio of Li_2O to B_2O_3 was varied with keeping the concentration of Fe_2O_3 to be 4 mol%. The mixture of the raw materials (Fe_2O_3, Li_2CO_3 and H_3BO_3) was melted at 1100 °C for 30 min in air. Then, the melt was made into glass by the same procedure used for the barium borate and lead borate glasses. It was ascertained by means of X-ray diffraction analysis with Co Kα radiation that the samples thus obtained were amorphous.

The glass samples were ground into powders, and a small amount of powder (about 100 mg) were placed in a silica tube and then subjected to ESR measurements. The ESR measurements were carried out at room temperature using Varian E-Line spectrometer operating at X-band frequency (ν - 9.5 GHz) with a magnetic field modulation of 100 kHz. The magnetic modulation width and the time constant used were 8.0 G and 0.25 s, respectively.

For barium borate and lead borate glasses, Mössbauer measurements were applied in order to obtain further information

about the local environment of iron ions, in particular the effect of melting temperature on the formation of Fe^{2+} ion in the glasses. The Mössbauer measurements were carried out at room temperature using the powder samples. As the γ-ray source, a 370 MBq ^{57}Co in metallic rhodium was used. The velocity calibration and the calculation of the isomer shift were made from the spectrum of α-Fe foil at room temperature.

The ESR spectra obtained for $BaO \cdot 2B_2O_3$ and $PbO \cdot 2B_2O_3$ glasses containing 1,5 and 10 mol% Fe_2O_3 are shown in Figs.5.1 and 5.2, respectively. These spectra are the ones for the glasses prepared by melting at 1150 °C. Two distinctive spectral lines at g=4.3 and g=2.0 appeared in all of the spectra. According to the previous studies,[17)-19)] the former is attributed to the isolated Fe^{3+} ion in the orthorhombic crystal field. Castner et al.[17)] successfully showed the effective g-value of 30/7 (≈4.3) by solving the eigenvalue problem for the next spin Hamiltonian:

$$\mathcal{H} = g\beta HS + D[S_z^2 - \frac{1}{3}S(S+1)] + E(S_x^2 - S_y^2) \qquad (5.1)$$

under the conditions that D=0, E≠0 and E>>$g\beta$H. Later, Wickman et al.[18)] revealed that E/D= $\frac{1}{3}$ and D>>$g\beta$H yield g=4.3 for Eq. (5.1) and demonstrated that the orthorhombic crystal field gives the signal at g=4.3. This interpretation was supported by the computation by Brodbeck.[19)]

On the other hand, the resonance signal at g=2.0 is attributable to the clustered Fe^{3+} ion.[7),20)] It was observed that the intensity of this signal at liquid helium temperature was much weaker than that at room temperature for a basalt glass.[20)] This

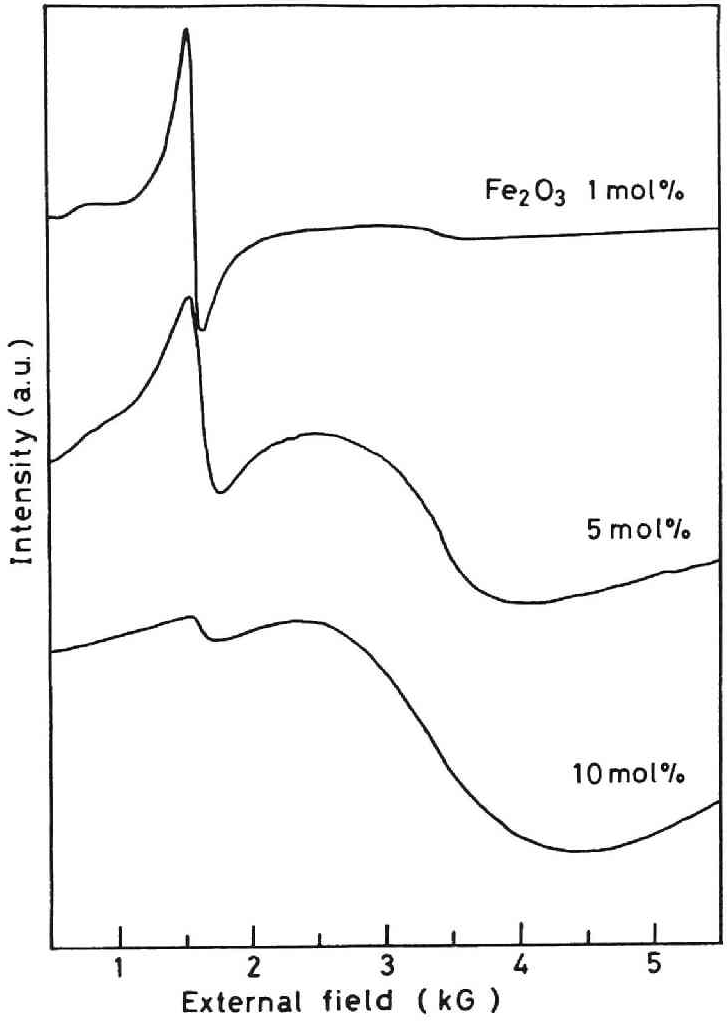

Fig.5.1 The variation of ESR spectrum with the content of Fe_2O_3 for $BaO \cdot 2B_2O_3$ glass.

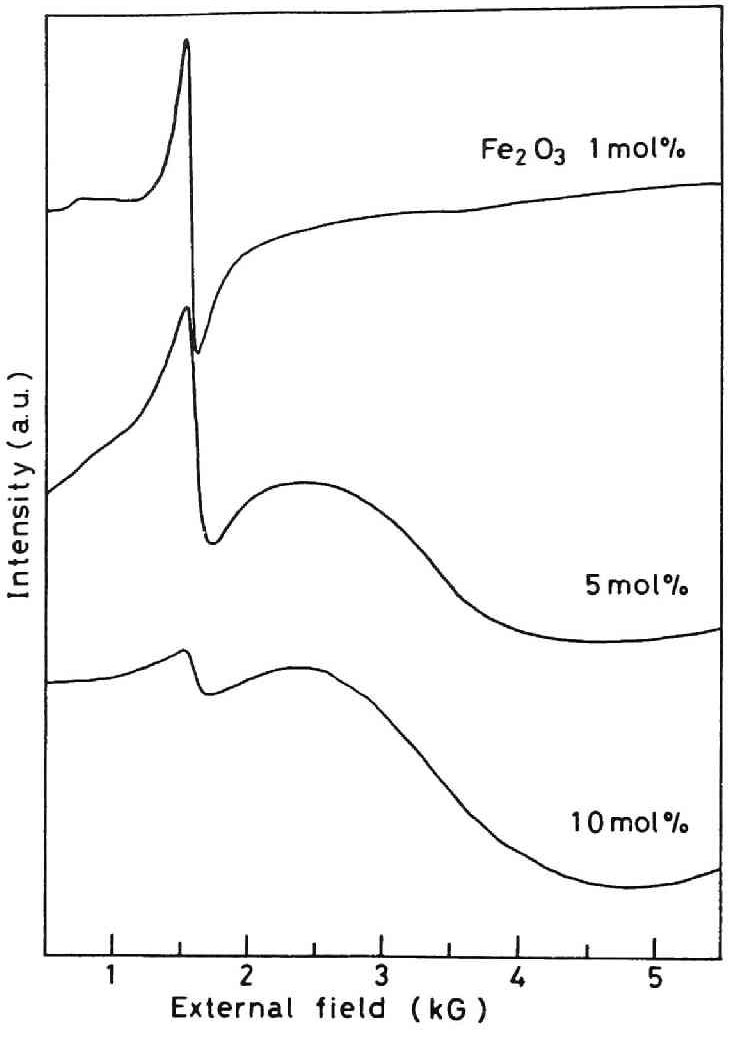

Fig.5.2 The variation of ESR spectrum with the content of Fe_2O_3 for $PbO \cdot 2B_2O_3$ glass.

fact clearly indicates that the signal at g=2.0 corresponds to the Fe^{3+} ion cluster within which the antiferromagnetic interaction is predominant at liquid helium temperature. Hence, Figs. 5.1 and 5.2 show that clustering already occurs in the glass containing a small amount of iron ions such as 5 mol% Fe_2O_3. This result is in agreement with the result of ESR measurements by Mendiratta and Sousa[16] that the formation of Fe^{3+} ion cluster starts to take place at the concentration of 3.2 mol% Fe_2O_3 in $PbO \cdot 2B_2O_3$ glass.

The variation of the ESR spectrum of $BaO \cdot 2B_2O_3$ glass containing 5 mol% Fe_2O_3 with melting temperature is shown in Fig. 5.3. A close look at this figure reveals that the intensity of the spectral line centered at g=4.3 increases while that centered at g=2.0 decreases as the melting temperature is raised, indicating that the fraction of the clustered Fe^{3+} ions is larger when the melting temperature is lower. The similar result was obtained for $PbO \cdot 2B_2O_3$ glass containing 5 mol% Fe_2O_3 as shown in Fig.5.4. In order to see this tendency more clearly, the value $N_{g=2.0}/N_{g=4.3}$, where $N_{g=2.0}$ and $N_{g=4.3}$ are the integrated intensity of the signals centered at g=2.0 and g=4.3, respectively, is plotted against the melting temperature for these two glasses in Figs.5.5 and Fig.5.6. The parameter N was estimated from the next approximate relation:

$$N = h(\Delta W)^2, \tag{5.2}$$

where h is the peak-to-peak height and ΔW is the linewidth of the signal. As clearly seen from these figures, $N_{g=2.0}/N_{g=4.3}$ decreases monotonically with increasing the melting temperature.

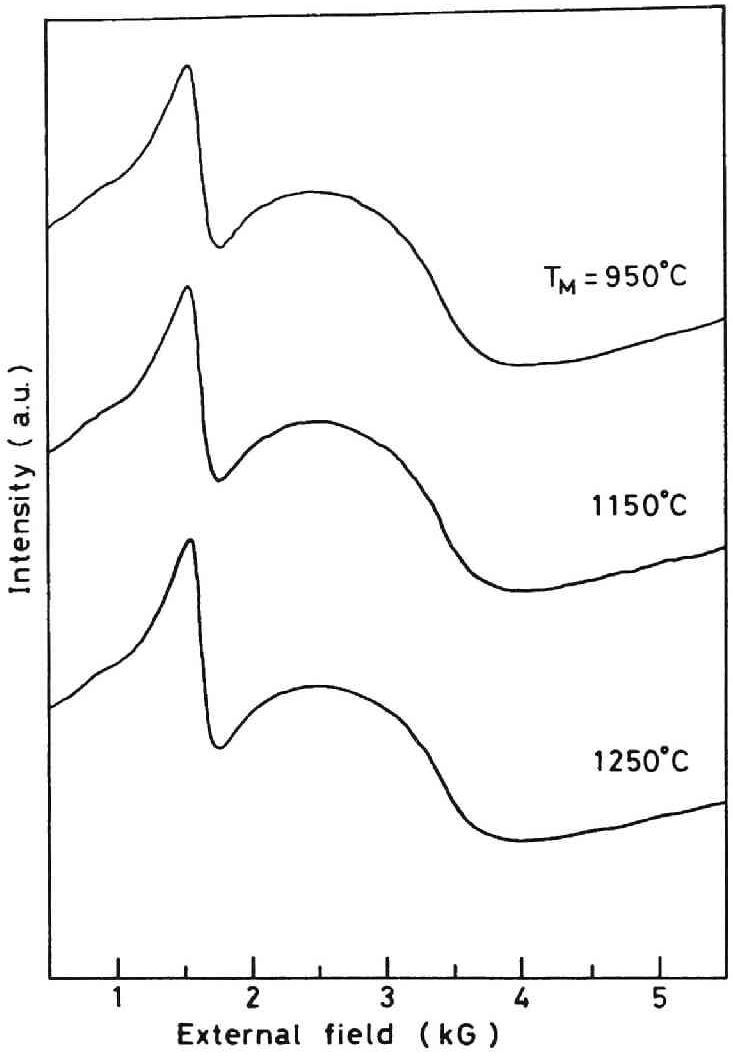

Fig.5.3 The variation of ESR spectrum with the melting temperature for $BaO \cdot 2B_2O_3$ glass containing 5 mol% Fe_2O_3. T_M denotes the melting temperature.

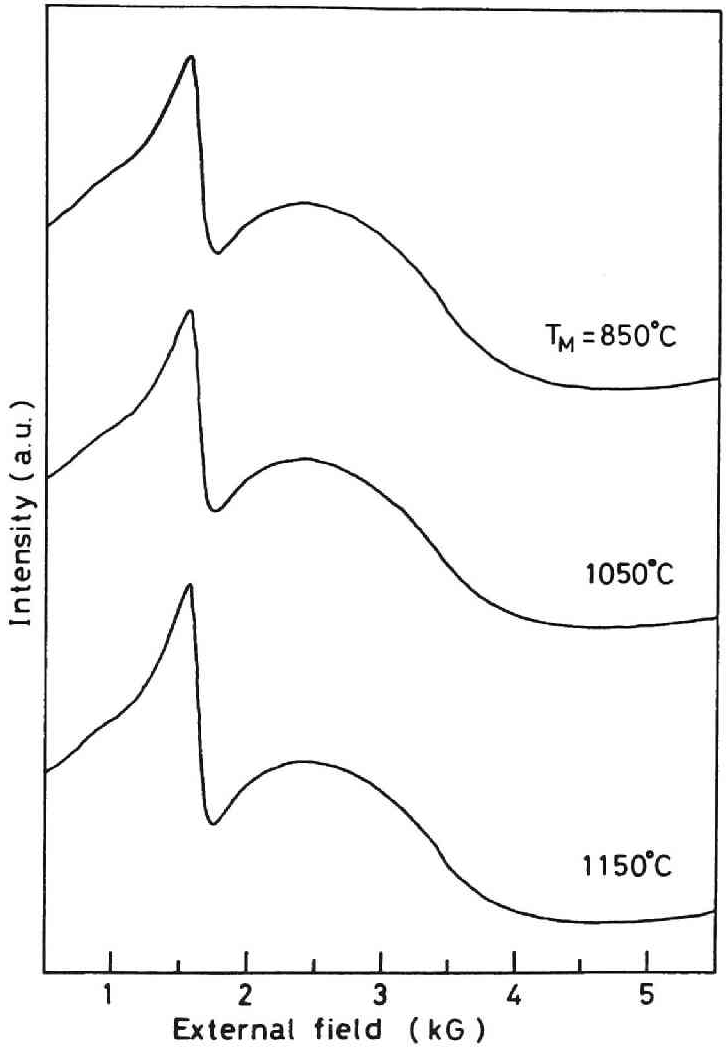

Fig.5.4 The variation of ESR spectrum with the melting temperature for $PbO \cdot 2B_2O_3$ glass containing 5 mol% Fe_2O_3.

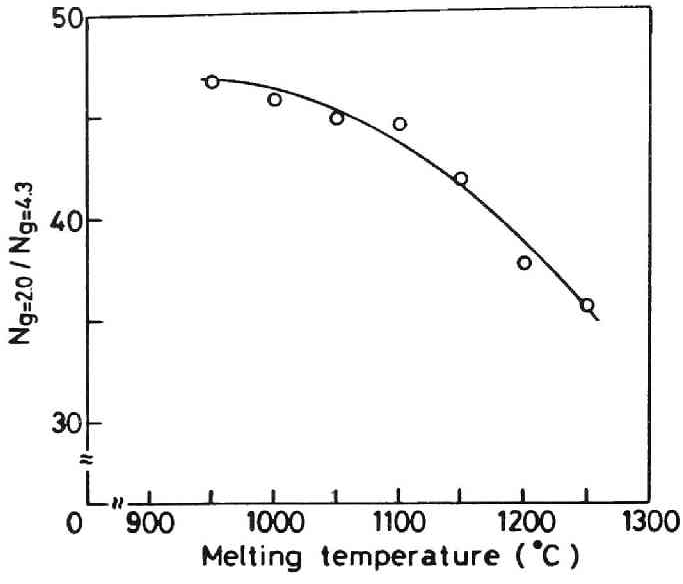

Fig.5.5 The variation of the integrated intensity ratio of the signal at g=2.0 to that at g=4.3 with the melting temperature for $BaO \cdot 2B_2O_3$ glass containing 5 mol% Fe_2O_3.

Namely, the lower the melting temperature is, the more the number of the clustered ions becomes.

Mössbauer spectra of $BaO \cdot 2B_2O_3$ and $PbO \cdot 2B_2O_3$ glasses containing 5 mol% of Fe_2O_3 obtained at various melting temperatures are shown in Figs.5.7 and 5.8, respectively. A slight absorption peak due to Fe^{2+} ion can be seen in the specimens melted at higher temperatures. The doublet due to Fe^{3+} ions is asymmetric in all the specimens. Several causes are possible for yielding such an asymmetric peak. One of them is related to the spin-spin relaxation. When the relaxation rate of spin-spin interaction is different between two γ-ray transitions corresponding to two

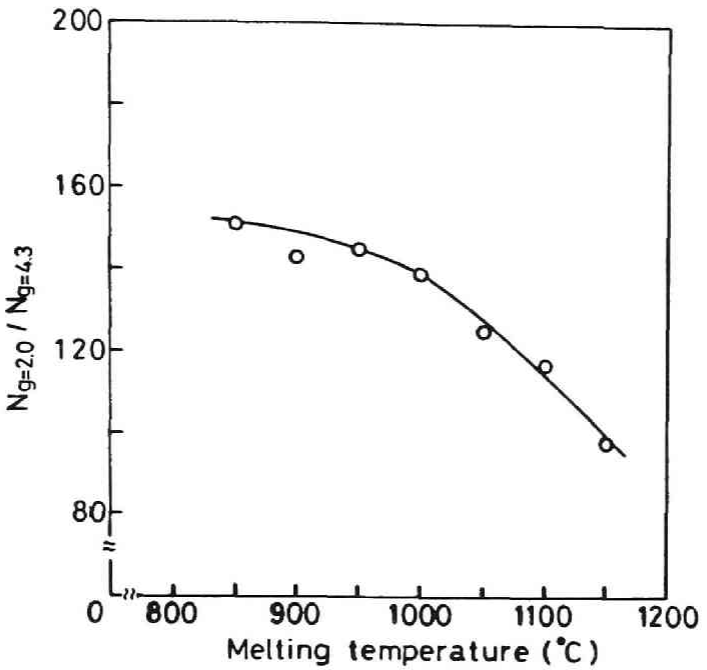

Fig.5.6 The variation of the integrated intensity ratio of the signal at g=2.0 to that at g=4.3 with the melting temperature for $PbO \cdot 2B_2O_3$ glass containing 5 mol% Fe_2O_3.

excited levels of nuclear spin due to quadrupole splitting, the absorption peak becomes asymmetrical.[21)-23)] Another possibility is the coexistence of Fe^{3+} ions laid on tetrahedral and octahedral sites in the glasses.[24)] It is not clear which is a better reason for the present glasses at present. Thus, in this study, an attempt was made to decompose the experimental spectrum into two couples of Lorentzian curves which correspond to the absorption due to Fe^{2+} ion and Fe^{3+} ion, respectively. Here, the intensity and the linewidth of two Lorentzian curves which consti-

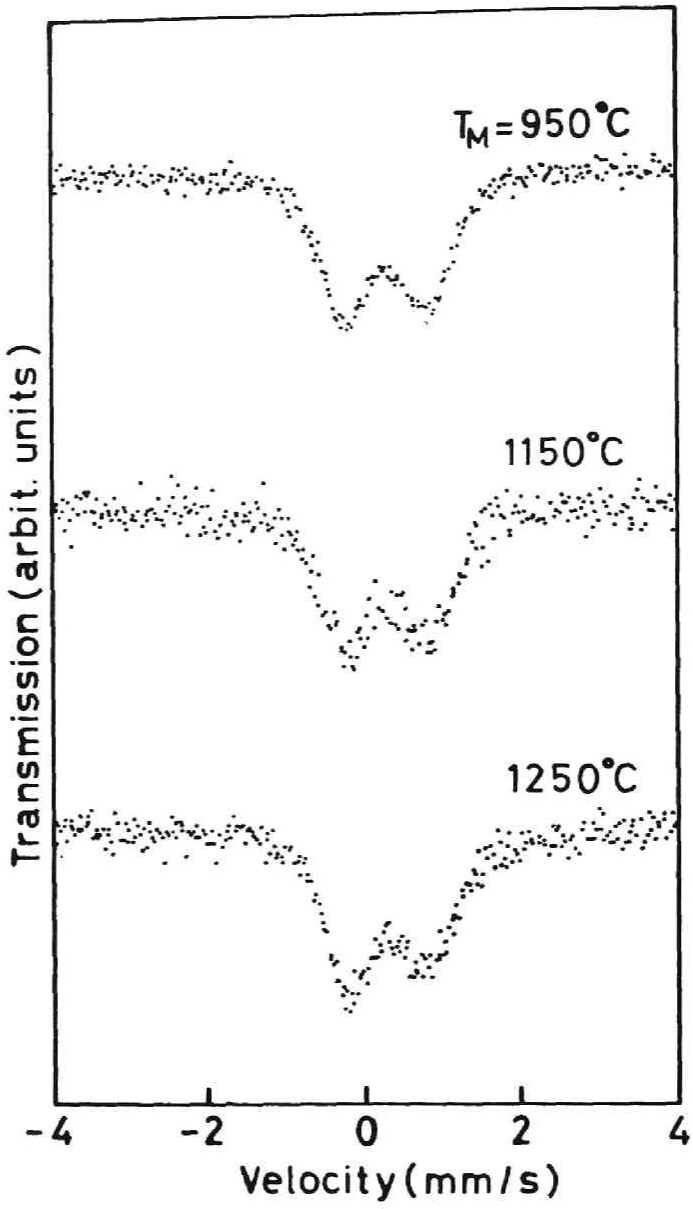

Fig.5.7 The Mössbauer spectra of $BaO \cdot 2B_2O_3$ glass containing 5 mol% Fe_2O_3 prepared by melting at several temperatures.

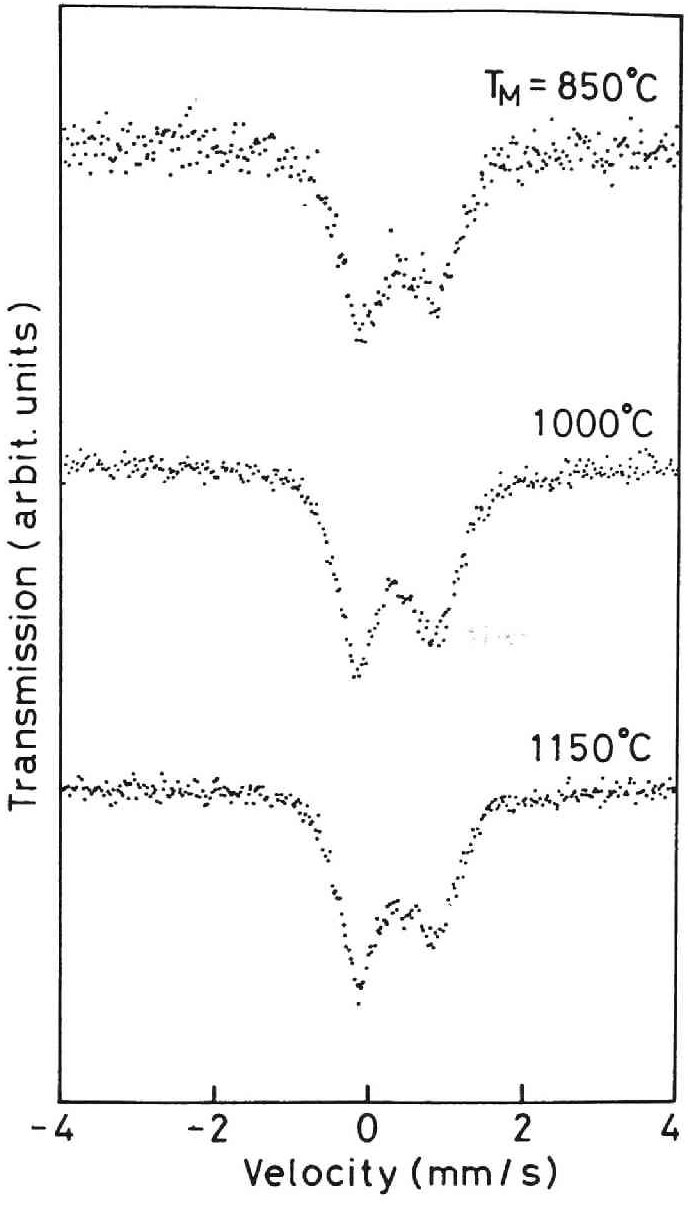

Fig.5.8 The Mössbauer spectra of $PbO \cdot 2B_2O_3$ glass containing 5 mol% Fe_2O_3 prepared by melting at several temperatures.

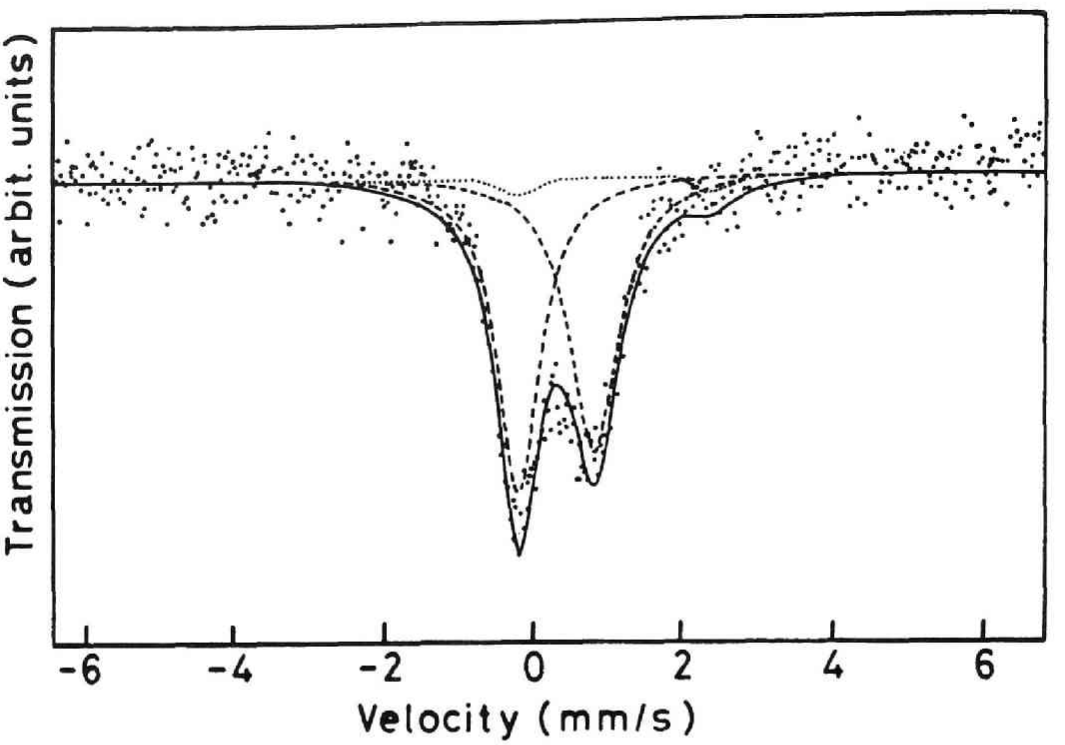

Fig.5.9 Result of parameter fitting for Mössbauer spectrum of $BaO \cdot 2B_2O_3$ glass containing 5 mol% Fe_2O_3 prepared by melting at 1250 °C. The broken and dotted curves are due to Fe^{3+} and Fe^{2+} ions, respectively.

tute one quadrupole doublet were allowed to vary with keeping the areas of them equal with each other. As an example, the result of the analysis for the barium borate glass melted at 1250 °C is shown in Fig.5.9. The solid curve is the calculated one, which agrees with the experimental data well. The Mössbauer parameters obtained from the analysis are summarized in Tables 5.1 and 5.2. It is seen from these tables that slight amounts of Fe^{2+} ions are present in the glasses and their amounts increase with

Table 5.1 Mössbauer parameters for the $BaO \cdot 2B_2O_3$ glass containing 5 mol% Fe_2O_3. T_M, IS, QS and A denote the melting temperature, isomer shift, quadrupole splitting and integrated intensity ratio, respectively.

T_M (°C)	Fe^{3+} IS (mm/s)	Fe^{3+} QS (mm/s)	Fe^{3+} A (%)	Fe^{2+} IS (mm/s)	Fe^{2+} QS (mm/s)	Fe^{2+} A (%)
950	0.31	1.04	99	1.11	2.64	1
1150	0.31	1.04	98	1.11	2.64	2
1250	0.31	1.02	94	1.12	2.63	6

Table 5.2 Mössbauer parameters for the $PbO \cdot 2B_2O_3$ glass containing 5 mol% Fe_2O_3. T_M, IS, QS and A denote the melting temperature, isomer shift, quadrupole splitting and integrated intensity ratio, respectively.

T_M (°C)	Fe^{3+} IS (mm/s)	Fe^{3+} QS (mm/s)	Fe^{3+} A (%)	Fe^{2+} IS (mm/s)	Fe^{2+} QS (mm/s)	Fe^{2+} A (%)
850	0.33	0.91	99	1.10	2.43	1
1000	0.32	0.96	98	1.10	2.43	2
1150	0.32	0.93	96	1.10	2.43	4

increasing the melting temperature. The isomer shift and the quadrupole splitting of Fe^{3+} ion do not vary so drastically with the melting temperature. Further, it is observed that the quadrupole splitting value is larger for both Fe^{3+} and Fe^{2+} ions in the $BaO \cdot 2B_2O_3$ glasses than in the $PbO \cdot 2B_2O_3$ glasses.

The variation of ESR spectrum with composition for the lithium borate glasses is shown in Fig.5.10. Two distinctive signals were observed at g=2.0 and g=4.3 for all the glasses. The integrated intensity ratio, $N_{g=2.0}/N_{g=4.3}$, was estimated from the ESR spectra and plotted against Li_2O concentration in Fig.5.11. The intensity ratio decreased until the Li_2O content reached about 30 mol% at which the intensity ratio became minimum value, and then increased rapidly with increasing Li_2O concentration. Since the ESR signals at g=2.0 and g=4.3 are attributable to the clustered and the isolated Fe^{3+} ions for the present glasses,[25] Fig. 5.11 indicates that the number of Fe^{3+} ion clusters decreases with an increase of the Li_2O content in the region of Li_2O content less than 30 mol% and increases drastically when the Li_2O content exceeds 40 mol%.

As shown in Figs.5.5 and 5.6, the clustering of Fe^{3+} ion proceeds in the glass melted at lower temperature. This phenomenon will be treated here from the thermodynamical viewpoint with some assumptions. It is assumed first that the formation of clusters occurs in the molten glass and the structure of the glass more or less reflects the structure of the melt from which that glass is formed. Thus, the next chemical equilibrium which occurs in a molten glass is taken into account:

$$Fe^{3+}(i) \rightleftharpoons Fe^{3+}(c), \qquad (5.3)$$

where Fe^{3+}(i) and Fe^{3+}(c) are the isolated and clustered Fe^{3+} ions, respectively. Although this chemical equilibrium is not maintained but changed during the cooling process, it is reasonable to assume that the state of Fe^{3+} ions in the glass prepared by melting at higher (lower) temperature reflects that in the molten glass at higher (lower) temperature. The effect of Fe^{2+} ion is negligible because of its small amount as demonstrated by the Mössbauer spectra. Since the equilibrium constant of Eq. (5.3) can be written as

$$K = \exp(-\Delta H/RT)\exp(\Delta S/R), \qquad (5.4)$$

the experimental results shown in Figs.5.5 and 5.6 clearly indicate that in order for the clustering reaction (forward reaction of Eq.(5.3)) to take place, the decrease of enthalpy is required when the amount of magnetic ions is much smaller than that of non-magnetic ions. Indeed, it was demonstrated by Moon et al.[7] that calculation[26] for random formation of cluster does not agree with the experimental result of $BaO \cdot 4B_2O_3$ glass containing Fe^{3+} ions. In other words, change of configurational entropy is disadvantageous for the cluster formation in the low concentration of magnetic ions. Although the reason of the decrease in enthalpy is not completely clear at the present time, it may be partly attributed to the decrease of energy of the system due to dipolar and superexchange interactions among iron ions in the cluster as well as the relative site energy proposed by Mendiratta and Sousa.[16]

The compositional dependence of the number of Fe^{3+} ion cluster for the lithium borate glass system shown in Figs.5.10 and

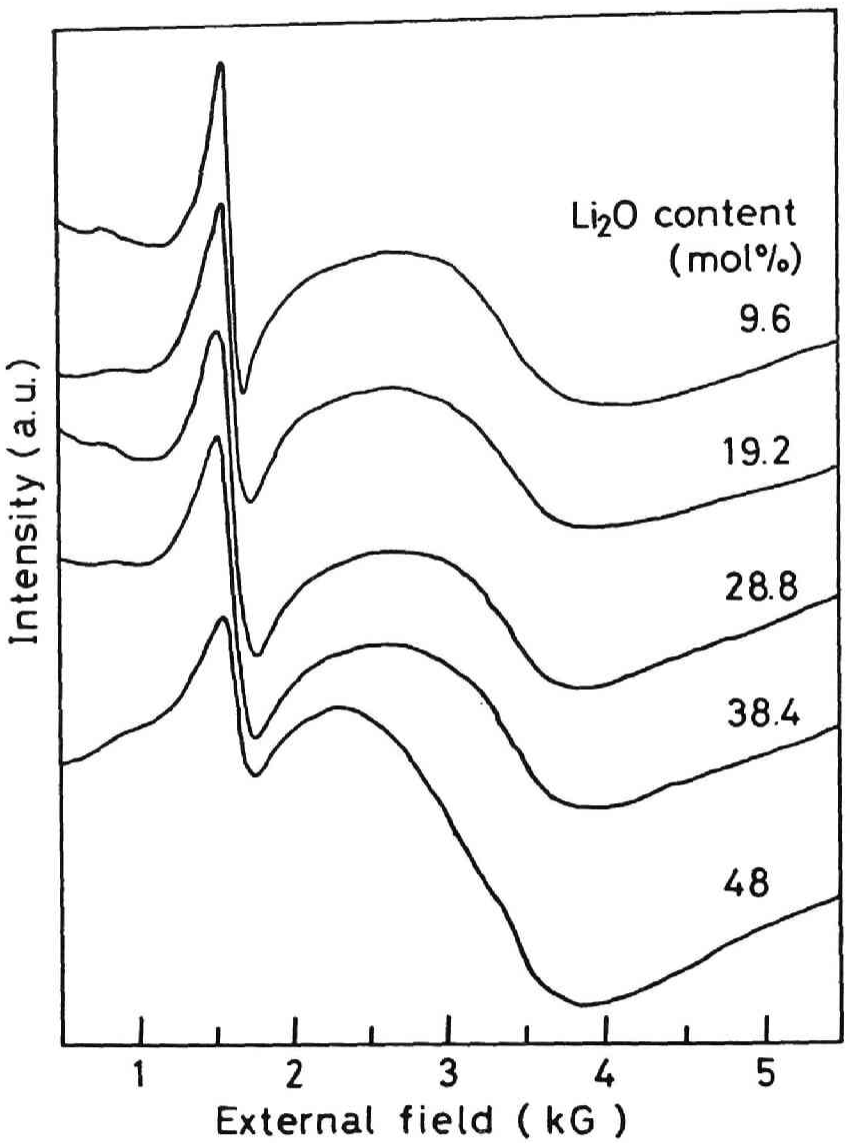

Fig.5.10 The variation of ESR spectrum with the composition for Li_2O-B_2O_3 glasses containing 4 mol% Fe_2O_3.

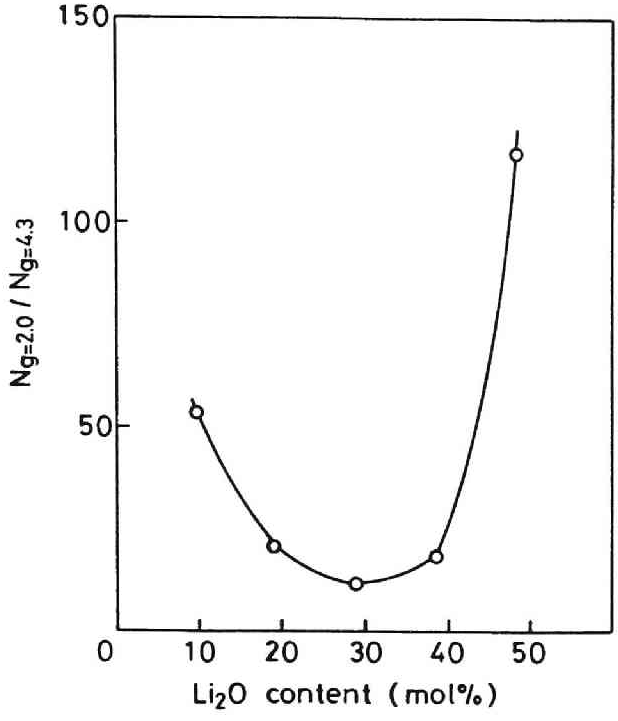

Fig.5.11 The variation of the integrated intensity ratio of the signal at g=2.0 to that at g=4.3 with the Li_2O content for Li_2O-B_2O_3 glasses containing 4 mol% Fe_2O_3.

5.11 clearly indicates that the state of Fe^{3+} ion cluster strongly depends on the glass structure. According to the NMR study on Li_2O-B_2O_3 glasses by Bray and O'Keefe,[27] the fraction of the number of four-coordinated boron ion increases with increasing the Li_2O content in the region of less than 30 mol% Li_2O in accordance with the next equation:

$$N_4 = \frac{y}{1-y} , \qquad (5.5)$$

where y denotes the molar fraction of Li_2O. The Li_2O content

dependence of N_4 begins to deviate from Eq.(5.5) at 30 mol% Li_2O. The value of N_4 reaches a maximum at 35 to 40 mol% Li_2O and then gradually decreases with increasing the Li_2O content. This fact indicates that the nonbridging oxygen begins to form at 30 mol% Li_2O and the number of nonbridging oxygen increases with further increase of Li_2O content. In particular, the rate of increase in the number of nonbridging oxygen becomes more rapid when the concentration of Li_2O is beyond 40 mol%. It is considered that these glass structures are gradually constructed during the cooling process from the melts and the construction of these glass network structures is predominant even when a small amount of Fe^{3+} ions are incorporated into the Li_2O-B_2O_3 molten glass. The Fe^{3+} ions incorporated tend to occupy preferable sites in the Li_2O-B_2O_3 glass network so as to form Fe^{3+}-O-Fe^{3+} pairs during the cooling process because the enthalpy for the cluster formation is negative as described above. However, it accompanies difficulty for the Fe^{3+} ions to take preferable sites in the glasses with less than 30 mol% Li_2O because the network structure of these glasses is rigid due to nonexistence of the nonbridging oxygen ions and formation of four-coordinated boron ions. Therefore, the change of entropy instead of enthalpy determines the state of Fe^{3+} ions in these glasses, resulting in a large number of isolated Fe^{3+} ions. The decrease in the number of clustered Fe^{3+} ion with the increase of the Li_2O content in this composition range, which is shown in Figs.5.11, is explainable in terms of the fact that the addition of Li_2O increases the number of four-coordinated boron to make the glass network more rigid. On

the other hand, the network structure of the glasses with more than 30 mol% Li_2O is more flexible because of the presence of nonbridging oxygen ions, so that the Fe^{3+} ions can readily take situations with lower internal energy, i.e. Fe^{3+}-O-Fe^{3+} pairs. As a result, the number of cluster increases with increasing the content of Li_2O. In particular, a great number of clusters are formed in the glass with the Li_2O content of about 50 mol% where about 70 % of the present boron ions possess one nonbridging oxygen, which can be estimated from the experimental results by Bray and O'Keefe.[27)]

5.2 Iron Ion Cluster in Gels and Gel-Derived Glasses

Nowadays, the sol-gel method is prevailingly utilized for preparation of oxide glasses and ceramics. The superiority of this method lies in the fact that it makes us possible to mix starting materials at molecular level and the resultant product is expected to be homogeneous.[28] For example, fine ceramic particles prepared by this method give us homogeneous and denser sintered bodies at lower elevated temperatures than conventional solid state reaction.[29)-34)] Besides, by utilizing this method, ceramic fibers[35)-38)] and thin films[39)-43)] can be produced from sol-derived precursor gels with such shapes. Because the sol-gel process to produce glass is rather different from the melt-quenching method, it is interesting to clarify whether the Fe^{3+} ion pairs or clusters detected in the melt-derived glasses are also formed in sol-gel-derived glasses or not. In the present section, an attempt was made to characterize the state of Fe^{3+} ions in the sol-gel-derived amorphous Fe_2O_3-SiO_2 system by means of ESR spectroscopy.

Silicon tetraethoxide, $Si(OC_2H_5)_4$ and tris(acetylacetonato)-iron(III), $Fe(acac)_3$ were used as the starting reagents. They were weighed to produce nominal compositions of $xFe_2O_3 \cdot (100-x)$-SiO_2 (mol%) with $0.5 \leq x \leq 10$ and added into ethanol used as a solvent. The mixture of ethanol, water and 35 wt% hydrochloric acid as a catalyst of the prescribed amounts (Table 5.3) was then added slowly into the alkoxide-acetonato mixed solution under stirring. During this process, $Si(OC_2H_5)_4$ and $Fe(acac)_3$ were dissolved completely and a clear sol solution was obtained. After being stirred overnight for the further hydrolysis reac-

Table 5.3 Amounts of starting chemicals for the preparation of the Fe_2O_3-SiO_2 glasses by the sol-gel method

Composition (mol%)		$Fe(acac)_3$ (g)	$Si(OC_2H_5)_4$ (g)	C_2H_5OH (ml)	H_2O (ml)	HCl_{aq} (ml)
Fe_2O_3	SiO_2					
0.5	99.5	0.35	20.73	87.6	27.0	0.1
0.7	99.3	0.49	20.69	87.6	27.0	0.1
1	99	0.71	20.62	87.6	27.0	0.1
1.5	98.5	1.06	20.52	87.6	27.0	0.5
2	98	1.41	20.42	87.6	27.0	0.5
3	97	2.12	20.21	87.6	27.0	1
4	96	2.83	20.00	87.6	27.0	1
5	95	3.53	19.79	87.6	27.0	1.5
7	93	4.94	19.37	87.6	27.0	2
10	90	7.06	18.75	87.6	27.0	3

tion, the resultant sol solution was heated to 60 °C until a homogeneous desiccated gel resulted. The above procedure to prepare gels is shown schematically in Fig.5.12. The desiccated gels obtained were ground into powders and heat-treated at several temperatures ranging from 300 °C to 800 °C for 24 h in air. X-ray diffraction analysis was carried out to ascertain whether the specimens thus obtained were amorphous or not, and to identify the crystalline species if precipitated. ESR measurements were carried out at room temperature on the gels and heat-treated specimens using a Varian E-Line spectrometer operating at X-band frequency (ν = 9.5 GHz). The condition for the measurements was the same as that described in section 5.1.

The results of X-ray diffraction analysis are summarized in Table 5.4. As seen from the table, all of the desiccated gels and the heat-treated specimens with $x \leq 4$ were amorphous while α-

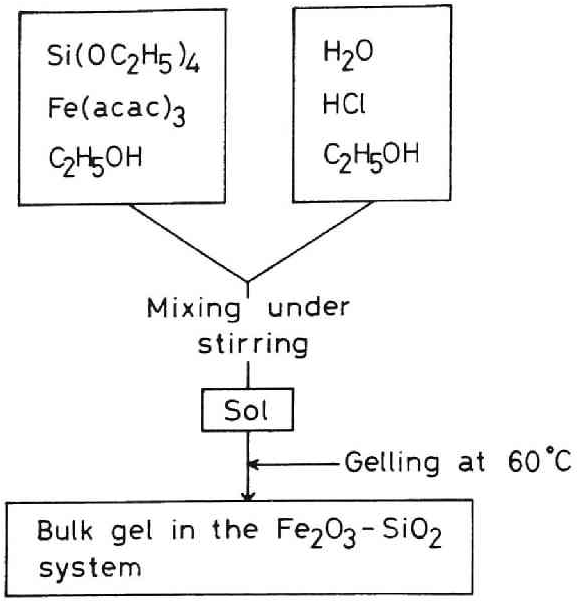

Fig.5.12 Flow chart for preparing gels of the Fe_2O_3-SiO_2 system.

Table 5.4 Results of X-ray diffraction analysis

Sample Fe_2O_3 (mol%)	Heat treatment temperature (°C) gel	300	400	500	600	700	800
x = 2	A	A	A	A	A	A	A
x = 3	A	A	A	A	A	A	A
x = 4	A	A	A	A	A	A	A
x = 5	A	H	H	H	H	H	H
x = 7	A	H	H	H	H	H	H
x = 10	A	H	H	H	H	H	H

A : Amorphous, H : Hematite

Fe_2O_3 precipitated in the heat-treated specimens with $x \geq 5$. The precipitation of other crystals than α-Fe_2O_3 was not observed.

ESR spectra of the desiccated gels are shown in Fig.5.13. Three distinctive resonance signals centered at g=6.0, 4.3 and 2.0 are observed. While the intensity of the signal centered at

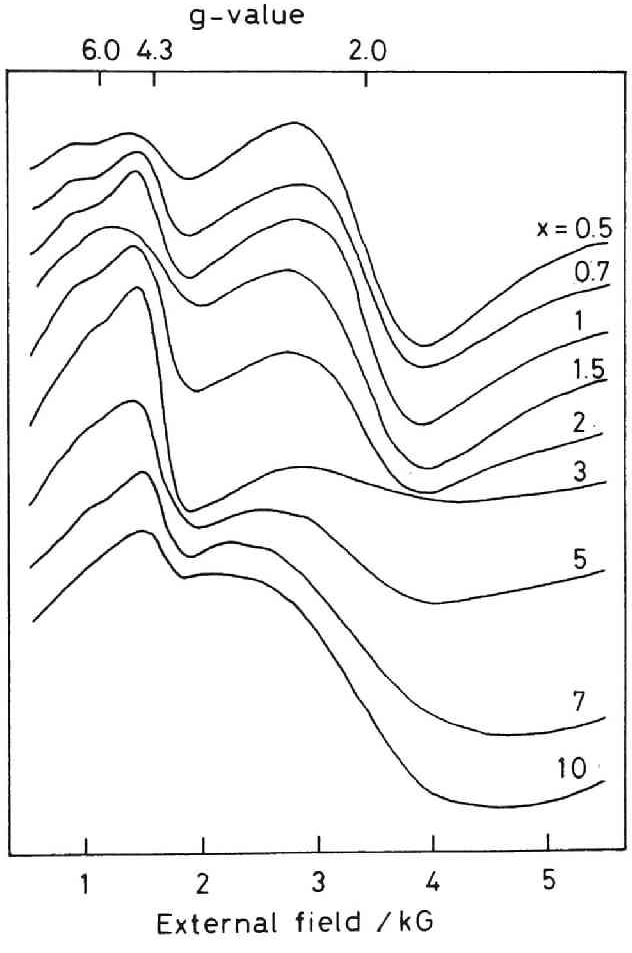

Fig.5.13 ESR spectra of the desiccated gels with nominal compositions of xFe_2O_3 $(100-x)SiO_2$.

g=2.0 decreases at first and thereafter increases as the concentration of iron ions increases, that centered at g=4.3 increases at first and thereafter decreases. According to the previous investigations,[17),18)] the isolated Fe^{3+} ions in axial crystal fields give the signals at g=2.0 and 6.0, whereas the signal at g=4.3 is assigned to those in orthorhombic crystal fields. The Fe^{3+} ions in spin pair Fe^{3+}-O-Fe^{3+} also give a signal at g=2.0. To see the variation of intensity of these signals more clearly,

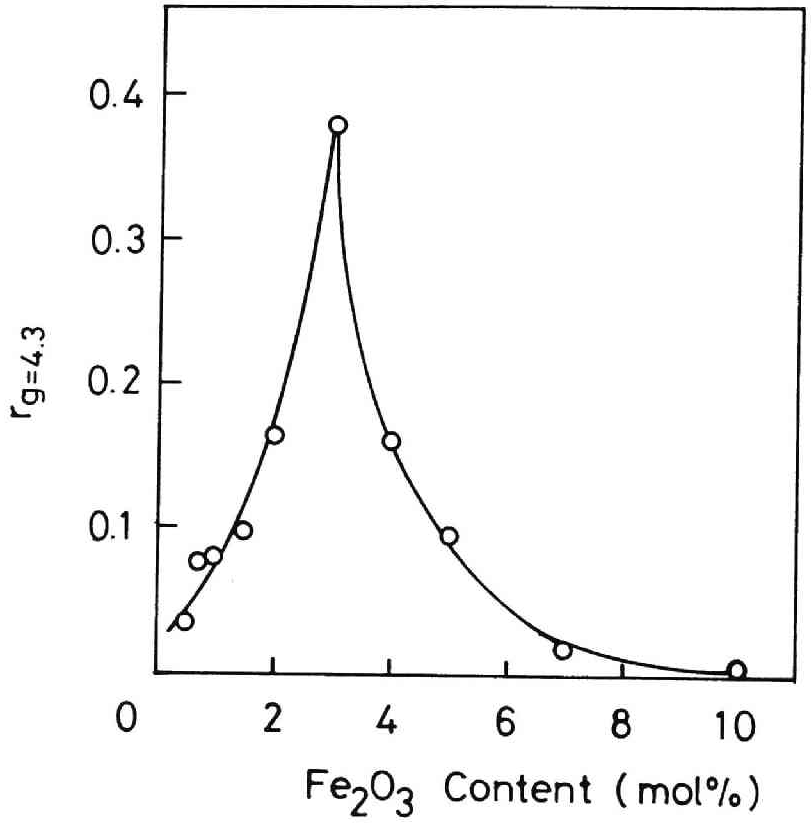

Fig.5.14 Composition dependence of the intensity ratio $r_{g=4.3}$ of the signal at g=4.3 to that at g=2.0 for the gel.

the ratio of the signal intensity at g=4.3 to that at g=2.0, $r_{g=4.3}$ was plotted against the concentration of Fe_2O_3 in Fig. 5.14. In estimating $r_{g=4.3}$, the intensity N of the signal was determined from Eq.(5.2). It is seen from this figure that the ratio $r_{g=4.3}$ increases for $x \leq 3$ and decreases for $x \geq 3$, indicating that some change of the state of Fe^{3+} ions occurs at x=3. From the fact that the signals at g=6.0 appear distinctly for $x \leq 3$ while they almost disappear for $x \geq 3$ as seen in Fig.5.14, it can be stated that a large part of isolated iron ions exist at the axial sites for $x \leq 3$ while they scarcely exist in the range $x \geq 3$. The signal at g=2.0 observed for $x \leq 3$ decreases in intensity along with the signal at g=6.0 with increasing x, indicating that it is attributed to the isolated iron ions at the axial sites but not to the spin pairs. On the other hand, the signal at g=2.0 for $x \geq 3$ is not imputable to the isolated iron ions at the axial sites but the spin pairs because its intensity increases without any indication of appearance of the signal at g=6.0 with increasing the concentration of iron ions. Thus, it is concluded that the signals at g=2.0 for $x \leq 3$ and $x \geq 3$ are attributable to the isolated Fe^{3+} ions in the axial crystal fields and the spin pairs, respectively. Moreover, it is seen from the variation of $r_{g=4.3}$ that the fraction of isolated Fe^{3+} ions in the axial crystal fields decreases with increasing the Fe_2O_3 content up to 3 mol% of Fe_2O_3, above which the number of spin pairs increases.

Recently, Tanabe et al.[44] have reported that Fe^{3+} ions have a tendency for forming an iron(III) hydroxide rather than Fe-O-Si

bond in the Fe_2O_3-SiO_2 gels when the amount of water added for hydrolysis is large compared to that stoichiometrically required. Since the molar ratio of water to $Si(OC_2H_5)_4$ in the present study is larger than 15 (Table 5.3), a large part of the Fe^{3+} ions are coordinated by OH^- and H_2O in the gels. Besides, because the acetylacetonato complex is relatively stable against the hydrolysis in general, several acetylacetonato groups which coordinate the Fe^{3+} ion may remain unchanged. Therefore, it seems plausible to consider that most of the Fe^{3+} ions are present in the form of $[Fe(OH)_x(H_2O)_y(OR)_{6-x-y}]^{y-3}$ (R=Si, $C(CH_3)CHCOCH_3$ etc.) in the gels. Accordingly, the symmetry of this complex may change from the axial symmetry to the orthorhombic one as the concentration of iron ions increases.

The variations of the ESR spectra with the heat treatment temperature for $1Fe_2O_3 \cdot 99SiO_2$ and $3Fe_2O_3 \cdot 97SiO_2$, which are amorphous at any heat treatment temperatures as revealed by X-ray diffraction, are shown in Figs.5.15 and 5.16, respectively. Both figures show that the intensity of the signal at g=4.3 decreases and the signal at g=2.0 becomes sharper as the heat treatment temperature is raised. Figure 5.17 shows the variation of the ESR spectrum of the specimen heat-treated at 500 °C for 24 h with Fe_2O_3 content. It is found that the intensity of the resonance signal at g=4.3 decreases monotonically with increasing the concentration of Fe_2O_3.

From the ESR spectra of the heat-treated specimens having x=1 and x=3, shown in Figs.5.15 and 5.16, $r_{g=4.3}$ was estimated and plotted against the heat treatment temperature in Fig.5.18.

This figure also shows the results for specimens with x=0.5, 2 and 4. It is found that the value of $r_{g=4.3}$ decreases as the heat treatment temperature is increased, indicating that the number of spin pairs gradually increases with the increase of heat treatment temperature. From these facts, it is considered that the isolated Fe^{3+} ions possibly presenting as an iron(III) hydroxide or iron(III) partly coordinated by acetylacetonato

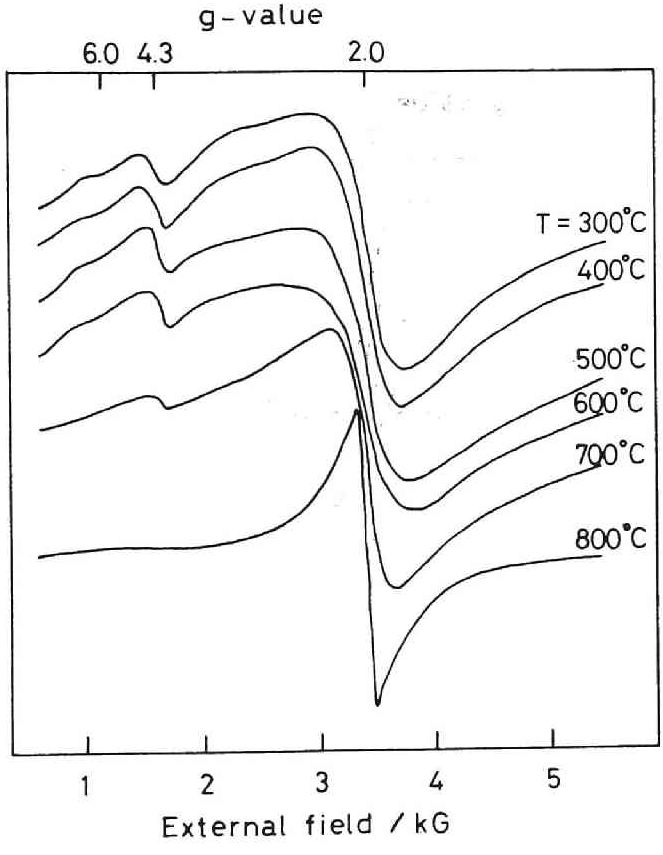

Fig.5.15 ESR spectra of $1Fe_2O_3 \cdot 99SiO_2$ gels heat-treated at several temperatures. T denotes the heat treatment temperature.

groups in the gels as mentioned above may undergo the following polycondensation reaction:

$$Fe\text{-}OH + HO\text{-}Fe \longrightarrow Fe\text{-}O\text{-}Fe + H_2O, \qquad (5.6)$$

or pyrolysis reaction of residual acetylacetonato groups schematically represented by the next equation:

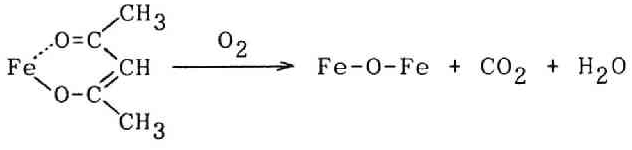

(5.7)

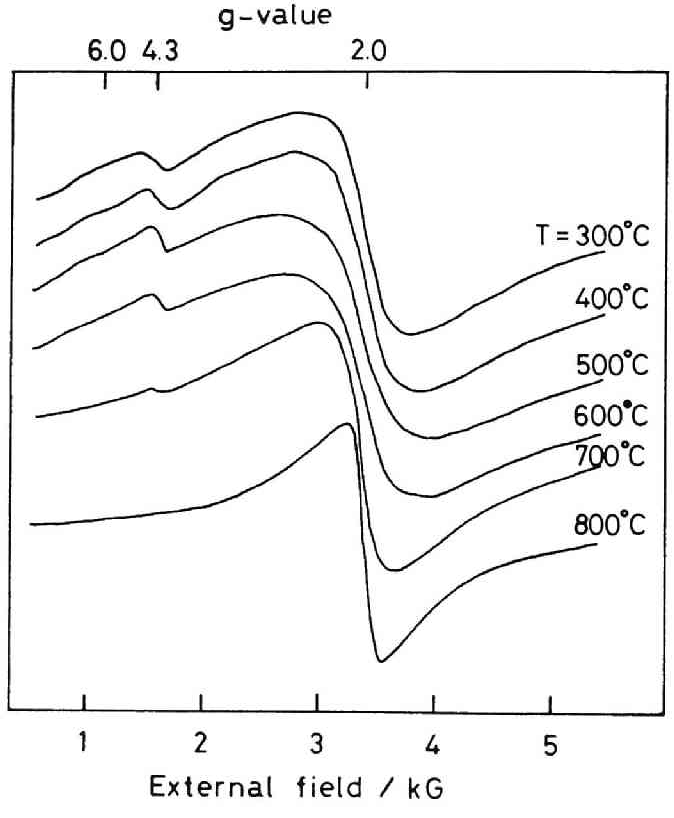

Fig.5.16 ESR spectra of $3Fe_2O_3 \cdot 97SiO_2$ gels heat-treated at several temperatures.

to form spin pairs during the heat treatment process.

The variation of $r_{g=4.3}$ with the Fe_2O_3 content estimated from the ESR spectra given in Fig.5.17 is shown in Fig.5.19 together with the results of the other heat-treated specimens. It is observed that $r_{g=4.3}$ decreases monotonically with the increase of Fe_2O_3 content in all the specimens, indicating that the number of spin pairs becomes larger as the concentration of Fe^{3+} ions

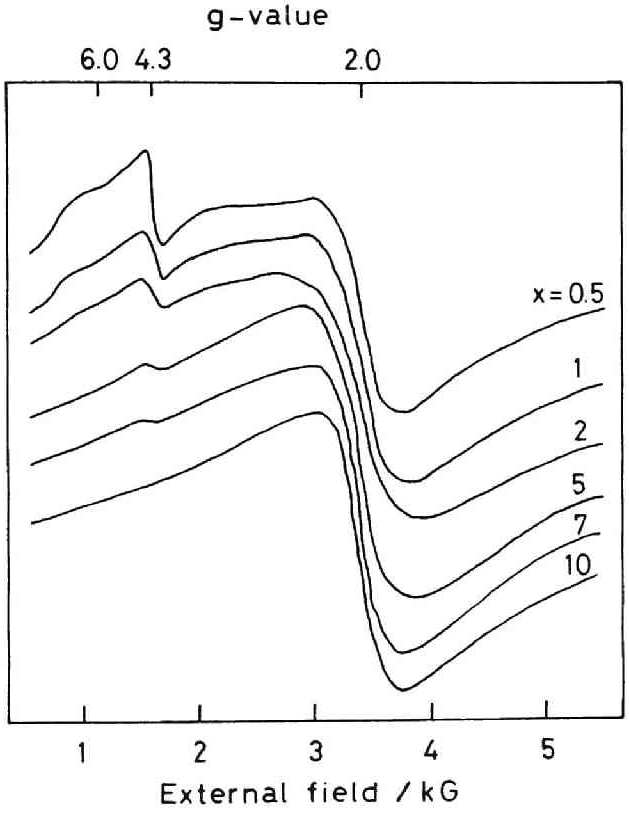

Fig.5.17 ESR spectra of $xFe_2O_3 \cdot (100-x)SiO_2$ gels heat-treated at 500 °C.

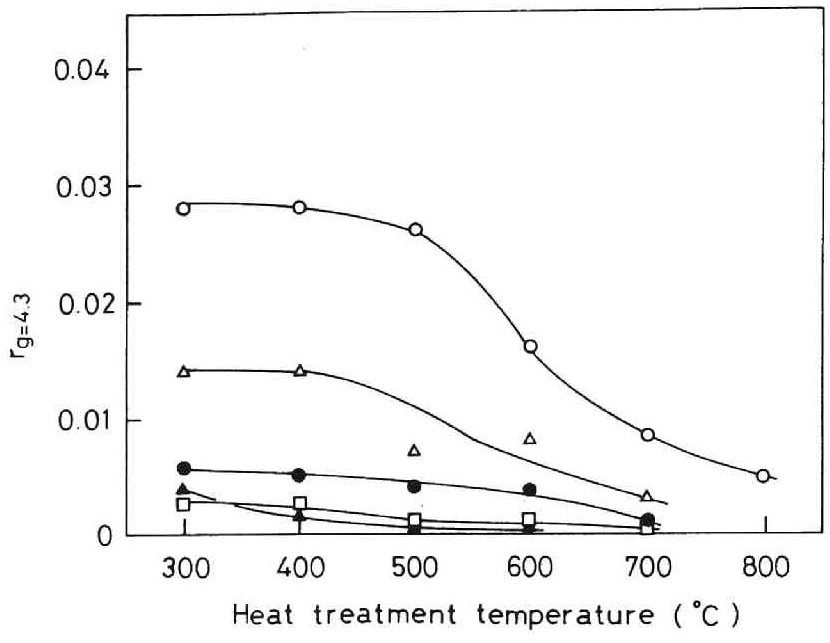

Fig.5.18 Variation of the intensity ratio $r_{g=4.3}$ of the signal at g=4.3 to that at g=2.0 with heat treatment temperature for $xFe_2O_3 \cdot (100-x)SiO_2$ gels. (○: x=0.5, △: x=1, ●: x=2, □: x=3, ▲: x=4)

increases. A similar concentration dependence of $r_{g=4.3}$ has been reported for $CaO \cdot SiO_2$ and $0.2CaF_2 \cdot 0.8CaO \cdot SiO_2$ glasses prepared from the melts.[10] However, the absolute values of $r_{g=4.3}$ in the present glasses are much smaller than those in both $CaO \cdot SiO_2$ and $0.2CaF_2 \cdot 0.8CaO \cdot SiO_2$ glasses, in other words, the signals at g=2.0 due to spin pairs are much more intensive. This fact may suggest that Fe^{3+} ions form spin pairs more easily in the present sol-gel-derived Fe_2O_3-SiO_2 glasses than in the above-mentioned melt-derived silicate glasses, although the glass composition is dif-

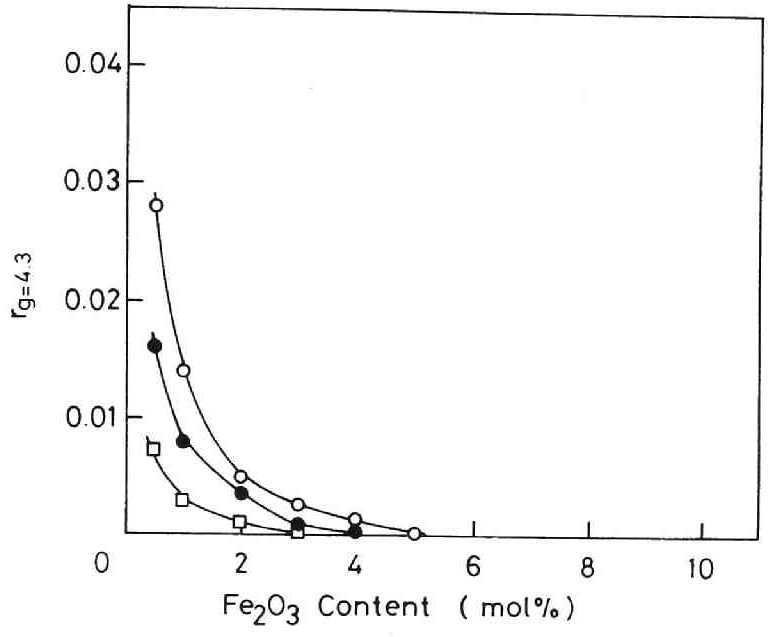

Fig.5.19 Composition dependence of the intensity ratio $r_{g=4.3}$ of the signal at g=4.3 to that at g=2.0 in the specimen heat-treated at several temperatures. (○: 400 °C, ●: 500 °C, □: 700 °C)

ferent, making the simplified comparison difficult. This result, however, disagrees with that by Yoshio et al.[45], who stated that there exist isolated Fe^{3+} ions in the sol-gel-derived silicate glasses containing Fe_2O_3 as large as 30 mol% on the basis of IR spectroscopy, namely Fe^{3+} ions are homogeneously distributed in that glass. Furthermore, it has been revealed from the ESR measurements that Ti^{3+} ions in the sol-gel-derived B_2O_3-SiO_2-TiO_2 glasses were distributed very homogeneously.[46] The discrepancy between the present result and the previous ones may be explain-

able in terms of the difference in the amount of water added for preparing gels. In the case of Fe_2O_3-SiO_2 and B_2O_3-SiO_2-TiO_2 glasses previously studied, the water was supplied from the humidity in air. In such a case the amount of water consumed for hydrolysis of starting materials is very small, leading to the formation of Fe-O-Si or Ti-O-Si bonds in the gels.[44] As a result, the gels thus obtained may possibly be converted to the glasses containing homogeneously distributed Fe^{3+} or Ti^{3+} ions. On the other hand, the amount of added water is very large in the present case. Besides, alkoxides of iron or titanium were used as the starting materials. They are subject to hydrolysis more readily than the acetylacetonato complex used here. Hence, $[Fe(OH)_x(H_2O)_y(OR)_{6-x-y}]^{y-3}$ instead of Fe-O-Si bond mainly forms in the gels, making the spin pair formation easier in the heat-treated specimens as described above.

5.3 Conclusions

The ESR measurements on $BaO \cdot 2B_2O_3$ and $PbO \cdot 2B_2O_3$ glasses containing 5 mol% Fe_2O_3 prepared by melting at several temperatures from 850 to 1250 °C revealed that the intensity of the spectral line centered at g=2.0 decreases while that at g=4.3 increases with increasing the melting temperature. Namely, the higher the melting temperature became, the less the amount of the clustered Fe^{3+} ions in the resultant glass became. This fact shows that a chemical equilibrium between isolated and clustered Fe^{3+} ions, which has an influence on the state of Fe^{3+} ions in the resultant glass, exists in the molten state and that the driving force for the clustering is the decrease of enthalpy. This decrease of enthalpy may arise from dipolar and superexchange interactions among the Fe^{3+} ions.

The state of Fe^{3+} ion cluster depended on the Li_2O content for the lithium borate glasses. The number of Fe^{3+} ion cluster decreased with increasing the Li_2O content in the range of less than 30 mol% Li_2O, while it increased rapidly in the range of more than 40 mol% Li_2O. This fact was explained in terms of the Li_2O content dependence of the flexibility of glass network structure which results from the variation of oxygen coordination number to boron ion and the change of the number of present nonbridging oxygen ions with glass composition.

The state of Fe^{3+} ions in the sol-gel-derived gels and glasses of the Fe_2O_3-SiO_2 system can be summarized as follows. In the gels with low Fe_2O_3 content, Fe^{3+} ions are present as isolated ones situated in the axial crystal fields. The number

of them decreases while that of the isolated Fe^{3+} ions in the orthorhombic crystal fields increases as the concentration of Fe_2O_3 increases up to 3 mol% of Fe_2O_3. Above 3 mol%, Fe-O-Fe spin pairs are formed. In the glasses obtained by heating the gels, almost all the Fe^{3+} ions are present as Fe-O-Fe spin pairs. The fraction of Fe^{3+} ions forming spin pairs becomes larger as the concentration of iron ions is increased and the heat treatment temperature is raised. It is considered that the state of Fe^{3+} ions in the sol-gel-derived glasses depends on the chemical environment of Fe^{3+} ions in the precursor gels.

References

1) R.A.Verhelst, R.W.Kline, A.M.de Graaf and H.O.Hooper, Phys. Rev., B11, 4427 (1975)

2) H.R.Rechenberg, L.H.Bieman, F.S.Huang and A.M.de Graaf, J. Appl. Phys., **49**, 1638 (1978)

3) J.P.Jamet, J.C.Dumais, J.Seiden and K.Knorr, J. Magn. Magn. Mat., **15-18**, 197 (1980)

4) J.P.Sanchez, J.M.Friedt, R.Horne and A.J.van Duyneveldt, J. Phys., C17, 127 (1984)

5) J.P.Renard, J.P.Miranday and F.Varret, Solid State Commun., 35, 41 (1980)

6) A.Bonnenfant, J.M.Friedt, M.Maurer and J.P.Sanchez, J. de Phys., **43**, 1475 (1982)

7) D.W.Moon, J.M.Aitken, R.K.MacCrone and G.S.Cieloszyk, Phys. Chem. Glasses, **16**, 91 (1975)

8) R.G.Gupta, R.G.Mendiratta, S.S.Sekhon, R.Kamal, S.K.Suri and N.Ahmad, J. Non-Cryst. Solids, **33**, 121 (1979)

9) R.A.Anderson and R.K.MacCrone, J. Non-Cryst. Solids, **14**, 112 (1974)

10) N.Iwamoto, Y.Makino and S.Kasahara, J. Non-Cryst. Solids, **55**, 113 (1983)

11) L.Trombetta, J.Williams and R.K.MacCrone, Amorphous Magnetism II, edited by R.A.Levy and R.Hasegawa (Plenum Press, New York, 1977), p.643

12) H.Laville and J.C.Bernier, J. Mat. Sci., 15, 73 (1980)

13) S.K.Mendiratta, R.Horne and A.J.van Duyneveldt, Solid State Commun., **52**, 371 (1984)

14) Y.Syono, A.Ito and O.Horie, J. Phys. Soc. Jpn., **46**, 793 (1979)

15) C.Chaumont and J.C.Bernier, J. de Phys., **43**, C9-685 (1982)

16) S.K.Mendiratta and E.G.D.Sousa, J. Mat. Sci. Lett., **7**, 733 (1988)

17) T.Castner,Jr., G.S.Newell, W.C.Holton and C.P.Slichter, J. Chem. Phys., **32**, 668 (1960)

18) H.H.Wickman, M.P.Klein and D.A.Shirley, J. Chem. Phys., **42**, 2113 (1965)

19) C.M.Brodbeck, J. Non-Cryst. Solids, **40**, 305 (1980)

20) A.K.Bandyopadhyay, J.Zarzycki, P.Auric and J.Chappert, J. Non-Cryst. Solids, **40**, 353 (1980)

21) M.Blume, Phys. Rev. Lett., **18**, 305 (1967)

22) M.Blume, Phys. Rev. Lett., **14**, 96 (1965)

23) N.Thrane and G.Trumpy, Phys. Rev., B1, 153 (1970)

24) R.A.Levy, C.H.P.Lupis and P.A.Flinn, Phys. Chem. Glasses, 17, 94 (1976)

25) J.P.Sanchez and J.M.Friedt, J. de Phys., **43**, 1707 (1982)

26) R.E.Behringer, J. Chem. Phys., **29**, 537 (1958)

27) P.J.Bray and J.G.O'Keefe, Phys. Chem. Glasses, **4**, 37 (1963)

28) S.Sakka, Treatise on Materials Science and Technology Vol.22, edited by M.Tomozawa and R.H.Doremus (Academic Press, New York, 1982), p.129

29) K.S.Mazdiyasni, R.T.Dolloff and J.S.Smith II, J. Am. Ceram. Soc., **52**, 523 (1969)

30) L.M.Brown and K.S.Mazdiyasni, J. Am. Ceram. Soc., **55**, 541 (1972)

31) L.Springer and M.F.Yan, Ultrastructure Processing of Glasses, Ceramics and Composites, edited by L.L.Hench and D.R.Urich (John Wiley & Sons, New York, 1984), p.464

32) K.Tanaka, A.Nozue and K.Kamiya, J. Mat. Sci., **25**, 3551 (1990)

33) K.Tanaka, A.Nozue and K.Kamiya, Jpn. J. Appl. Phys., **28**, L934 (1989)

34) A.Nozue, H.Nasu, K.Tanaka and K.Kamiya, Jpn. J. Appl. Phys., **28**, L2161 (1989)

35) K.Kamiya, K.Tanimoto and T.Yoko, J. Mat. Sci. Lett., **5**, 402 (1986)

36) K.Kamiya, T.Yoko and M.Bessho, J. Mat. Sci., **22**, 937 (1987)

37) K.Kamiya, T.Yoko, K.Tanaka and H.Itoh, J. Ceram. Soc. Jpn., **95**, 1157 (1987)

38) S.Sakka, Sol-Gel Technology for Thin Films, Fibers, Preforms, Electronics, and Specialty Shapes, edited by L.C.Klein (Noyes Publications, New Jersey, 1988), p.140

39) G.Kordas, R.A.Weeks and N.Arfsten, J. Appl. Phys., **57**, 3812 (1985)

40) T.Yoko, K.Kamiya and S.Sakka, J. Ceram. Soc. Jpn., **95**, 150 (1987)

41) T.Yoko, K.Kamiya, A.Yuasa, K.Tanaka and S.Sakka, J. Non-Cryst. Solids, **100**, 483 (1988)

42) J.C.Huling and G.L.Messing, J. Am. Ceram. Soc., **71**, C-222 (1988)

43) H.Dislich, Sol-Gel Technology for Thin Films, Fibers, Preforms, Electronics, and Specialty Shapes, edited by L.C.Klein (Noyes Publications, New Jersey, 1988), p.50

44) S.Tanabe, K.Hirao and N.Soga, J. Non-Cryst. Solids, **100**, 388 (1988)

45) T.Yoshio, C.Kawaguchi, F.Kanamaru and K.Takahashi, J. Non-Cryst. Solids, **43**, 129 (1981)

46) S.Dave and R.K.MacCrone, J. Non-Cryst. Solids, **71**, 303 (1985)

CHAPTER 6

MAGNETIC PROPERTIES OF IRON OXIDE-BASED FINE PARTICLES AND THIN FILMS

The magnetic behavior of fine particles and thin films based on iron oxide has several common features with that of iron-containing amorphous oxides because in fine particles and thin films, major part of the magnetic moments are present at the surface and are necessarily forced to be in random arrangements. It has been reported that there exist a distribution of hyperfine field and a reduction of the superexchange interactions due to the surface effect for several iron oxide-based fine particles and thin films as well as bulk surface.[1)-5)] Besides, in particular for the thin films, anisotropy due to their shape effect manifests in the magnetic properties. Furthermore, it is well known that the fine particles of sufficiently small size show superparamagnetism which essentially dominates the cluster spin glass transition of iron-containing oxide and fluoride glasses as described in details in the previous chapters.

From a viewpoint of practical applications, iron oxide-based fine particles and thin films are superior magnetic materials. The formers are utilized as excellent precursors for ferrite ceramics, magnetic recording medium and magnetic fluid. For example, γ-Fe_2O_3 crystal in acicular shape is the most available material for the magnetic recording tape. The thin films are used as several kinds of electronic and optoelectronic devices such as magnetic head material, magnetic Kerr effect device, optomagnetic recording medium and so forth.

In the present chapter, firstly, local structure and magnetic properties of fine particles precipitated from oxide glass are investigated. At the same time, the change of structure and magnetic properties during the crystallization process of the glass is examined so as to compare the structure of glass with that of crystals precipitated. Fe_2O_3-P_2O_5 and BaO-Fe_2O_3 glasses are chosen for the investigation because they are interesting from a viewpoint that the Fe^{3+}-O bond is most covalent in the former and is most ionic in the latter among the oxide glasses studied in this thesis, and significant amounts of Fe^{2+} ions coexist in the iron phosphate glasses but do not in the barium iron oxide glass (see Chapter 3). Secondly, Fe_3O_4 and γ-Fe_2O_3 thin films are prepared by utilizing the sol-gel method and their magnetic properties are studied.

6.1 Magnetic Properties of Fine Particles Precipitated from Oxide Glasses

6.1.1 Precipitates from Iron Phosphate Glass

The glass samples were prepared by using reagent-grade Fe_2O_3 and $FePO_4$ hydrate as starting materials. $FePO_4$ hydrate was kept in an electric furnace at 400 °C for several hours for the purpose of excluding water, and then it was mixed thoroughly with Fe_2O_3 in suitable proportions (Table 6.1) and sintered at 800-900 °C for 3 h in air. The resultant material was melted by heating it in an image furnace with a xenon lamp and the melt was rapidly quenched by falling it on a twin-roller rotating at 3000 rpm. The cooling rate of this method is about 10^5 K/s. The specimen obtained was a thin foil of about 20 μm thickness.

Table 6.1 Compositions of Fe_2O_3-P_2O_5 binary system and results of X-ray diffraction analysis

Composition (mol%) Fe_2O_3	P_2O_5	Results of X-ray diffraction
50	50	Amorphous
60	40	Amorphous
70	30	Amorphous
75	25	Amorphous
76	24	Amorphous
77	23	Fe_3O_4 precipitated
80	20	Fe_3O_4 precipitated

X-ray diffraction measurements with Cu Kα radiation were employed to determine whether the specimen was amorphous or not.

For the heat treatment experiments, the $70Fe_2O_3 \cdot 30P_2O_5$ glass was used. The reason for the choice of this composition will be described below. The heat treatment was carried out in an electric furnace at various temperatures from 220 to 710 °C for 5 h in air. The crystals precipitated in the heat treatment process were ascertained by X-ray diffraction analysis.

The samples thus obtained were subjected to ESR and Mössbauer effect measurements. The ESR measurements were made using a JEOL PE-2X spectrometer operating at X-band frequency (ν=9.4 GHz) with $1.0X10^{-4}$ T magnetic modulation width at room temperature. Reference signals of Mn^{2+} ions in MgO were used as the standards for the linewidth and effective g-value. The Mössbauer effect measurements were carried out at room temperature by using a 370 MBq ^{57}Co in metallic rhodium as the γ-ray source.

The compositions of the specimens prepared to select a glass having no trace of microcrystals are summarized in Table.6.1 along with the results of X-ray diffraction analysis. The X-ray diffraction pattern of the specimen exhibited an amorphous state until the concentration of Fe_2O_3 reached up to 76 mol% and showed the appearance of Fe_3O_4 when the content of Fe_2O_3 exceeded 77 mol%. However, in the X-ray diffraction patterns of $75Fe_2O_3 \cdot 25P_2O_5$ and $76Fe_2O_3 \cdot 24P_2O_5$ one very weak peak was noticed in the halo pattern. The existence of a minute amount of some microcrystalline phase was confirmed by employing ESR and Mössbauer effect measurements on the three specimens, $70Fe_2O_3 \cdot 30P_2O_5$,

$75Fe_2O_3 \cdot 25P_2O_5$ and $76Fe_2O_3 \cdot 24P_2O_5$.

ESR spectra of these specimens are shown in Fig.6.1. The linewidth and effective g-value obtained from these spectra are summarized in Table 6.2. As seen in Fig.6.1, the spectra of $75Fe_2O_3$ $25P_2O_5$ and $76Fe_2O_3$ $24P_2O_5$ were different from that of

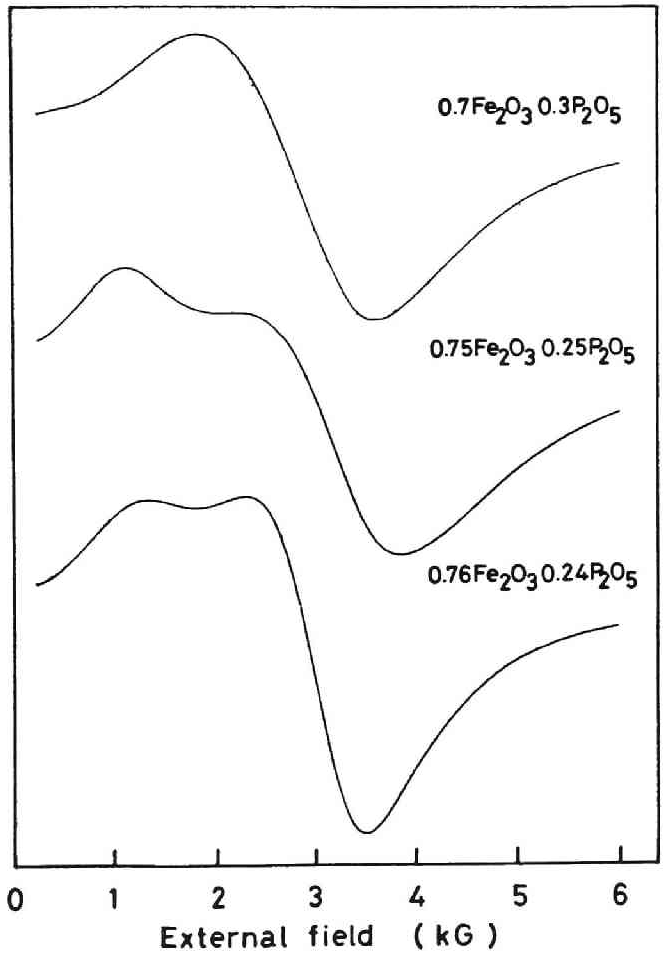

Fig.6.1 ESR spectra of $70Fe_2O_3 \cdot 30P_2O_5$, $75Fe_2O_3 \cdot 25P_2O_5$ and $76Fe_2O_3 \cdot 24P_2O_5$.

$70Fe_2O_3$ $30P_2O_5$. The latter consisted of only one broad peak centered at g=2.0, but the former spectra were composed of two peaks at g=4.3 and 2.0.

Table 6.3 shows the results of Mössbauer effect measurements. Fe^{2+} ions were detected in all the specimens. It is apparent from this table that the values of the quadrupole splitting of Fe^{3+} ions in both $75Fe_2O_3 \cdot 25P_2O_5$ and $76Fe_2O_3$ $24P_2O_5$ are significantly smaller than that in $70Fe_2O_3 \cdot 30P_2O_5$. This fact means that the symmetry of Fe^{3+} ion sites is more distorted in $70Fe_2O_3 \cdot 30P_2O_5$ than in $75Fe_2O_3 \cdot 25P_2O_5$ or $76Fe_2O_3 \cdot 24P_2O_5$, because the quadrupole splitting is a measure of the symmetry of the environment around an iron ion. This result of Mössbauer effect measurements indicates the precipitation of some microcrystals in both $75Fe_2O_3 \cdot 25P_2O_5$ and $76Fe_2O_3 \cdot 24P_2O_5$, while no

Table 6.2 ESR linewidth and effective g-value of $70Fe_2O_3 \cdot 30P_2O_5$, $75Fe_2O_3 \cdot 25P_2O_5$ and $76Fe_2O_3 \cdot 24P_2O_5$

Composition (mol%)		Line width	g-value
Fe_2O_3	P_2O_5	(G)	
70	30	1780	2.38
75	25	1610	2.18
		460	≃4.3
76	24	1230	2.18
		510	≃4.3

Table 6.3 Results of Mössbauer effect measurements of $70Fe_2O_3 \cdot 30P_2O_5$, $75Fe_2O_3 \cdot 25P_2O_5$ and $76Fe_2O_3 \cdot 24P_2O_5$

Composition (mol%)		Isomer shift (mm/sec)		Quadrupole splitting (mm/sec)	
Fe_2O_3	P_2O_5				
70	30	Fe^{3+}	0.43	Fe^{3+}	1.18
		Fe^{2+}	1.06	Fe^{2+}	2.45
75	25	Fe^{3+}	0.41	Fe^{3+}	0.79
		Fe^{2+}	1.22	Fe^{2+}	2.41
76	24	Fe^{3+}	0.36	Fe^{3+}	0.78
		Fe^{2+}	1.10	Fe^{2+}	2.26

crystalline phase existed in the $70Fe_2O_3 \cdot 30P_2O_5$ specimen. Thus, this composition was used for the following heat treatment experiments.

The kinds of crystals precipitated in the $70Fe_2O_3 \cdot 30P_2O_5$ specimen during the crystallization process are summarized in Table 6.4. As seen in this table, α-Fe_2O_3 precipitated at 420 °C, and at 500 °C Fe^{2+} ions formed iron metaphosphate $Fe(PO_3)_2$.

Figure 6.2 shows the ESR spectra of the quenched $70Fe_2O_3 \cdot 30P_2O_5$ glass and the specimen heat-treated at 710 °C. The former is apparently much broader than the latter. This fact indicates that the ligand field around Fe^{3+} fluctuates in $70Fe_2O_3 \cdot 30P_2O_5$ glass. Generally, spin Hamiltonian yielding the energy levels of spin is written as follows:

Table 6.4 Precipitated crystals through the crystallization process of $70Fe_2O_3 \cdot 30P_2O_5$ glass

Heat treatment temperature and time (°C, h)	Results of X-ray diffraction
300, 5	Amorphous
400, 5	Amorphous
420, 5	α-Fe_2O_3
500, 5	α-Fe_2O_3, $Fe(PO_3)_2$
600, 5	α-Fe_2O_3, $Fe(PO_3)_2$
710, 5	α-Fe_2O_3, $FePO_4$, Fe_3PO_7

$$\mathcal{H} = g\beta HS + D\{S_z^2 - S(S+1)/3\} + E(S_x^2 - S_y^2) + (a/6)\{S_x^4 + S_y^4 + S_z^4 - \frac{1}{5}S(S+1)(3S^2+3S-1)\} + H_{ss} + H_{hf} + H_Q. \quad (6.1)$$

The first term is Zeeman energy and the second and the third terms are ligand field energies. The fourth term is fourth dimensional one of spin peculiar to Fe^{3+}, spin quantum number of which is larger than 2. H_{ss}, H_{hf} and H_Q correspond to Hamiltonian representing spin-spin interaction, hyperfine interaction and quadrupole interaction of nucleus, respectively. If there exists

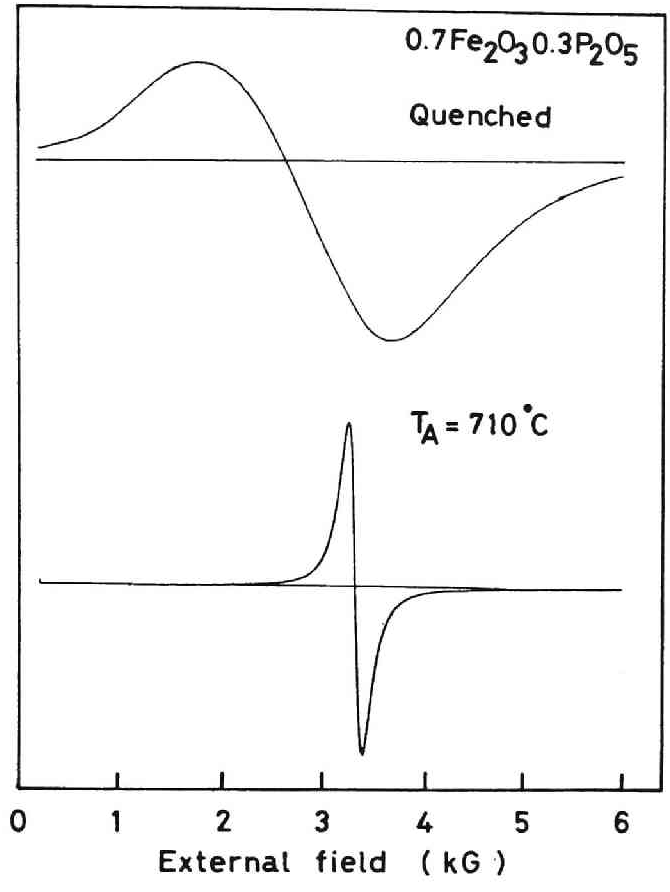

Fig.6.2 ESR spectra of $70Fe_2O_3 \cdot 30P_2O_5$ quenched glass and heat-treated at 710 °C. T_A means the heat treatment temperature.

a variation of ligand fields, the crystal field parameters D and E are not uniform but fluctuate. So, Hamiltonian must be affected by the fluctuation, and the eigenvalue of Hamiltonian, that is the energy level of spin, should have a distribution. Therefore, the ESR spectrum of $70Fe_2O_3 \cdot 30P_2O_5$ glass is expected to exhibit a

very broad tail as observed in Fig.6.2.

The change in linewidth of ESR spectra appearing during the heat treatment process is shown in Fig.6.3, along with the change of effective g-value. The linewidth started to decrease at about 300 °C and took a minimum at about 340 °C, beyond which it increased. When the heat treatment temperature exceeded 500 °C, it decreased again rapidly. A similar tendency was seen on the change of effective g-value.

The linewidth of the quenched $70Fe_2O_3$ $30P_2O_5$ glass was 1780 G, which is much larger than that of the specimen heat-treated at 710 °C (160 G). The latter is attributable to the parasitic ferromagnetism of α-Fe_2O_3,[6),7)] which causes a strong superexchange interaction at room temperature. According to the Anderson-Weiss theory,[8)] the observed linewidth is represented as follows:

$$\Delta H = \frac{(10/3)(\Delta H_p)^2 + (\Delta H_H)^2}{\Delta H_e} \quad , \qquad (6.2)$$

where ΔH_p, ΔH_e and ΔH_H represent the linewidth due to dipole-dipole interaction, superexchange interaction and fine structure field, respectively. Therefore the linewidth of the specimen heat-treated at 710 °C should become very narrow due to the precipitation of α-Fe_2O_3. On the other hand, dipole-dipole interaction governs the magnetic interaction between iron ions in the quenched glass. Consequently, the linewidth of the quenched glass becomes broadened as indicated in Eq.(6.2).

A complicated change of linewidth with heat treatment temperature shown in Fig.6.3 requires another mechanism of line narrowing than the superexchange interaction in the precipitated

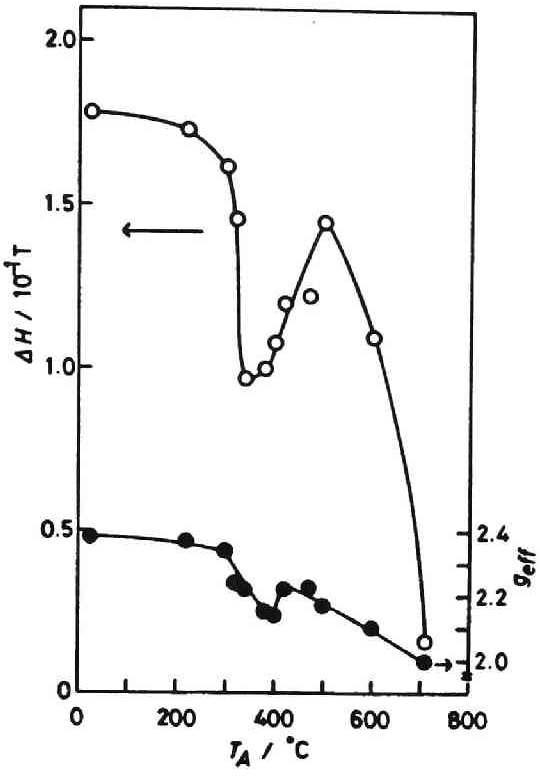

Fig.6.3 Change of linewidth and effective g-value of ESR spectrum through the crystallization process of $70Fe_2O_3$ $30P_2O_5$ glass.

α-Fe_2O_3. According to Néel,[9] α-Fe_2O_3 is also known as a compound which shows superparamagnetism when the size of the particles is sufficiently small.

The smallness of the size of α-Fe_2O_3 precipitated in this temperature range can be demonstrated by the result of Mössbauer effect measurements. The Mössbauer spectrum of the specimen heat-treated at 500 °C is drawn in Fig.6.4 along with the spectra

of the quenched glass as well as the specimen heat-treated at 710 °C. Although α-Fe_2O_3 has already precipitated in the specimen heat-treated at 500 °C as ascertained by X-ray diffraction analysis shown in Table 6.4, the sextet peak due to the internal field in α-Fe_2O_3 did not appear in this specimen. This fact indicates that α-Fe_2O_3 in this specimen is small and shows superparamag-

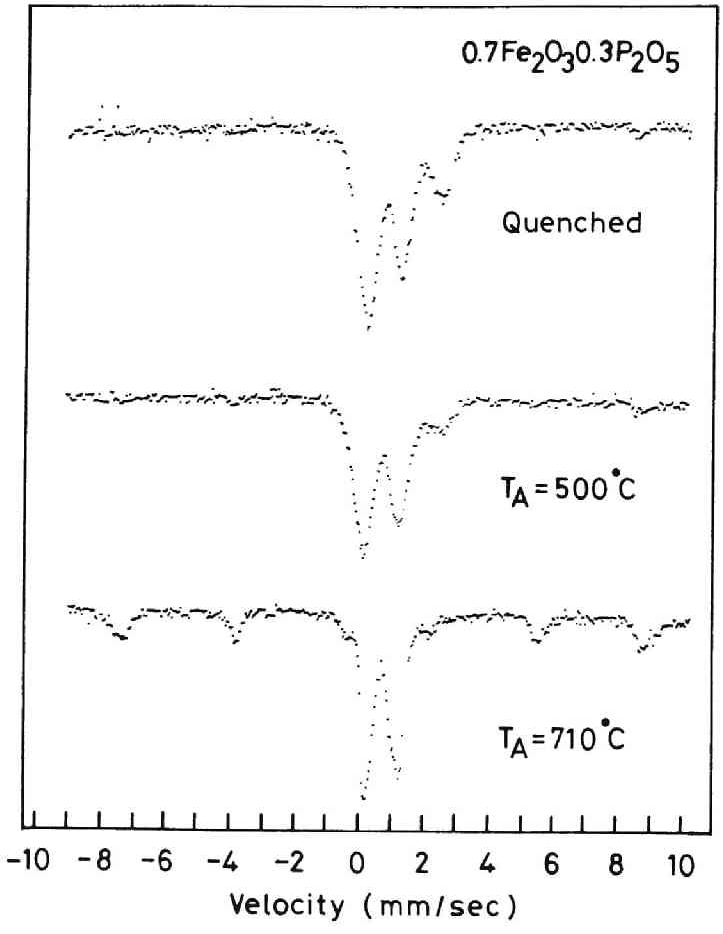

Fig.6.4 Mössbauer spectra of quenched, heat-treated at 500 °C and heat-treated at 710 °C $70Fe_2O_3 \cdot 30P_2O_5$ glass.

netism. The existence of superparamagnetism can be seen in the ESR spectrum of the specimen heat-treated at 400 °C shown in Fig.6.5. The shoulder at about 1800 G is attributable to Fe^{3+} ions which still exist in the glassy state in this specimen, and the peak at the higher field is due to Fe^{3+} ions in the superparamagnetic α-Fe_2O_3 particle. This ESR spectrum is very similar to that of ultrafine particles of Fe_3O_4 in various liquid observed by Sharma and Waldner.[10)]

The line narrowing due to superparamagnetism was observed by Sharma and Waldner,[10)] who investigated ultrafine particles of

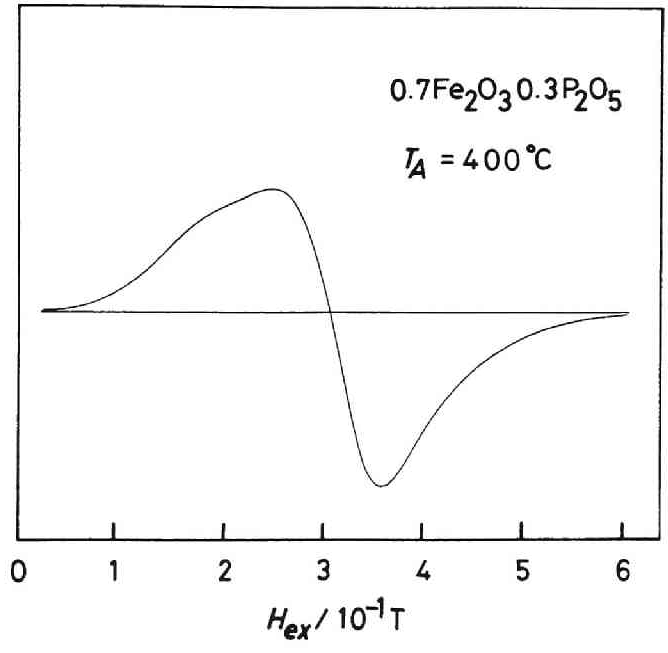

Fig.6.5 ESR spectrum of $70Fe_2O_3 \cdot 30P_2O_5$ glass heat-treated at 400 °C

Fe_3O_4 in various ferrofluids by means of X-band ESR measurements. They defined the superparamagnetic narrowing factor f as follows:

$$f = \tau_{sp}/\tau_L = M_s V/\gamma kT\tau_L, \quad (6.3)$$

where τ_{sp} and τ_L are the superparamagnetic relaxation time and Larmor precession time, respectively, M_s is the saturation magnetization, V is the volume of the superparamagnetic particle, and γ is the gyromagnetic ratio. The proportional relation between the superparamagnetic narrowing linewidth and the volume of the particle was demonstrated by the data measured by Aharoni and Litt.[11] The increase in linewidth with increasing heat treatment temperature from 340 to 500 °C observed in the present study is attributable to the growth of α-Fe_2O_3 crystallites.

When the heat treatment temperature exceeded 500 °C, the linewidth decreased sharply. As described above, this narrowing is assigned to superexchange interaction owing to Fe^{3+} in α-Fe_2O_3 particles, the size of which is large enough not to show superparamagnetism. This interpretation agrees with the Mössbauer spectrum of the specimen heat-treated at 710 °C in Fig.6.4, which exhibited internal field lines. The internal field of α-Fe_2O_3 in this specimen is estimated to be 506 kOe.

As for the effective g-value, it was 2.00 for the specimen heat-treated at 710 °C. This value is reasonable for Fe^{3+} ions because the spin state of Fe^{3+} is $^6S_{5/2}$ and its orbital angular momentum is zero. The effective g-value of the quenched $70Fe_2O_3$ $30P_2O_5$ glass was 2.38, larger than 2.00. This deviation from g=2.00 is ascribed to the contribution of orbital angular momentum to the g-value. The fraction of the orbital angular momentum

to the spin angular momentum is represented by the following relation:[12),13)]

$$\varepsilon = g/2 - 1. \qquad (6.4)$$

In the case of $70Fe_2O_3 \cdot 30P_2O_5$ glass, $\varepsilon = 0.19$. As described above, however, the orbital angular momentum quantum number of Fe^{3+} is zero, so that ε should be zero. The reason why ε was not zero in the $70Fe_2O_3 \cdot 30P_2O_5$ glass is not clear at present, but might be related to the existence of Fe^{2+} ions in this glass. Fe^{2+} is known as an ion which is magnetically extremely anisotropic. The spin state of Fe^{2+} is S=2, L=2, indicating that the orbital angular momentum remains. In a general crystal such as an ionic crystal, this orbital angular momentum is quenched because of strong orbital-lattice interaction. Since there is a distribution of ligand field in this glass as described above, it is predictable that quenching of orbital angular momentum is not complete. Moreover, it may be presumed that there exists a resonance structure in this glass like the next one:

$$Fe^{2+}\text{-}O^{2-}\text{-}Fe^{3+} \rightleftharpoons Fe^{3+}\text{-}O^{2-}\text{-}Fe^{2+}. \qquad (6.5)$$

It is considered that Fe^{2+} has an effect on Fe^{3+} by way of such a resonance. As a result, the effective g-value becomes significantly larger than 2.00.

The change in linewidth of Mössbauer spectra appearing during the heat treatment process is shown in Fig.6.6. The linewidth of Fe^{3+} did not change until the heat treatment temperature reached up to 300 °C and decreased monotonically when the heat treatment temperature exceeded 400 °C, at which α-Fe_2O_3 microcrystals started to precipitate according to the X-ray dif-

fraction measurements. The linewidth of Fe^{2+} also decreased at 400 °C. This demonstrates a distribution of electric field gradient around both Fe^{3+} and Fe^{2+} ions in this glass. Eibschütz et al.[14] studied vitreous yttrium iron garnet by Mössbauer effect measurements and succeeded in fitting the computed absorption line to the experimental spectrum by assuming an asymmetric non-Gaussian distribution of electric field gradient. Their method has been already applied to the examination of the ligand fields around iron in Bi_2O_3-Fe_2O_3 glasses in the present thesis as described in Chapter 3. The existence of distribution of electric field gradient, that is a fluctuation of ligand field around Fe^{3+}

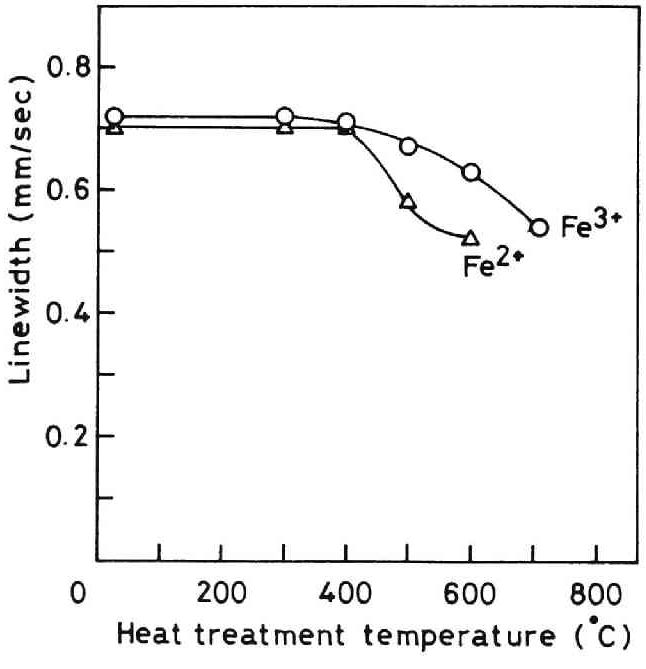

Fig.6.6 Change of linewidth of Mössbauer spectra through the crystallization process.

ions, in the $70Fe_2O_3 \cdot 30P_2O_5$ glass is ascertained by the shape of ESR spectra as mentioned above.

The change of isomer shift is shown in Fig.6.7. The isomer shift of Fe^{3+} in the quenched $70Fe_2O_3 \cdot 30P_2O_5$ glass was 0.43 mm/s when referred to pure iron. The isomer shift of Fe^{3+} decreased slowly through the crystallization process. On the contrary, the isomer shift of Fe^{2+} increased with increasing heat treatment temperature.

The change of quadrupole splitting, which is a measure of symmetry of the shape of electron clouds around an iron ion, is shown in Fig.6.8. The quadrupole splitting of Fe^{2+} decreased at first and then increased as $Fe(PO_3)_2$ crystal grew. This change corresponds to the change of isomer shift.

The isomer shift of Fe^{3+} in the quenched $70Fe_2O_3 \cdot 30P_2O_5$ glass (0.43 mm/s) shows that Fe^{3+} ions in this glass are coordinated by six O^{2-} ions as indicated by Kurkjian and Sigety.[15] The change of isomer shift reflects the change in distance between an iron ion and an O^{2-} ion.[16] As discussed in detail in Chapter 3, a smaller value of isomer shift shows a higher density of 4s-electrons around an iron ion, indicating the shorter distance between an iron ion and an O^{2-} ion. Therefore, the decrease of isomer shift of Fe^{3+} exhibits the decrease of the distance between Fe^{3+} and O^{2-} ions through the crystallization process and the increase of isomer shift of Fe^{2+} shows that the distance between Fe^{2+} and O^{2-} ions in $70Fe_2O_3 \cdot 30P_2O_5$ glass is smaller than that in $Fe(PO_3)_2$ polycrystal.

The quadrupole splitting of Fe^{3+} directly reflects the geo-

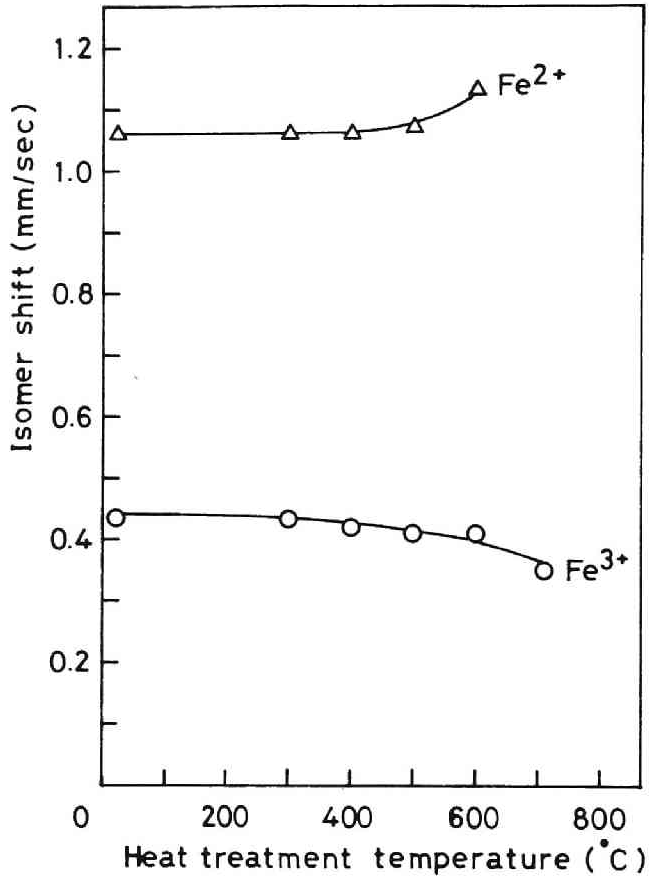

Fig.6.7 Change of isomer shift of Fe^{3+} and Fe^{2+} through the crystallization process.

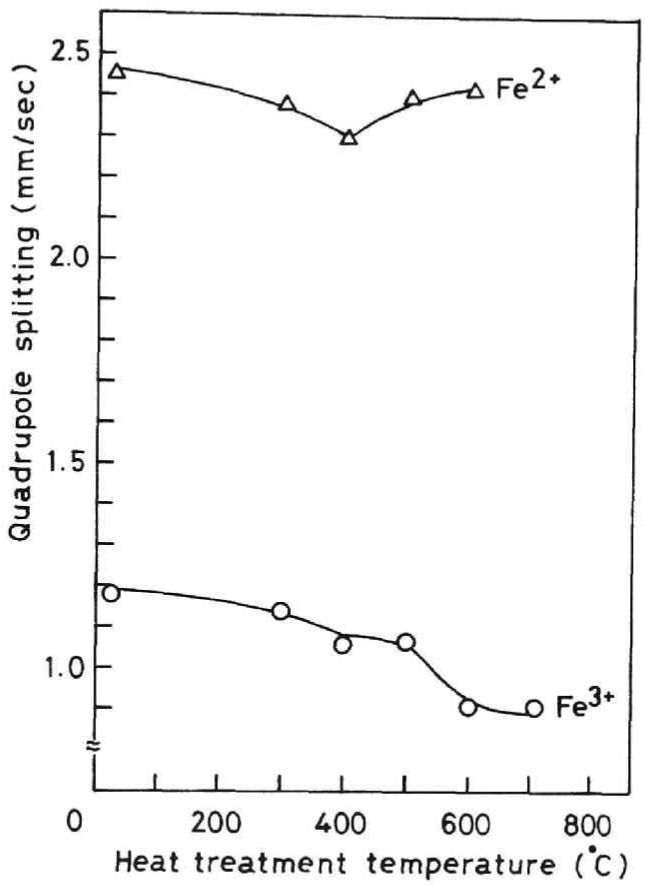

Fig.6.8 Change of quadrupole splitting of Fe^{3+} and Fe^{2+} through the crystallization process.

metrical symmetry of the coordination state of O^{2-} ions, because the 3d-orbitals of Fe^{3+} is hall filled and the electric field gradient caused by 3d-electrons is tetrahedrally symmetrical. Hence, the decrease of quadrupole splitting of Fe^{3+} through the crystallization process reveals that the coordination state of O^{2-} ions around Fe^{3+} in $70Fe_2O_3 \cdot 30P_2O_5$ glass is more asymmetrical than that in α-Fe_2O_3.

The increase of isomer shift of Fe^{2+} after $Fe(PO_3)_2$ precipitated may be explained by the decrease of 4s-electron density of Fe^{2+} as described above. Because of the decrease of 4s-electron density, the nucleus of iron in Fe^{2+} interacts more easily with 3d-electrons. Since five 3d-orbitals of Fe^{2+} is filled with six electrons, the electric field gradient induced by 3d-electrons of Fe^{2+} is significantly asymmetrical. So, the quadrupole splitting of Fe^{2+} increases with decreasing 4s-electron density as $Fe(PO_3)_2$ crystals grow.

6.1.2 Precipitates from Barium Iron Oxide Glass

It has been revealed experimentally that the compositions in the vicinity of an eutectic point can be converted to glassy states more easily than the other compositions when the rapidly quenching method is applied. For BaO-Fe_2O_3 system, attempts were made to prepare glass by using gun method[17] and single-roller method[18] thus far and it was reported that the glass-forming region lies in the range of 30-60 mol% Fe_2O_3 for the gun method and 38-45 and 55-70 mol% Fe_2O_3 for the single-roller method, respectively. Namely, the glass-forming region extends around the eutectic points in the phase diagram of BaO-Fe_2O_3 system.[19]

Thus, in the present study, an attempt was made to prepare the glass with the compositions around the eutectic points by using the twin-roller quenching method.

Reagent-grade $BaCO_3$ and Fe_2O_3 were used as starting materials for the preparation of glass. They were mixed thoroughly in prescribed compositions (Fig.6.9). The mixture was pressed under hydrostatic pressure and sintered at 900 °C for 3 h in air. The sintered body thus obtained was melted at about 2000 °C in air by using an image furnace with a xenon lamp. The melt was quenched by dropping on a twin-roller made of stainless steel rotating at 3000 rpm. Thus, a specimen of about 20 μm thickness was obtained. X-ray diffraction analysis was carried out in order to ascertain whether the specimen was amorphous or not.

The glass-forming region obtained is shown in Fig.6.9. As clearly seen in this figure, the composition $60BaO \cdot 40Fe_2O_3$ only yields a stable glass: specimens with the other compositions include crystalline phases. In particular, although X-ray diffraction pattern of the specimens with compositions around 60 mol% Fe_2O_3 shows halo pattern as a whole, a slight amount of

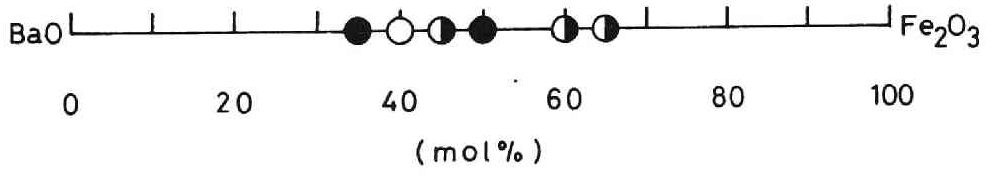

Fig.6.9 Glass-forming region of $BaO-Fe_2O_3$ system by twin-roller method. ○: glass, ●: crystal, ◑: glass+crystal

crystalline $BaFe_{12}O_{19}$ was detected. The narrower glass-forming region obtained by the present twin-roller method compared with those by the previous gun method and single-roller method is attributable to the slower cooling rate of the present method. Thus, the $60BaO \cdot 40Fe_2O_3$ glass was subjected to the subsequent experiments of heat treatment.

The heat treatment of the glass was performed at 300 to 700 °C for 5 h in air. The crystalline phase precipitated was identified by means of the X-ray diffraction analysis. The heat-treated specimens as well as the quenched glass were then sub-

Table 6.5 Precipitated crystals through the crystallization process of $60BaO \cdot 40Fe_2O_3$ glass

Heat treatment temperature and time (°C, h)	Results of X-ray diffraction
300, 5	Amorphous
400, 5	Amorphous
440, 5	$BaFe_2O_4$, $Ba_2Fe_2O_5$
500, 5	$BaFe_2O_4$, $Ba_2Fe_2O_5$
600, 5	$BaFe_2O_4$, $Ba_2Fe_2O_5$
700, 5	$BaFe_2O_4$, $Ba_2Fe_2O_5$

jected to the ESR and Mössbauer effect measurements with the same conditions as described in section 6.1.1.

Table 6.5 shows the results of X-ray diffraction analysis performed on the heat-treated specimens. The specimens heat-treated at 300 °C and 400 °C do not contain any crystalline phases, that is they are amorphous. When the heat treatment temperature was raised up to 440 °C, $BaFe_2O_4$ and $Ba_2Fe_2O_5$ crystals were precipitated from the glass. Only these two crystalline phases were detected in the specimens heat-treated at higher temperatures than 440 °C. The $BaFe_2O_4$ is known as antiferromagnetic crystal with Néel temperature of 880 K.[20]

The Mössbauer spectra of several specimens are shown in Fig.6.10. The isomer shift value of the as-quenched glass is 0.22 mm/s as described in Chapter 4, which is in agreement with the value for the glass with the same composition prepared by the single-roller method.[18] However, the quadrupole splitting of the present glass, 0.81 mm/s, is somewhat smaller than that of the glass prepared by the single-roller method, i.e. 0.91 mm/s. This discrepancy may arise from the difference in the cooling rate of these two methods. For the present twin-roller quenching method, the cooling rate of which is slower as mentioned above, the structural relaxation of the glass proceeds more readily during the quenching process. As a result, the structure of FeO_4 units approaches the structure in the crystalline states and becomes more symmetrical, resulting in the smaller value of quadrupole splitting. These facts indicate that the bond angle of $O\text{-}Fe^{3+}\text{-}O$ is more changeable than the bond length of $Fe^{3+}\text{-}O$ in the

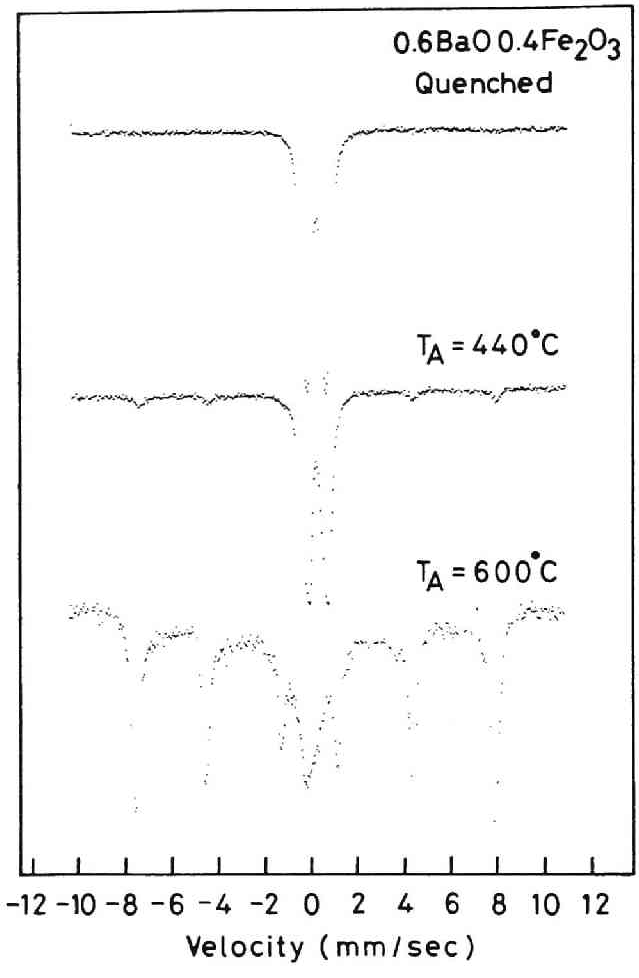

Fig.6.10 Mössbauer spectra of quenched, heat-treated at 440 °C and heat-treated at 600 °C $60BaO \cdot 40Fe_2O_3$ glass. T_A means the heat treatment temperature.

glassy state.

Both the isomer shift and the quadrupole splitting decrease with increasing the heat treatment temperature as shown in Figs. 6.11 and 6.12, respectively, where the open circles are estimated from the paramagnetic peak appearing in the central position of the spectra and the solid circles are estimated from the splitted peaks due to hyperfine field. Especially, sharp decrease is observable at the heat treatment temperature wherein the crystallization takes place. These facts indicate that the distance of Fe^{3+}-O is shorter and the FeO_4 tetrahedron is more symmetric in the crystalline state. The extremely small value of the isomer shift obtained from the paramagnetic peak for the specimens heat-treated at 600 °C and 700 °C may suggest the coexistence of Fe^{4+}. Therefore, it is plausible that $BaFeO_{3-\delta}$ or $BaFeO_3$ precipitates in addition to $Ba_2Fe_2O_5$ in these specimens.

A close look at Fig.6.12 reveals that the quadrupole splitting of $BaFe_2O_4$ decreases monotonically with increase of the heat treatment temperature (solid circles). Since the increase of the heat treatment temperature means the growth of $BaFe_2O_4$ crystal, this tendency shown in Fig.6.12 indicates that the quadrupole splitting is larger for the $BaFe_2O_4$ particle with smaller size. A large part of Fe^{3+} ions are present at the surface in small particle and it is expected that the FeO_4 tetrahedra are more asymmetric at the surface than in the interior. Hence, the quadrupole splitting value becomes larger as the size of the particle is decreased. In fact, the specimen heat-treated at 700 °C gives the quadrupole splitting of 0.25 mm/s which was the same value as

that reported for bulk $BaFe_2O_4$ crystal.[20)]

Figure 6.13 shows the variation of the hyperfine field due to $BaFe_2O_4$ with the heat treatment temperature. The hyperfine field increases with increasing the heat treatment temperature and is saturated to 474 kOe at 600 °C. This value is in agreement with that of the bulk $BaFe_2O_4$.[20)] The smaller value of hyperfine field observed for the specimen heat-treated at lower temperature is attributable to the smaller size of $BaFe_2O_4$ par-

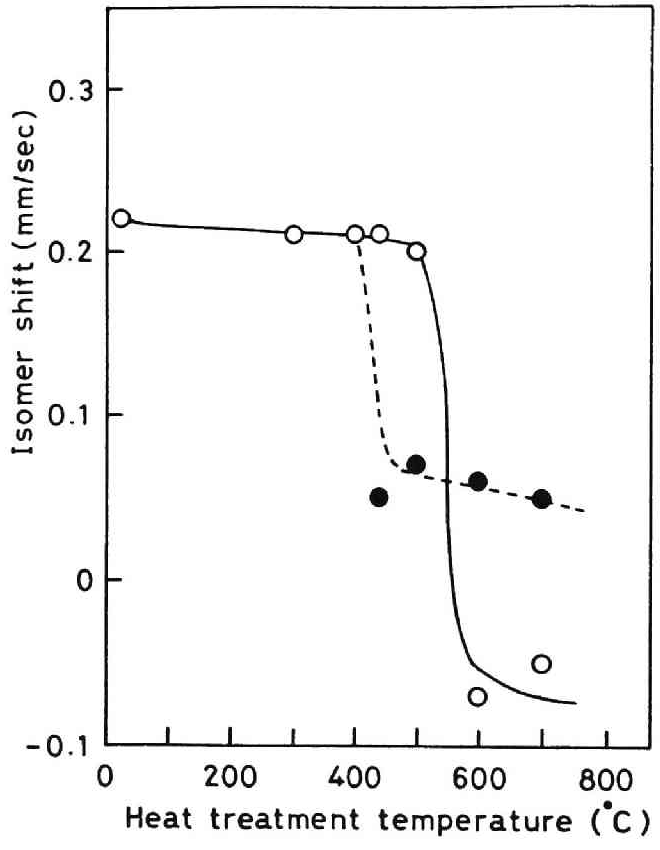

Fig.6.11 Change of isomer shift through the crystallization process.

ticle. A similar phenomenon was observed for the crystallization process of $NiFe_2O_4$ from silicate glass.[16] Further, Kündig et al.[21] carried out Mössbauer effect measurements on α-Fe_2O_3 particles with different sizes at room temperature and revealed that the hyperfine field increased with increasing the size of particle. The superparamagnetic effect is one of the reasons why

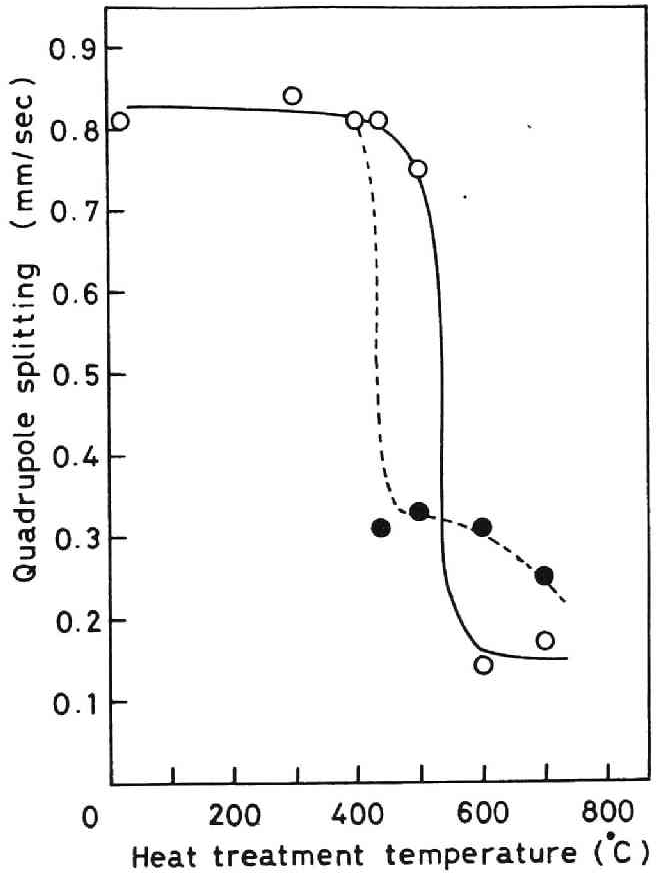

Fig.6.12 Change of quadrupole splitting through the crystallization process.

the particle with smaller size gives the smaller value of hyperfine field. Another is the effect of surface magnetism. As revealed for α-Fe_2O_3, γ-Fe_2O_3 and Fe_3O_4,[1)-4)] the Fe^{3+} ions at the surface yield lower hyperfine fields than those in the inside due to the relatively random configuration of Fe^{3+} ions at the surface. It is thought that in the present case, these two effects lead to the smaller value of hyperfine field for $BaFe_2O_4$ precipitated at lower heat treatment temperature.

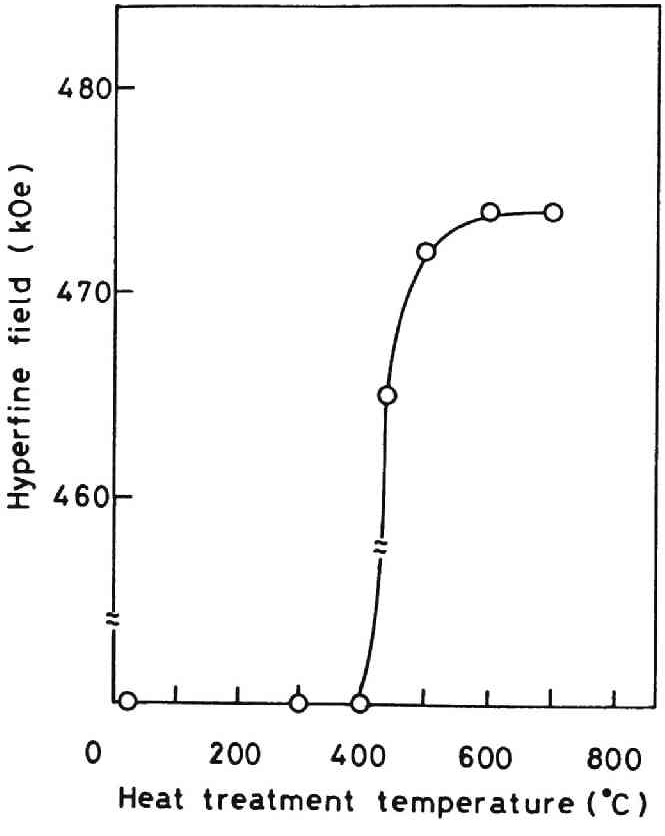

Fig.6.13 Change of hyperfine field through the crystallization process.

ESR spectra for the quenched glass and the heat-treated specimens are shown in Fig.6.14. The resonance signal at g=2.0 is observed in the spectra of the quenched glass and the specimen heat-treated at 440 °C. This signal is attributable to the spin pairs of Fe^{3+}-O-Fe^{3+}. The specimen heat-treated at 600 °C gives

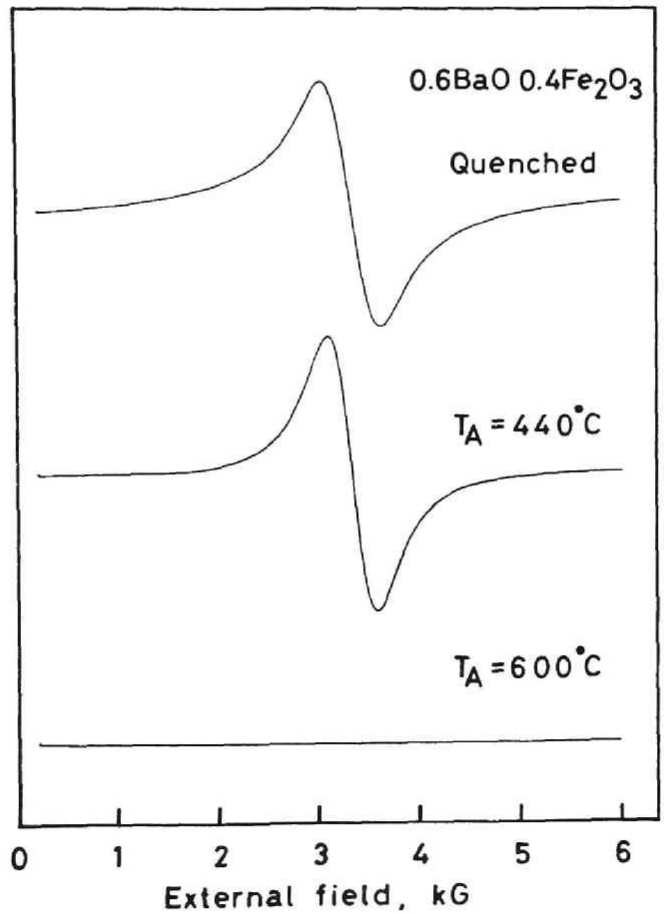

Fig.6.14 ESR spectra of quenched, heat-treated at 440 °C and heat-treated at 600 °C $60BaO \cdot 40Fe_2O_3$ glass.

no ESR resonance signals because this specimen contains large amounts of antiferromagnetic crystal $BaFe_2O_4$.

The variations of ESR linewidth and effective g-value with the heat treatment temperature are shown in Fig.6.15. The effective g-value is independent of the heat treatment temperature and is approximately equal to 2.00. This is a reasonable value for Fe^{3+} whose orbital angular momentum is zero. On the other hand, the linewidth decreases monotonically with the increase of heat

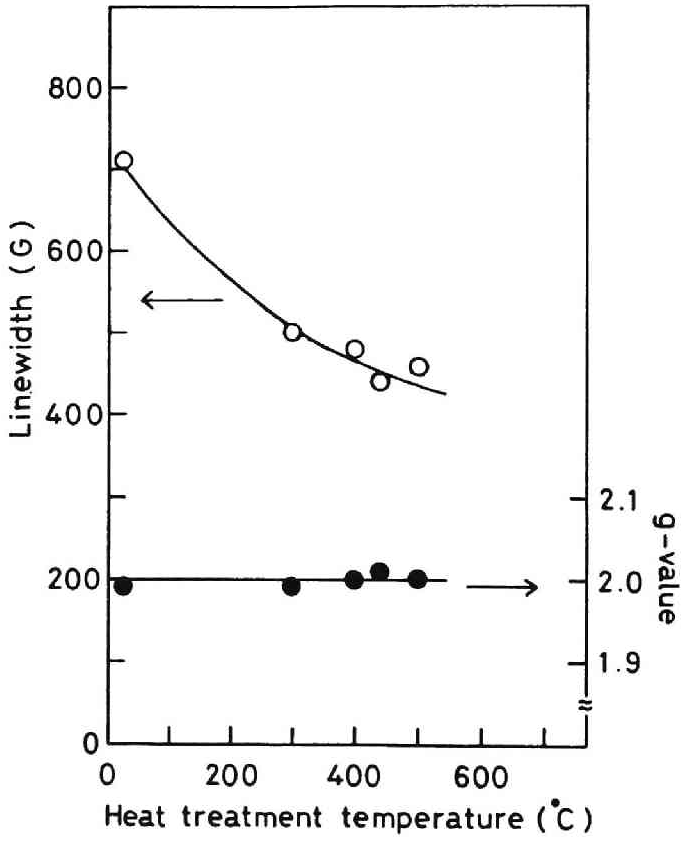

Fig.6.15 Change of ESR linewidth and effective g-value through the crystallization process.

treatment temperature. According to Eq.(6.2), the decrease of the linewidth is explainable in terms of the decrease of dipole-dipole interaction and the increase of superexchange interaction. These phenomena result from the thermal relaxation of glass structure because no crystalline phases are precipitated in this heat treatment temperature region. The slight decrease of Fe^{3+}-O bond length with increasing the heat treatment temperature as seen from Fig.6.11 may result in the increase of superexchange interaction among Fe^{3+} ions. Further, change of Fe^{3+}-O-Fe^{3+} bond angle is also a possible cause for the variation of dipole-dipole interaction and superexchange interaction during the thermal relaxation. It is well known that the Fe^{3+}-O-Fe^{3+} with bond angle of 180° produces stronger superexchange interaction than that with bond angle of 90°. Moreover, the variation of the separation between Fe^{3+} ions accompanied by the change of the Fe^{3+}-O-Fe^{3+} bond angle leads to the variation of dipole-dipole interaction. It is estimated by using the next Van Vleck's equation:

$$\Delta H_p \approx \sqrt{S(S+1)}r^{-3} \qquad (6.6)$$

that the dipole-dipole interaction between Fe^{3+} ions with the Fe^{3+}-O-Fe^{3+} bond angle of 90° is about 2.8 times larger than that in the case of 180° bond angle. It is concluded that the change of Fe^{3+}-O bond length and Fe^{3+}-O-Fe^{3+} bond angle due to the thermal relaxation of the glass structure brings about the variation of the ESR linewidth.

6.2 Magnetic Properties of Ferrite Thin Films Prepared from Gel

Ferrite-based magnetic thin films are important materials for practical applications. They are effectively utilized as magnetic core materials with low iron loss, optomagnetic devices, bubble memory devices, vertical recording magnetic materials and so on. They are also interesting substances from the viewpoint of surface magnetism. The surface magnetic state of thin films as well as ultrafine particles of α-Fe_2O_3, γ-Fe_2O_3 and Fe_3O_4 has been investigated extensively.[1)-5)]

As for the preparation of such thin films, many investigations have been made by using sputtering,[23)] APS,[24)] OMCVD,[25)] LPE[26)] and ferrite-plating,[27)] so far. However, little attention has been paid to the preparation of the magnetic thin film by the sol-gel method except for the recent work by Kordas et al.[28),29)] and Chen et al.[30)] In particular, as far as we know, the preparation and magnetic properties of sol-gel-derived Fe_3O_4 and γ-Fe_2O_3 thin films have not yet been reported. From the technological viewpoint, the sol-gel method possesses several advantageous points such that it enables us to make a thin film with very large area and any shape, and it does not require too high temperature and any vacuum. In the present investigation, an attempt was made to prepare Fe_3O_4 and γ-Fe_2O_3 thin films by using the sol-gel method. The characterization of the Fe_3O_4 and γ-Fe_2O_3 thin films prepared was carried out by means of X-ray diffraction, ESR and magnetization measurements.

The dip-coating method[31)] was used for the preparation of the thin film. The flow chart of the preparation is shown in Fig.6.16. The sol solution for the dip-coating was prepared by

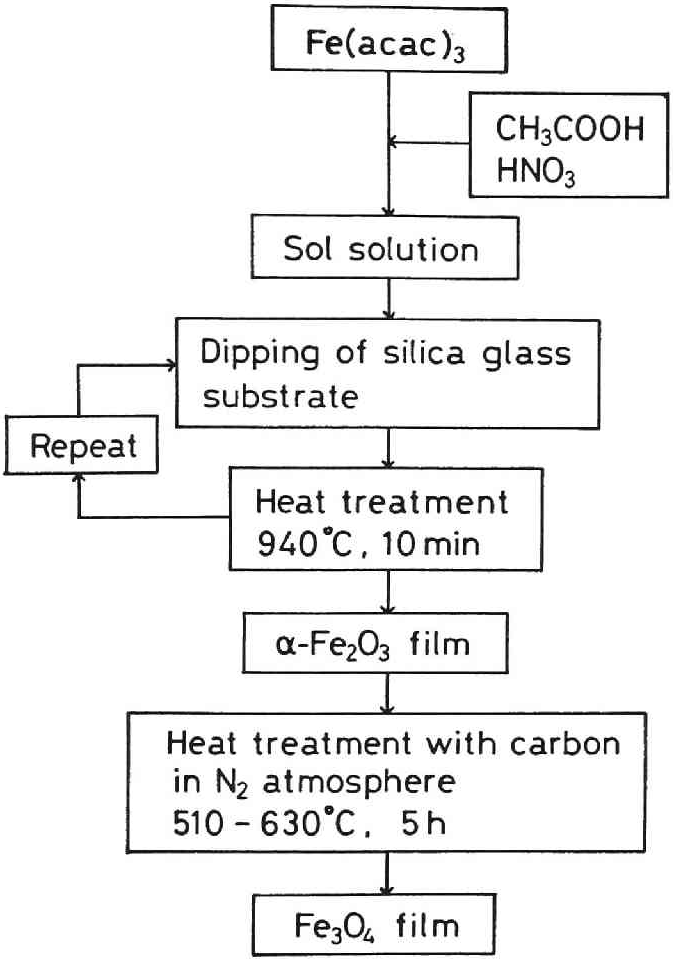

Fig.6.16 Flow chart for the preparation of Fe_3O_4 thin film by the sol-gel method.

using tris(acetylacetonato)iron(III), $Fe(acac)_3$, as a starting reagent. 14.13 g (0.04 mol) of $Fe(acac)_3$ was added into a mixture of 68.7 ml CH_3COOH as a solvent and 7.49 ml concentrated HNO_3(aq) (61 wt%) as a catalyst under vigorous stirring. The molar ratios of CH_3COOH and HNO_3 to $Fe(acac)_3$ were 30.0 and 2.5, respectively. Solvents other than acetic acid were slightly inferior. For instance, the use of ethanol or acetylacetone made wetting of the substrate with the solution worse. The mixed solution became a clear sol solution upon complete dissolution of $Fe(acac)_3$ after stirring for 4 h. All of these procedures were performed at room temperature.

The iron oxide sol solution was applied to a silica glass substrate, the surface of which was cleaned beforehand with acetone, by dipping the substrate into the above-mentioned sol solution and pulling it up at a constant speed (about 0.6 mm/s). The coating film thus obtained was heat-treated at 940 °C for 10 min in air. After ten repetitions of this process, the thickness of the film became 0.2 μm, as determined by the stylus-type surface profilometer. X-ray diffraction measurements on the film with Co Kα radiation indicated the precipitation of α-Fe_2O_3. The crystallite size was estimated to be about 50 nm.

For the purpose of being converted to Fe_3O_4 thin film, the α-Fe_2O_3 thin film obtained was embedded in carbon powders so that the surface of the film was thoroughly covered with carbon and heat-treated at several temperatures from 490 to 690 °C for 5 h in N_2 atmosphere. The resultant thin film was subjected to the X-ray diffraction analysis for the identification of precipitates. The Fe_3O_4 thin film thus prepared was examined by means

of ESR and magnetization measurements to obtain information about the magnetic properties. The ESR measurements were carried out at room temperature using a Varian E-Line spectrometer operating at X-band frequency. The silica glass coated with Fe_3O_4 film was cut into a suitable size (3X3X20 mm^3) and was subjected to the measurements. It was set at various angles between the surface of the film and the direction of the external field in order to examine the direction of the axis of easy magnetization and the strength of magnetization of the film. The magnetization measurements were carried out at room temperature using a vibrating-sample magnetometer. The surface area of the sample was 3X6 mm^2 and the external field was applied parallel to the surface.

The γ-Fe_2O_3 was prepared by heating the Fe_3O_4 thin film at 300 °C for 1 h in air according to the conventional method for the preparation of γ-Fe_2O_3 particle. The resultant γ-Fe_2O_3 thin film was subjected to the ESR measurements. The sample was set so that the external field was applied perpendicular or parallel to the surface of the film.

Fig.6.17 shows the results of the X-ray diffraction analysis of the iron oxide thin films heat-treated at various temperatures. When the heat treatment temperature is lower than 510 °C, the conversion to Fe_3O_4 does not occur and α-Fe_2O_3 still remains. The heat treatment at 510 to 630 °C gives Fe_3O_4 thin films. The diffraction pattern of the specimen heat-treated above 630 °C shows a peak around $2\theta=25°$ which is not attributable to either Fe_3O_4 or α-Fe_2O_3. Accordingly, it may be said that a suitable heat treatment temperature for the preparation of

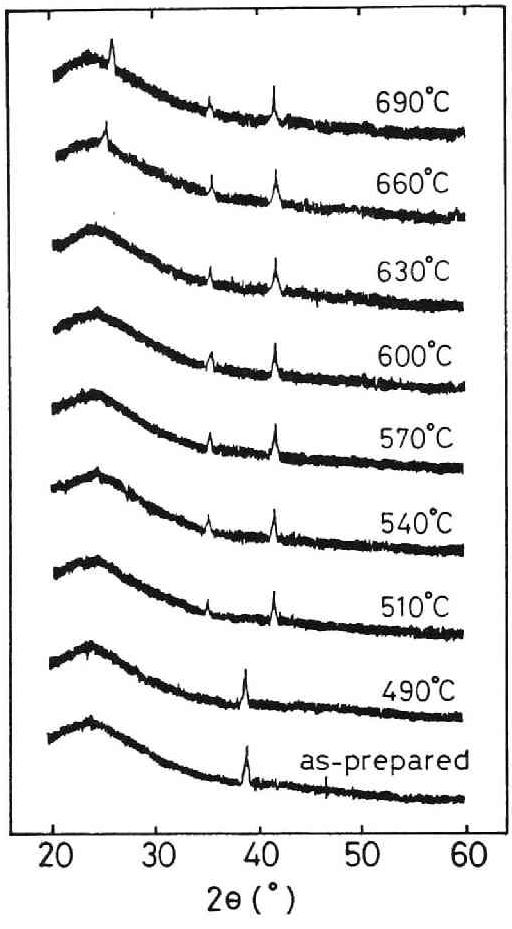

Fig.6.17 X-ray diffraction patterns of the thin films heat-treated at several temperatures for 5 h in N_2 atmosphere. The specimens were brought into contact with carbon powders during the heat treatment.

Fe_3O_4 thin film lies between 510 and 630 °C. The crystallite size of the Fe_3O_4 in the thin film obtained is estimated to be about 50 nm from the half-height width of the (311) diffraction line. The crystallite size was independent of the heat treatment temperature. No preferred orientation of the crystal was observed in the specimens.

Figs.6.18a and b show the ESR spectra of a specimen heat-treated at 580 °C with the direction of the external field per-

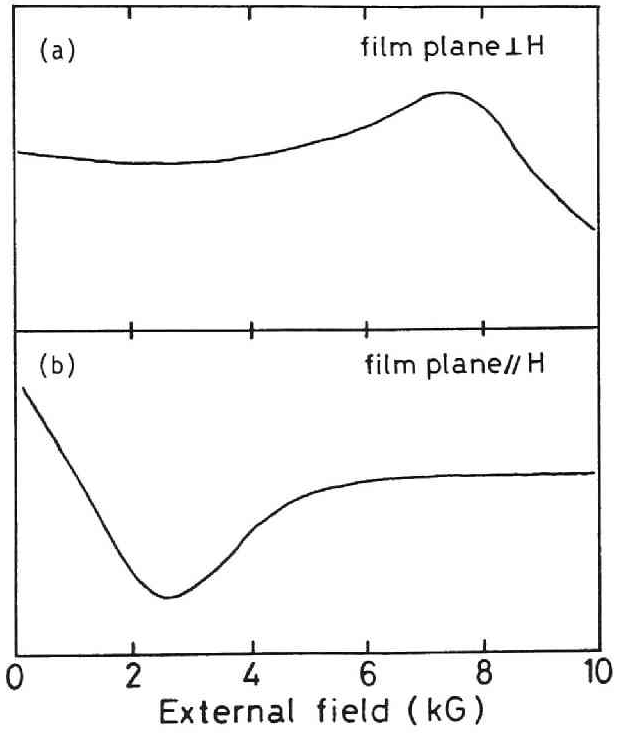

Fig.6.18 ESR spectra of the Fe_3O_4 thin film with the direction of external field being perpendicular and horizontal to the surface of the thin film, respectively.

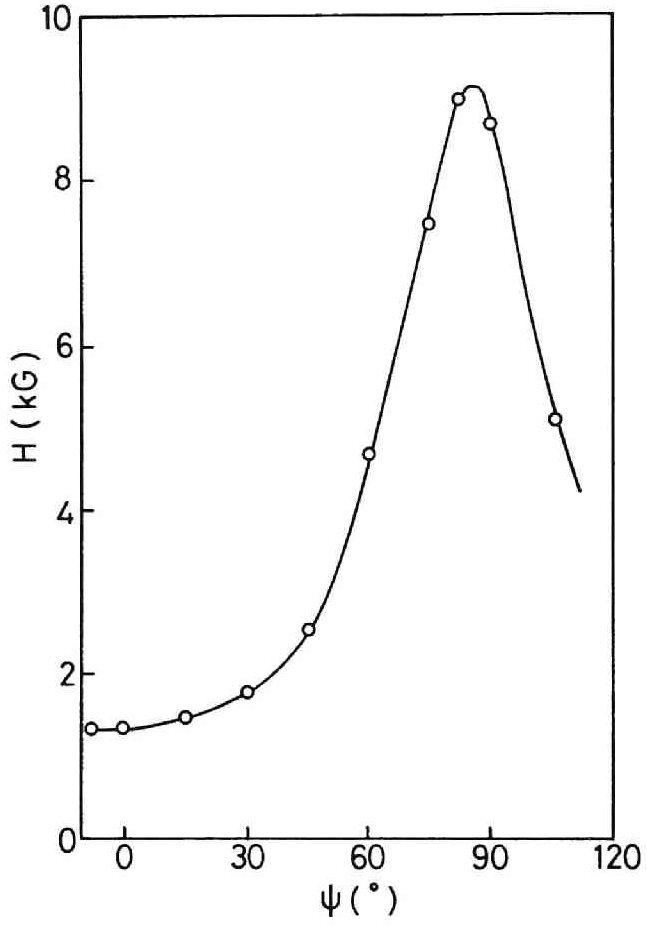

Fig.6.19 Variation of the resonance field with the angle between the applied field and the film plane of the Fe_3O_4 thin film, where $\psi = 0^\circ$ corresponds to $H_{||}$.

pendicular ($H_{\perp}$) and parallel ($H_{\parallel}$) to the film plane, respectively. The resonance field is lower when the external field is applied parallel to the film. The variation of the resonance field H with the angle ψ between the plane and the direction of the external field is shown in Fig.6.19, where $\psi=0^{\circ}$ corresponds to $H_{\parallel}$. The resonance field varies smoothly with the angle ψ and experiences a maximum and a minimum at about $\psi=90^{\circ}$ and $\psi=0^{\circ}$, respectively. This fact indicates that the axis of easy magnetization is in the plane. According to Kittel,[32] when only the

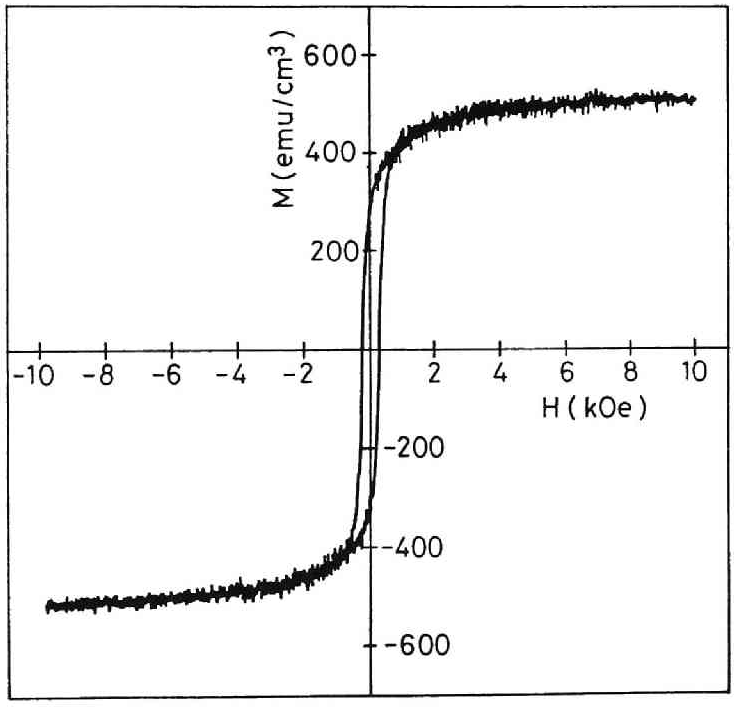

Fig.6.20 Magnetization curve of the Fe_3O_4 thin film measured parallel to the film surface at room temperature.

shape effect of the specimen is taken into consideration, the conditions of ferromagnetic resonance for an infinite plane are given for $H_{\perp}$ by

$$h\nu = g\beta(H_{\perp} - 4\pi M) \qquad (6.7)$$

and for $H_{||}$ by

$$h\nu = g\beta[H_{||} (H_{||} + 4\pi M)]^{1/2} \qquad (6.8)$$

in CGS units, where M is the magnetization and the other symbols have their usual meanings. For the present Fe_3O_4 thin film, $H_{\perp}$ and $H_{||}$ are 9100 and 1350 G, respectively, as seen from Fig. 6.19. Substituting these values into Eqs.(6.7) and (6.8), M 470 G and g 2.16 are obtained. The value of M is almost the same as that obtained by magnetization measurements as will be described below. These values are in good agreement with those reported for polycrystalline Fe_3O_4.[33] This fact means that the present Fe_3O_4 thin film is not heterogeneous but homogeneous; in other words, it does not consist of superparamagnetic fine particles which cause a descent of the magnetization.

The magnetization curve of the specimen heat-treated at 580 °C is shown in Fig.6.20. The magnetization tends to saturate at a relatively low external field and residual magnetization is observed, indicating that the film is characteristic of ferromagnetism and supporting the conclusion derived on the basis of ESR data. The coercive force is estimated to be 230 Oe from Fig.6.20. This value is larger than that of the bulk Fe_3O_4. This is ascribable to the smaller crystallite size of Fe_3O_4 in the present thin film compared with the bulk Fe_3O_4.

ESR spectra obtained for the γ-Fe_2O_3 thin film are shown in Fig.6.21. It is found that the external field applied parallel

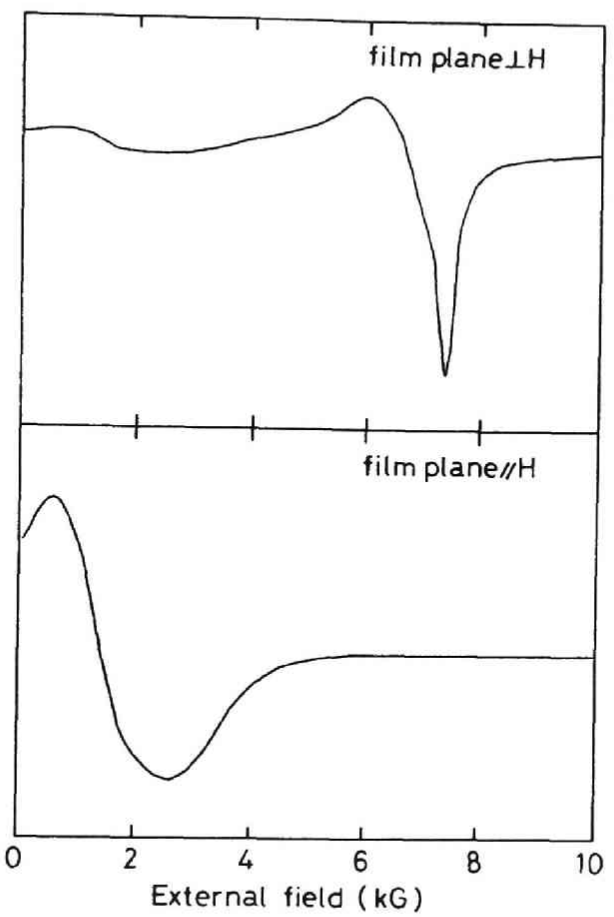

Fig.6.21 ESR spectra of γ-Fe_2O_3 thin film with the external field applied perpendicular and parallel to the surface of the thin film.

to the surface of the film yields the resonance line at lower magnetic field than that applied perpendicular to the surface, indicating that the axis of easy magnetization lies in the plane due to its shape effect. This situation is the same as the case of the Fe_3O_4 thin film mentioned above. Further, the shape of the resonance line is rather asymmetrical, indicating that Fe^{3+} ions are laid on anisotropic ligand fields.

6.3 Conclusions

The crystallization process of $70Fe_2O_3 \cdot 30P_2O_5$ and $60BaO \cdot 40Fe_2O_3$ glasses was followed by means of ESR and Mössbauer spectroscopy. As for the $70Fe_2O_3 \cdot 30P_2O_5$ glass, the isomer shift and the quadrupole splitting decrease monotonically for Fe^{3+} while they increase for Fe^{2+} as the crys-tallization proceeds, indicating that the bond length of Fe^{3+}-O is shorter and the configuration of O^{2-} around Fe^{3+} is more sym-metric in the crystalline state and in contrast the Fe^{2+}-O bond is longer and the symmetry of arrangement of O^{2-} around Fe^{2+} is less in the crystal precipi tated. At the first stage of the crystallization process, α-Fe_2O_3 particles precipitated were sufficiently small and so the specimen was superparamagnetic, as revealed from the line shape of the ESR and Mössbauer spectra of the heat-treated specimens. The superparamagnetic line narrowing was also observed in the ESR spectrum.

The $BaFe_2O_4$ crystal with Néel temperature of 880 K was precipitated from the $60BaO \cdot 40Fe_2O_3$ glass. It was found that the hyperfine field increases and the quadrupole splitting decreases with increasing the heat treatment temperature. Namely, the $BaFe_2O_4$ crystalline particle with smaller size exhibits smaller hyperfine field and larger quadrupole splitting. This fact is attributable to both superparamagnetism and effect of surface of the small particle. The ESR linewidth of the glass decreased with increasing the heat treatment temperature before the crys-tallization took place. It was thought that the change of Fe^{3+}-O-Fe^{3+} bond angle as well as the decrease of the Fe^{3+}-O bond

length which resulted from the thermal relaxation of the glass structure contributed to the decrease of the linewidth.

On the other hand, Fe_3O_4 and γ-Fe_2O_3 thin films coated on silica glass substrates were successfully obtained by the sol-gel method. The anisotropy in magnetic properties characteristic of the thin film form was clearly observed. The value of the magnetization of the present thin film is comparable to that of bulk Fe_3O_4, indicating that the present thin film can be a promising material for the practical use.

References

1) A.Ochi, K.Watanabe, M.Kiyama, T.Shinjo, Y.Bando and T.Takada, J. Phys. Soc. Jpn., **50**, 2777 (1981)

2) T.Shinjo, M.Kiyama, N.Sugita, K.Watanabe and T.Takada, J. Magn. Magn. Mat., **35**, 133 (1983)

3) A.H.Morrish and K.Haneda, J. Magn. Magn. Mat., **35**, 105 (1983)

4) S.F.Alvarado, Z. Phys., **B33**, 51 (1979)

5) T.Terashima and Y.Bando, J. Phys. Soc. Jpn., **54**, 3920 (1985)

6) I.Dzyaloshinsky, J. Phys. Chem. Solids, **4**, 241 (1958)

7) T.Moriya, Phys. Rev. Lett., **4**, 228 (1960)

8) P.W.Anderson and P.R.Weiss, Rev. Mod. Phys., **25**, 269 (1953)

9) L.Nëel, Rev. Mod. Phys., **25**, 293 (1953)

10) V.K.Sharma and F.Waldner, J. Appl. Phys., **48**, 4298 (1977)

11) S.M.Aharoni and M.H.Litt, J. Appl. Phys., **42**, 352 (1971)

12) C.Kittel, Phys. Rev., **76**, 743 (1946)

13) J.H.Van Vleck, Phys. Rev., **78**, 266 (1950)

14) M.Eibschütz, M.E.Lines and K.Nassau, Phys. Rev., **B21**, 3767 (1980)

15) C.R.Kurkjian and E.A.Sigety, Phys. Chem. Glasses, **9**, 73 (1968)

16) T.Komatsu and N.Soga, J. Appl. Phys., **51**, 601 (1980)

17) P.Kantor, A.Revcolevschi and R.Collonges, J. Mat. Sci., **8**, 1359 1973)

18) Y.Kuromitsu, K.Morinaga and T.Yanagase, Yogyo-Kyokai-Shi, **92**, 173 (1984)

19) Y.Goto and T.Takada, J. Am. Ceram. Soc., **43**, 150 (1960)

20) C.Do-Dinh, E.F.Bertaut and J.Chappert, J. de Phys., **30**, 566 (1969)

21) W.Kündig and H.Bömmel, Phys. Rev., **142**, 327 (1966)

22) J.H.Van Vleck, Phys. Rev., **74**, 1168 (1948)

23) K.Takahashi, T.Yoshio, K.Oda and F.Kanamaru, J. Non-Cryst. Solids, **42**, 157 (1980)

24) D.H.Harris, R.J.Janowiecki, C.E.Semler, M.C.Willson and J.T.Cheng, J. Appl. Phys., **41**, 1348 (1970)

25) H.Itoh, T.Takeda and S.Naka, J. Mat. Sci., **21**, 3677 (1986)

26) R.Wolfe, R.C.Lecraw, S.L.Blank and R.D.Pierce, Appl. Phys. Lett., **29**, 815 (1976)

27) M.Abe, Y.Tanno and Y.Tamaura, J. Appl. Phys., **57**, 3795 (1985)

28) G.Kordas, R.A.Weeks and N.Arfsten, J. Appl. Phys., **57**, 3812 (1985)

29) G.Kordas, Mat. Res. Soc. Symp. Proc., **73**, 685 (1986)

30) K.C.Chen, A.Janah and J.D.Mackenzie, Mat. Res. Soc. Symp. Proc. **73**, 731 (1986)

31) H.Dislich and E.Hussman, Thin Solid Films, **77**, 129 (1981)

32) C.Kittel, Introduction to Solid State Physics, 6th ed. (John Wiley & Sons, Inc., New York, 1986), Chap.16, p.481; Phys. Rev., **73**, 155 (1948)

33) J.Smit and H.P.J.Wijn, Ferrites, International edn (Tokyo Electrical Engineering College Press, Tokyo, 1965), Chap.8

SUMMARY

In the present thesis, local structure of iron, magnetic properties, and correlation between them for iron-containing amorphous magnetic matters, in particular, iron-containing oxide glasses which are interesting substances from both fundamental and practical viewpoints were examined in detail. Furthermore, from a standpoint of further clarification of the magnetism due to a random configuration of magnetic moments, magnetic properties of crystalline fine particles and thin films which have a larger fraction of magnetic moments in random state than bulk crystals were examined. The results obtained are summarized as follows.

In Chapter 1, the general background and purpose of the present study were outlined. Several interesting features in the magnetism of not only oxide glasses but amorphous alloys were described and the unresolved problems concerning the local structure and the magnetic properties of oxide glasses were suggested.

In Chapter 2, the cluster spin glass transition observed for most of the amorphous oxides and fluorides was treated theoretically. An attempt was made to explain the cluster spin glass transition on the basis of the superparamagnetic model by considering temperature dependence of cluster size, intercluster interactions and a distribution of superexchange interaction. The theoretical calculation was performed for some distribution functions. As a result, it was found that the spin-freezing temperature increases monotonically with increasing the average value of the superexchange interaction. Since the magnitude of the superexchange interaction is proportional to the small co-

valency of Fe^{3+}-O or Fe^{3+}-F bond, the above fact led to the inference that the spin-freezing temperature increases with an increase of the covalency of Fe^{3+}-O or Fe^{3+}-F bond.

In this chapter, the principle of ESR and Mössbauer spectroscopies was also described. In particular, for the purpose of utilizing the Mössbauer spectroscopy to examine the bonding characteristics of iron in amorphous solids from a viewpoint of the lattice vibration, the temperature dependence of recoil-free fraction and second-order Doppler shift was theoretically derived for the two-band model which describes the lattice dynamical properties of amorphous solids much better than the Debye model. The equations derived were used to analyze the experimental data of amorphous Fe-B and Fe-P alloys. It was found that agreement of the theoretical curve and the experimental data was fairly good for the temperature dependence of both recoil-free fraction and second-order Doppler shift.

In Chapter 3, the cluster spin glass theory derived in Chapter 2 was applied to the present oxide and fluoride glasses. First of all, the relation between the spin-freezing temperature and the covalency of Fe-O and Fe-F bonds, which was estimated from the isomer shift, was examined for several oxide and fluoride glasses. As a result, it was found that the spin-freezing temperature tends to decrease with increasing the isomer shift, which was coincident with the prediction of the theory. Second, the present theory was applied to the explanation of the measuring frequency dependence of the spin-freezing temperature for oxide glasses which was empirically represented by the Vogel-

Fulcher law. It was found that the theory well described the measuring frequency dependence of the spin-freezing temperature for some oxide glasses. Third, the qualitative description of the temperature dependence of the susceptibility in the superparamagnetic region was derived, which was found to be qualitatively coincident with the experimental data of some oxide and fluoride glasses. Finally, the relation between the spin-freezing temperature and the covalency was well applied to the interpretation of the room temperature Mössbauer spectra of amorphous $CaO-Bi_2O_3-Fe_2O_3$ system which shows ferromagnetic character. In other words, the magnetism of this amorphous system could be explained in terms of the superparamagnetic or mictomagnetic model.

In Chapter 4, the covalency of $Fe^{3+}(Fe^{2+})$-O bond in several oxide glasses was estimated from the isomer shift value appearing in Mössbauer spectrum. The degree of covalency was dependant on the glass systems and compositions, and that dependency was explainable in terms of the principle of electronegativity equalization. Namely, the larger degree of covalency in $Fe^{3+}(Fe^{2+})$-O bond results from the smaller value of average electronegativity of glass constituent atoms. This is the first case that the concept of principle of electronegativity equalization proposed by Sanderson is applied to the inorganic glasses. The experimental data for the present oxide glasses along with the fluoride glasses studied thus far agreed with this conception as a whole. However, a slight deviation from the correlation between the covalency and the average electronegativity was observed for $Bi_2O_3-Fe_2O_3$ glasses. More detailed investigation on the local

environment of iron in these glasses revealed that the symmetry of the oxygen coordination state around iron is more dominant than the electronegativity for determination of the covalency of Fe^{3+}-O bond because the electronegativity of Fe and Bi is almost the same.

In Chapter 5, the state of Fe^{3+} ion cluster in oxide glasses prepared by the conventional melting-and-quenching method and the sol-gel method was discussed. For the borate glasses prepared from the melts, the number of Fe^{3+} ion cluster increased with decreasing the melting temperature. This fact was explained by assuming that a chemical equilibrium exists between isolated Fe^{3+} ions and clustered Fe^{3+} ions in the molten glass and the change of enthalpy controls the clustering reaction. It was also revealed that the number of the Fe^{3+} ion cluster varies with the glass composition for lithium borate glasses derived from the melts. The change of the number of Fe^{3+} ion cluster with Li_2O content corresponded well to the compositional dependence of the oxygen coordination number to boron and the number of nonbridging oxygen ion. It was thought from this fact that the state of Fe^{3+} ion cluster is determined by the entropy change for the reaction between isolated and clustered Fe^{3+} ions in the low Li_2O content range and by the enthalpy change in the high Li_2O content range. On the other hand, the state of Fe^{3+} ion cluster in oxide glasses prepared by the sol-gel method depended on that in the gel precursors and it was varied with heat treatment temperature. Namely, the heat treatment at higher temperatures promoted the clustering of Fe^{3+} ions.

In Chapter 6, magnetic properties of fine particles and thin films prepared by the crystallization of oxide glass and gel were described. For α-Fe_2O_3 crystal which was precipitated from the iron phosphate glass, superparamagnetic behavior was clearly observed when the particle size of α-Fe_2O_3 was sufficiently small as demonstrated by the change of ESR linewidth and Mössbauer spectra with the growth of the crystal. Besides, the smaller particle of $BaFe_2O_4$ crystal precipitated from the barium iron oxide glass exhibited larger value of quadrupole splitting and smaller hyperfine field than the larger particle. This fact was explained by the surface effect of the small particle. On the other hand, the shape effect was observed for Fe_3O_4 and γ-Fe_2O_3 thin films prepared by the sol-gel method. Namely, the axis of easy magnetization was present in plane in these thin films. Moreover, the magnetization of the present Fe_3O_4 thin film bore comparison with that of bulk Fe_3O_4, suggesting that the present thin film can be a candidate for practical applications.

ACKNOWLEDGEMENTS

The present thesis has been carried out under the direction of Professor Naohiro Soga at Faculty of Engineering in Kyoto University.

The author wishes to express his sincere gratitude to Professor Naohiro Soga for his continuous encouragement and valuable advice all through the duration of the present work. The author is also indebted to Professor Kanichi Kamiya of Faculty of Engineering, Mie University, for his informative discussion and helpful advice. Continuous encouragement given by Professor Rikuo Ota and Dr. Toshinobu Yoko is also appreciated. The author wishes to express his appreciations to Drs. Teiichi Hanada and Kazuyuki Hirao for their useful discussions. The author would like to thank Dr. Yasuhito Isozumi of Radioisotope Research Center, Kyoto University, for the Mössbauer effect measurements and for suggestions on many aspects of this work. The author also would like to thank Professor Koichi Sugiyama of Electrical Engineering Department, Mie University, for the ESR measurements and valuable discussions.

Finally, the author thanks Mrs. Hiroko Tanaka, his wife, for her support and encouragement.

Katsuhisa Tanaka